



**POLITECNICO**  
MILANO 1863

SCUOLA DI INGEGNERIA INDUSTRIALE  
E DELL'INFORMAZIONE

# A preliminary experimental and numerical analysis of hybrid CFRP/aluminum tubes under dynamic axial loading

TESI DI LAUREA MAGISTRALE IN  
AERONAUTICAL ENGINEERING  
INGEGNERIA AERONAUTICA

Author: **Stefano Terragni**

Student ID: 900563

Advisor: Paolo Astori

Co-advisor: Giulia Vignati, Ivan Colamartino, Navid Ghavanini

Academic Year: 2021-22



## Abstract

The following study addresses the problem of analysing the behaviour of a hybrid composite-metal component, especially in the axial crush absorbing energy field.

An aluminium circular tube coupled with Carbon Resin Fibre Plastic (CFRP) lamination was investigated.

The study is divided in two, an experimental campaign of different tube configurations using a drop tower testing system and numerical simulations in order to capture and correlate the dynamic of the crushing process.

Each configuration has been reproduced and simulated in the finite element code LS-Dyna.

**Key-words:** FML, CFRP, Crushing tube, Simulation.



## Abstract in italiano

Il seguente lavoro tratta l'analisi del comportamento a crash di tubi ibridi metallo-composito, nello specifico il comportamento di assorbimento di energia durante un impatto assiale.

È stato ispezionato il comportamento di un tubo in alluminio rinforzato tramite laminazione di pre-impregnati in fibra di carbonio.

Lo studio si è diviso in test sperimentali utilizzando il sistema "torre di caduta", in differenti configurazioni di laminazione, e la correlazione del comportamento tramite simulazioni numeriche.

Tutte le configurazioni sono state simulate tramite il codice ad elementi finiti LS-Dyna.

**Parole chiave:** Compositi, Impatto assiale tubi, Simulazioni.



# Contents

<b>Abstract</b> .....	<b>i</b>
<b>Abstract in italiano</b> .....	<b>iii</b>
<b>Contents</b> .....	<b>v</b>
<b>Introduction</b> .....	<b>1</b>
<b>1 Background theory</b> .....	<b>5</b>
1.1. Crashworthiness .....	5
1.1.1. Energy Absorber.....	5
1.1.2. Loading modes .....	8
1.2. Ductile material crushing tubes.....	10
1.2.1. Ductile circular tubes .....	11
1.2.2. Ductile global bending deformation .....	14
1.3. Composite material crushing tubes .....	16
1.3.1. Composite material.....	18
1.3.2. Macroscopic failure mechanisms of axial loading.....	19
1.3.3. Microscopic failure mechanisms of axial loading .....	23
1.3.4. Trigger Mechanism .....	29
1.3.5. Fiber Orientation .....	30
1.3.6. Strain Rate Sensitivity .....	32
1.4. Hybrid material crushing tubes.....	32
1.4.1. Advantages and Applications of FML .....	33
1.4.2. FMLs under axial crushing load .....	35
<b>2 Manufacturing</b> .....	<b>40</b>
2.1. Materials and Components .....	40
2.2. Lay-up procedure .....	42
2.2.1. Tube manufacturing .....	42

2.2.2.	Intermediate compaction .....	44
2.2.3.	Tensile specimen lay-up .....	45
2.3.	Autoclave curing process .....	46
2.3.1.	Vacuum-assisted bag molding .....	46
2.3.2.	Curing cycle .....	48
2.4.	Test specimens .....	49
2.4.1.	Energy absorption tube specimens.....	49
2.4.2.	Tensile test specimens.....	51
<b>3</b>	<b>Experimental Testing.....</b>	<b>53</b>
3.1.	Material characterization.....	53
3.1.1.	Tensile Testing .....	54
3.1.2.	In-plane shear .....	58
3.2.	Drop tower testing.....	61
3.2.1.	Aluminum tube .....	63
3.2.2.	Composite tubes .....	64
3.2.3.	External lamination hybrid tubes .....	69
3.2.4.	Internal lamination hybrid tubes .....	72
3.3.	Comparative analysis.....	75
<b>4</b>	<b>Numerical simulation.....</b>	<b>80</b>
4.1.	Numerical model.....	80
4.1.1.	Laminated composite fabric material model.....	81
4.1.2.	Piecewise linear plasticity material model .....	85
4.1.3.	Aluminum-composite delamination model.....	87
4.2.	Model build-up .....	89
4.3.	Results .....	91
4.3.1.	Aluminum tube numerical model results .....	91
4.3.2.	Numerical model: composite tube.....	93
4.3.3.	External lamination hybrid tube numerical model results .....	96
4.3.4.	Internal lamination hybrid tube numerical model results .....	99



<b>5</b>	<b>Conclusions and future developments .....</b>	<b>103</b>
5.1.	Conclusions .....	103
5.2.	Future development .....	104
	<b>Bibliography.....</b>	<b>109</b>
<b>A</b>	<b>Appendix A .....</b>	<b>119</b>
A.1.	Manufacturing.....	119
A.2.	Tensile test .....	120
B.1.	Crush test pictures.....	121
	<b>List of Figures .....</b>	<b>123</b>
	<b>List of Tables .....</b>	<b>127</b>
	<b>List of symbols .....</b>	<b>129</b>
	<b>Acknowledgments.....</b>	<b>131</b>



## Introduction

The work presented in this thesis began as the starting point for a wide field of research named hybrid components. FML (Fiber Metal Laminates), which are materials known for their performance in the aeronautical field, is the basic idea and starting point for the research of background theory.

With the aim of exploiting the useful material characteristics of both ductile and composite materials, the study lays in the big picture of the structure crashworthiness macro topic. It is wanted to design a structure that protect occupants of vehicle during an impact, this is obtained dissipating the phenomena kinetic energy via deformation and breakage of the structure itself.

In the passive safety field, axial crushing tubes are one of the most used components, therefore the geometry of a thin wall tube is known from the beginning. In this study it is analyzed the state of the art on tubes behavior during impact, regarding bare composite and ductile materials. The materials have different responses, and their interaction can be beneficial in the dissipation of energy. The post-crush result of composite and ductile circular tubes are presented in Figure 0.1.



Figure 0.1: Circular tubes after impact (a) composite, (b) ductile.

Hybrid thin-walled tubes, composed of composite and metal, can use the stable plastic deformation of metal to guide and control the progressive failure of the composite to improve their energy absorption characteristics. Therefore, hybrid thin-walled tubes have attracted the attention of researchers.

After a deep analysis of articles and books about the subjects, circular aluminum (AL) tube with a simple layup of Carbon Fiber Reinforced Plastic (CFRP) are considered for the study. Moreover, regarding hybrid tubes are considered two configurations:

- External lamination, the composite lay-up is applied on the external surface of the aluminum tube.
- Internal lamination, the composite lay-up is applied on the internal surface of the aluminum tube.

All the specimens are built with the vacuum-assisted bag molding and the process is described step by step to highlight the features to assemble FML tubes.

The aim of the study is to analyze the energy absorption behavior of tube structure considering how the composite and ductile material interact with each other and compare the hybrid configurations with the bare CFRP and AL tubes.

The capability of a structure to absorb energy during a crash is defined by the examination of the reaction force exerted by the component to an impacting mass. This analysis is obtained by the use of drop tower test. The crushing phenomena is inspected by employing sensors and high frame rate videos, to capture the ways structures behave. The drop tower test system employed in this study is presented in Figure 0.2.



Figure 0.2: Drop tower test.

Deformations and ruptures are expected during the impact, which characterizes the reaction acceleration magnitude experienced by the impacting mass.

In addition, a numerical model is defined by the use of Finite Element Method (FEM) and simulation performed by the solver Ansys LS-DYNA®, which is an explicit simulation software used for applications like drop tests, impact and penetration, smashes and crashes, occupant safety, and more.

The study is entirely performed at the Department of Aerospace Science and Technology of Politecnico di Milano, from the manufactory of all the specimens and components at the Technological Laboratory, the material characterization at the Experimental Test Laboratory and the crushing test at the Transport Safety Laboratory (LaST).



# 1 Background theory

The study deals with three major aspects: ductile-composite material, experimental testing and simulation. In this chapter, the base theory is summed up as an introduction to the analysis of the results obtained in the next chapters.

## 1.1. Crashworthiness

Early in the 1960s, the U.S. Army Aviation Research and Technology Activity started a campaign to study all the aspects of aircraft safety and survivability, related to specific relationships among crash forces and structural failures. In those years, the idea of a structural design with the objective of crash resistance in order to eliminate unnecessary human injuries and fatalities developed, hence the idea of 'structural crashworthiness' was born.

The term 'structural crashworthiness' is used to describe the impact performance of a structure when it collides with another object. A study into the structural crashworthiness characteristics of a system is required in order to calculate the forces during a collision which are needed to assess the damage to structures and the survivability of passengers in vehicles, for example. This topic embraces the collision protection of aircraft, buses, cars, trains, ships and offshore platforms, spacecraft, etc. [1].

Depending on the nature of the impact and the vehicle involved, different criteria are used to determine the crashworthiness of the structure. But, generally speaking, the core is to reduce the load transferred from the structure to the occupants during impact. The basic thought is to transform and dissipate the kinetic energy of the system using components of the structure.

In the everyday transportation vehicles, structures are designed embedded with energy-absorbing system.

### 1.1.1. Energy Absorber

The kinetic energy of a moving mass can be absorbed by applying a force over a distance; this is the primary mechanism for absorbing crash energy [2]. The

energy-absorbing mechanism transmits the crash force to the occupant of the vehicle; therefore, the loads should be tolerable to passengers.

By considering the same energy, the stroke of an energy-absorbing system is inversely proportional to the average load on the mass, i.e. higher stroke, lower loads. But, by considering the vehicle system, the stroke distance must be consistent with the structural design.

The energy absorption system behavior during the crushing dynamic is defined by some parameters that exploit the efficiency and mechanical characteristic of the component:

- Crushing length ( $\delta$ ), is the distance travelled by the impacting mass during the crushing phenomena. It is often addressed as stroke length.
- Initial Peak Crushing Force (IPCF), defined as the first peak (maximum crushing) force. The peak crushing load (Pmax) is related to the possibility of damage to connected members and the injury of passengers. IPCF is the maximum force usually observed at the onset of the progressive damage and generally highly dependent on the type of trigger [3].
- Mean Crushing Force (MCF), is calculated as the average force of the total crush process. Considering  $F_i$  as the axial load during the impact, and  $n$  is the total number of points considered.

$$MCF = \frac{\sum_{i=1}^n F_i}{n} \quad (1.1)$$

- Crushing Force Efficiency (CFE), evaluates the crashworthiness in a more comprehensive way.

$$CFE = \frac{MCF}{IPCF} \quad (1.2)$$

CFE reveals the uniformity of load–displacement curve of the tube (it is related to the energy absorption efficiency) and higher values of it indicate that the tube behavior is closer to the ideal energy absorber and the fluctuations of load–displacement curve are less and guarantees less injury of the occupants [4].

- Energy Absorption (EA), the total energy dissipation of the test specimen determined from the area under the force–displacement curve.



$$EA = \int_0^{\delta} F(x)dx \quad (1.3)$$

Where  $F(x)$  is the instantaneous crushing force and  $x$  is the displacement of the striker during the crushing phenomenon.

- Specific Energy Absorption (SEA) is the energy absorbed per unit mass of crushed material, also defined as damaged material.

$$SEA = \frac{EA(\delta)}{Weight_{damage\ material}} \quad (1.4)$$

The damage material is defined as:

$$Weight_{damage\ material} = \mu\delta \quad (1.5)$$

Where  $\mu$  is the mass per unit length of the structure.

A high SEA value means that the crash energy component exploits its structure and mass in an efficient way, therefore the design of the absorber can result in a lighter component.

- Stroke efficiency ( $\eta_s$ ), is defined as the maximum useful displacement divided by the original length ( $L$ ) of the energy absorber [5]. Especially for ductile components, axial crushing eventually results in the compaction or densification of the structure, rapidly increasing the force levels. When this occurs, higher efficiency is achieved, meaning that the entire structure participates in the phenomena. This indicator is only calculated for the dynamic results, since the crushing length of the quasi-static crushing tests is far from the compaction region of the curve [6].

$$\eta_s = \delta/L \quad (1.6)$$

The aforementioned parameters are sketched In Figure 1.1 [7].

In the field of energy absorption, the structures analyzed over the years differ from the basic tubes to more complicated structures (rings, honeycomb, straps bending etc.). The different material and production process used for the application must be considered, as geometry can vary.

Tubes are simple geometry and simple to manufacture. They have drawn much attention owing to the stable crushing load and long stroke.

Still, the axially loaded tube energy absorbers have a huge variation in terms of geometric shape where they may be: circular, square, triangle, or polygon in cross

section. Furthermore, they may be formed in a single or multi-cell configuration. Additionally, they may adopt a form that is straight or tapered in appearance.

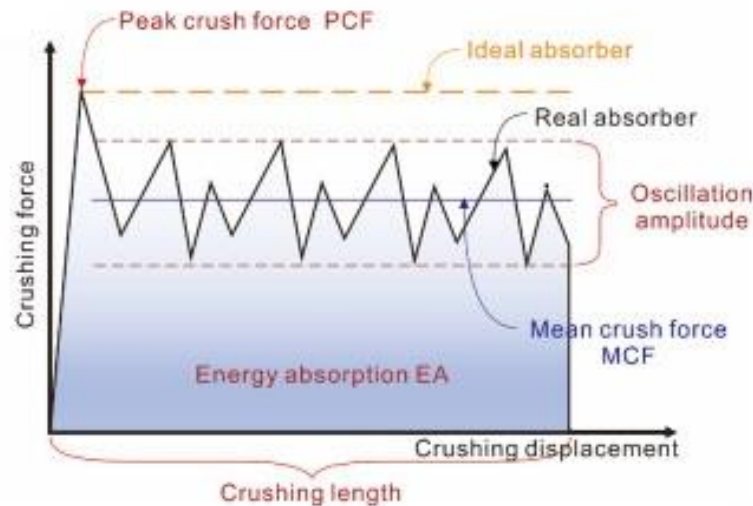


Figure 1.1: Representative crushing force–displacement curve

Obviously, as much as the geometry, the chosen material will crucially influence in the deformation behavior and the loading response during the impact. In literature, the most common material used to manufacture thin-walled tubes with the aim of energy absorbing, are ductile and composite materials.

### 1.1.2. Loading modes

The geometrical shape of a thin-walled tube, the way through which it is loaded and its deformation, are crucial factors in the crashworthiness performance. These factors determine the amount of the tube materials that participate in the energy absorbing process.

The dynamic loading of an impact crushing scenario can always be idealized as an impacting mass moving relatively fast towards the component with a defined direction. Mass and velocity define the energy (kinetic) involved in the crushing; the direction identifies the type of load situation.

Basically, the most common loading situations of the thin-walled tubes used in the protection system of a vehicle are axial, oblique, lateral and bending loading, as shown in Figure 1.2.

As an example, during a full-frontal automobile collision scenario, the front longitudinal rails including the crash boxes undergo axial loading and during the impact deform and absorb around 50% of the total kinetic energy. On the other

hand, the bumper cross beam undergoes a bending or lateral deformation mode and absorbs around 25% of the total energy [8].

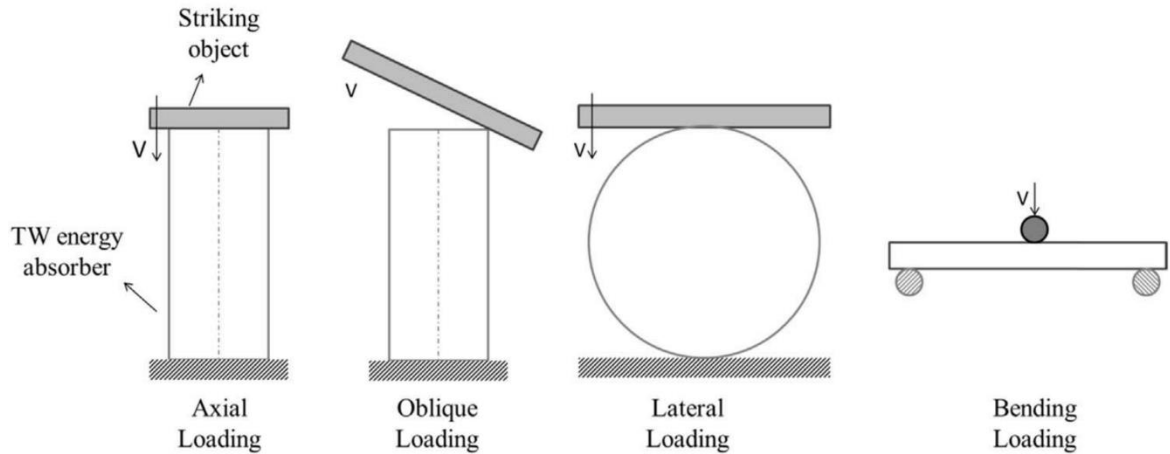


Figure 1.2: Typical load configuration

The remaining kinetic energy is absorbed by the other front structural components of the car (front panel, fenders, wheel wells, and hood), see Figure 1.3.

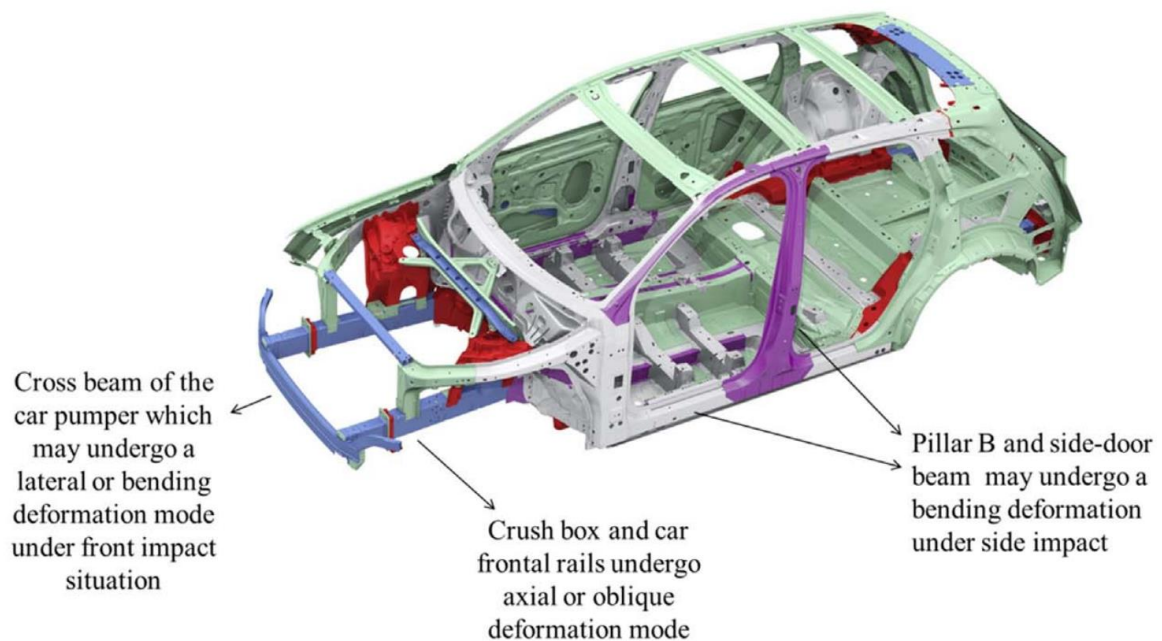


Figure 1.3: Most common energy absorption sub-structures in automobiles [9].

Axially loaded thin-walled components are the most commonly used structures as energy absorbers and appear mainly in the automotive industry (e.g. crush box behind the car bumper) and aeronautical industry (e.g. aeronautical seats). The axial crushing of tubes is characterized by a reasonably constant collapse load and a comparatively high energy absorbing capacity where the specific energy

absorbing capacity of axially loaded components is approximately 10 times greater than that in laterally compressed tubes [10].

## 1.2. Ductile material crushing tubes

The crash components of an aeronautical civil vehicle are mostly manufactured using a metallic material such as aluminum alloy and mild steel.

Aluminum structures are considered very effective for developing the lightweight vehicle. The mechanical properties of the absorber's material, such as yield stress and strain hardening behavior, play an important role in the crashworthiness behavior. This is due to the fact that under axial loading, the majority of the tube's material deforms plastically to participate in the energy dissipating process.

It is fundamental that deformation in ductile absorber is plastic and not elastic. Elastic deformation is not a dissipating energy deformation, and the kinetic energy of the impact could be transformed again in kinetic energy.

Metallic materials are normally sensitive to loading rate where their mechanical properties under dynamic loading are different from those observed under quasi-static loading. It should be noted that the material's strain rate sensitivity is a material property and is independent from the geometrical factors of the thin walled tube [11]. The dynamic behavior of metallic materials has been substantially investigated, consequently, an almost complete understanding has been established.





Material strain rate sensitivity is a beneficial phenomenon since it allows the material to achieve a greater energy absorption capacity when it is loaded dynamically [9].

The energy-absorbing behavior of various cross-sections and configurations of axially loaded components were compared in many papers and a summary of these is presented in Table 1.1.

For the sake of considering a simple cross-section geometry, a circular tube is chosen in this study, mainly because the square tubes are less effective at absorption energy than circular tubes.

Tang et al. [12] reported that the structural effectiveness of a square tube is about 0.7 of a circular tube. This could mainly be caused by the severe deformation concentrated in the zones near to the corner of square tubes.

Table 1.1: Summary of crashworthiness comparative papers [9]

<i>Ref</i>	<i>Material and load Condition</i>	<i>Cross section SEA from best to worst</i>
[13]	<ul style="list-style-type: none"> <li>Aluminium alloy</li> <li>Quasi-static loading</li> </ul>	
[14]	<ul style="list-style-type: none"> <li>Mild steel</li> <li>Dynamic loading</li> </ul>	
[15]	<ul style="list-style-type: none"> <li>Aluminum</li> <li>Quasi-static loading</li> </ul>	
[16]	<ul style="list-style-type: none"> <li>Aluminum</li> <li>Quasi-static loading</li> </ul>	

### 1.2.1. Ductile circular tubes

The axial crushing of circular tubes is extensively studied by many researchers for its energy absorption capability. Studies on the axial collapse of a circular tube were made to develop analytical models that estimate the mean crush force [17][18][19].

In literature, it is reported that axial crushing of a circular tube involves progressive folding or buckling of the tube with one or more of three main deformation modes:

- axisymmetric or concertina, Figure 1.4(a),
- non-symmetric or diamond, Figure 1.4(b),
- mixed mode, Figure 1.4 (c).

It is evident from Figure 1.5(a) that the load–displacement behavior impact scenario exhibits a repeated pattern. Each pair of peaks in Figure 1.5(a) is associated with the development of a wrinkle or buckle in Figure 1.5(b). Usually, the folding shown in Figure 1.4 develop sequentially from one end of a tube so that the phenomenon is known as progressive buckling. For convenience, designers often ignore the fluctuations in the load-displacement characteristics and use MCF ( $P_m$  in Figure 1.5(a)).

An ideal energy-absorbing device is defined, for some purposes, as one which has a constant resistance and, therefore, offers a constant deceleration throughout the entire stroke.

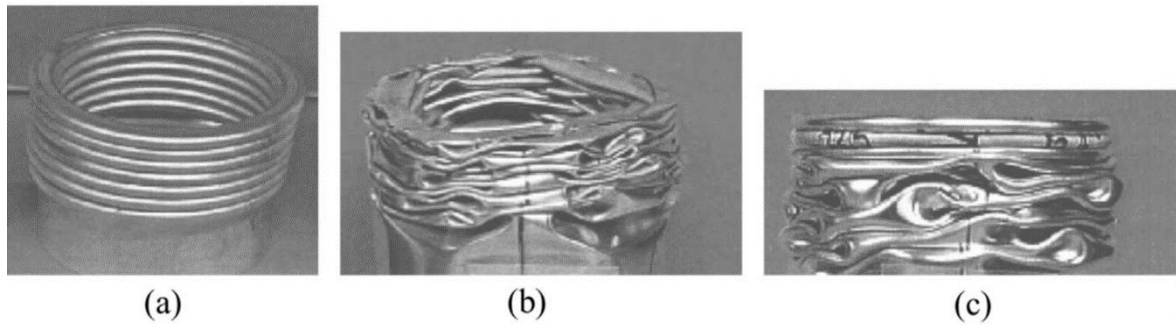
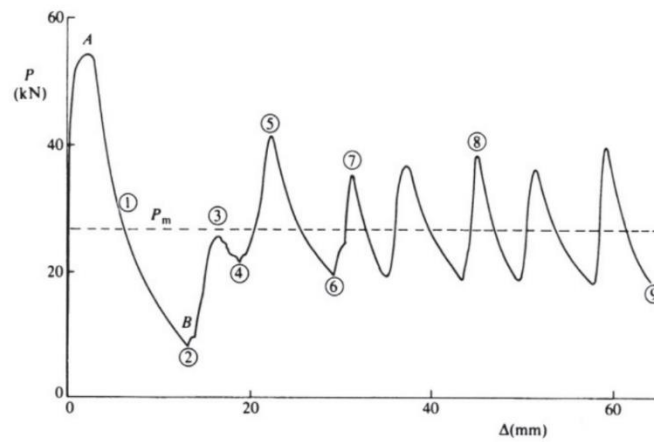
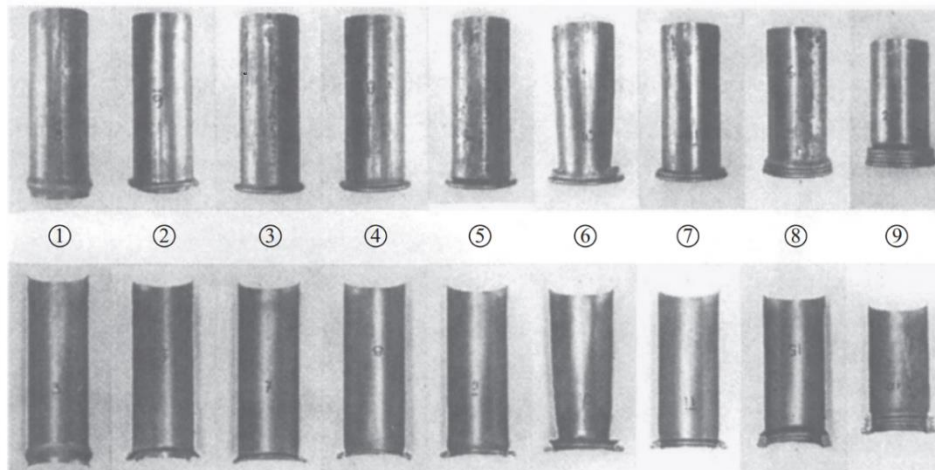


Figure 1.4: Axially loaded deformation modes of circular tube [20]



(a)



(b)

Figure 1.5: (a) Axial force vs axial crushing distance, (b) photographic record of the development of wrinkles during axial crushing [11].

The photographs (from left to right) in Figure 1.5(b) refer to numbers 1 to 9 in Figure 1.5(a). The upper row gives the outside views, while the lower row shows the specimens cut open across a diameter.

The characteristic dimensions of a circular tube geometry have a significant influence on its deformation mode during the impact, especially if the ratio of diameter to thickness ( $D/t$ ) and the ratio of length to thickness ( $L/t$ ) are considered. Different deformation modes are obtained varying these values [20].

It is reported that these crushing modes generally develop in these ranges [21]:

- Diamond mode:  $\frac{D}{t} > 80$
- Concertina mode:  $\frac{D}{t} < 50$  and  $\frac{L}{t} < 2$
- Mixed modes:  $\frac{D}{t} < 50$  and  $\frac{L}{t} > 2$

Many researchers have developed theoretical models for each deformation mechanism of the axial crushing of the circular tubes, with the aim of computing the MCF. Some researchers [20], who investigated the axial compression of circular aluminum tubes under quasi-static conditions, developed an empirical expression for MCF that works for any deformation mode. They confirmed, as other authors, that the mean force relates to  $D/t$  ratio as shown in Equation (1.7).

$$MCF = 18.075 \sigma_0 t^2 \left( \frac{D}{t} \right)^{0.32} \quad (1.7)$$

$$\sigma_0 = \sqrt{\frac{\sigma_y \sigma_u}{1 + n_{sh}}} \quad (1.8)$$

Where in Equation (1.7) and (1.8),  $\sigma_0$  is the flow stress,  $\sigma_y$  is the yield stress,  $\sigma_u$  is the ultimate stress and  $n_{sh}$  is the strain hardening exponent from the power law stress strain curve.

In addition to geometrical parameters, loading velocity has a great influence on the deformation pattern of a circular tube. It is found that high impact speeds produced a unique plastic deformation called 'Mushrooming' which made the walls of the shell thicker [22]. Studies identified three modes of deformation, as shown in Figure 1.6, depending on the velocity of impact and the thickness:

1. progressive deformation mode in the form of folds for tubes with small wall thickness at relatively low velocity,
2. mushrooming associated with folds for all tubes at medium velocity,
3. mushrooming associated with wrinkling for tubes with big wall thicknesses at high velocity.

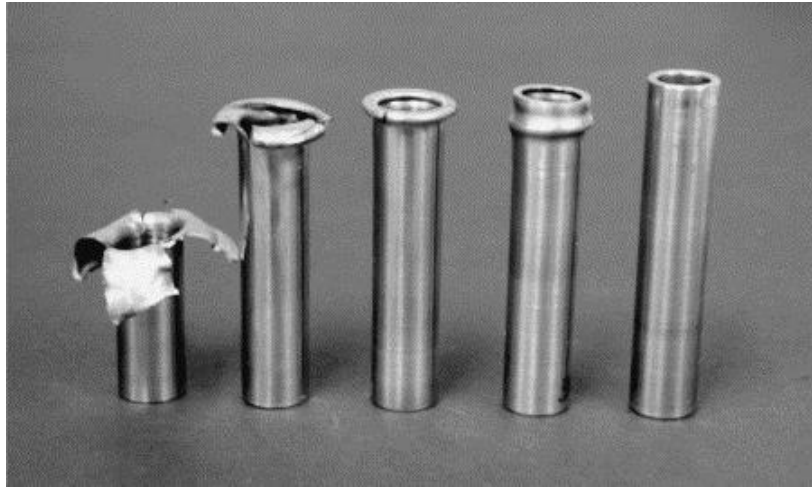


Figure 1.6: Mild steel samples, velocities from left to right are: 352, 158, 127, 114 m/s and untested [22].

### 1.2.2. Ductile global bending deformation

In general, based on their dimensions, the thin-walled tubes can undergo a global buckling or global bending deformation mode during their axial crushing. The phenomenon is related to the global Euler buckling of a bar under compression. This mode is very dangerous, unstable and inefficient (leading to a considerable decrease in the effectiveness of an energy absorber). It should be avoided when designing an energy absorption structure.

The global bending deformation mode may occur despite of the cross-section type of the tube, for example as shown in Figure 1.7 the collapse of a circular [20] and square tubes [23].

The occurrence of global bending in axially loaded circular tubes depends on the diameter to thickness ( $D/t$ ) and length to diameter ( $L/D$ ) ratios, as reported by Guillow et al. [20]. In Figure 1.8 it is shown a typical curve of an axial load response of an aluminum tube for progressing folding mode and catastrophic buckling collapse.

As equivalent as global Euler buckling mode theory, experimental studies (performed by Abramowicz [24]) prove that there is a critical tube length ( $L_{cr}$ ) where the tubes with lengths less than the critical value deform progressively while tubes longer than the critical length undergo a global bending mode.



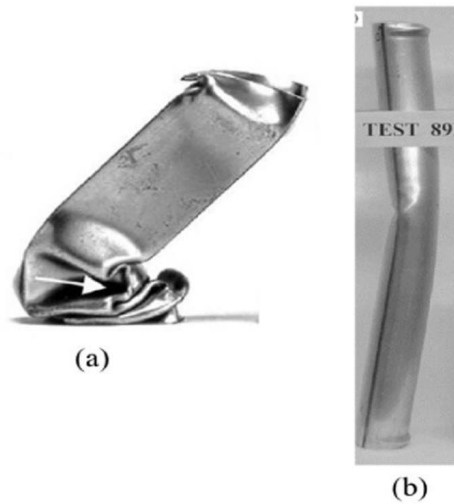


Figure 1.7: Buckling collapse of (a) square [23] and (b) circular tubes [20].

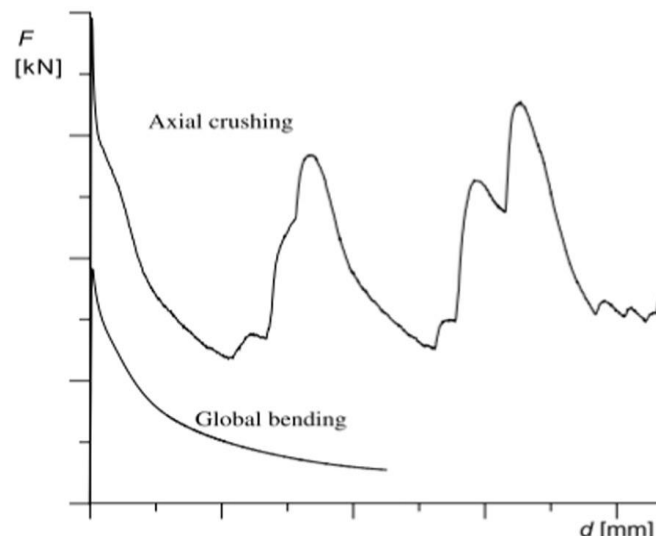


Figure 1.8: Global buckling versus progressive folding [20].

It is found that, when the tube length is close to critical value, a mixed mode of progressive deformation and global bending deformation mode could occur. As a consequence, the global bending mode develops at the later stages of the deformation. Generally, the critical length, is believed to be influenced by the following factors: material properties (yield stress, strain and hardening behavior), impact velocity, and tube dimensions [24].

Abramowicz and Jones [24] reported that circular tubes with greater  $D/t$  have longer  $L_{cr}$ . Karagiozova and Alves [25] found that  $L_{cr}$  increases as the impact velocity increases.

### 1.3. Composite material crushing tubes

Many of the mechanical devices and elements, made of metals, polymers and composite materials, are designed to absorb impact energy under axial crushing, bending and/or combined loading. An important requirement is that these structural members must be able to dissipate large amounts of energy by controlled collapse in the event of a collision. Composite materials have gained much attention over the last three decades in crashworthiness applications due to their high specific strength, high specific stiffness and excellent energy absorption performance [26].

Besides the perspective of reduced weight and design, composite materials offer a considerable potential for lightweight energy absorbing structures; these facts attract the attention of the automotive and aircraft industry owing to the increased use of composite materials in various applications, such as frame rails used in the apron construction of a car body and the subfloor of an aircraft, replacing the conventional materials used [27].

The energy-absorption behavior of composite materials and structural components is affected by number of factors. The characteristics of a fiber reinforced composite lamina are governed by:

- fiber material,
- matrix material,
- fiber-matrix interface,
- fiber content.

The total mechanical behavior of a composite laminate is defined by important factors, the response of the material could change completely with the variation of these parameters:

- laminate stacking sequence,
- lamina orientation in each layer
- type of lamina: unidirectional, woven fabric or braided fabric.

Woven composites introduce a different approach to the fabrication of thick sections for use in primary and secondary structural applications. Interlacing two mutually perpendicular sets of yarn shapes woven composites. The lengthwise clothes are called warp and the crosswise clothes are known as fill or weft (see Figure 1.9). Warp and weft's interlacing pattern are known as weave. The fundamental two-dimensional weaves are plain, twill and satin, where it provides more balanced properties in the fabric plane than a unidirectional laminate [28][29][30].

The weave architecture gives improvements of in-plane stiffness and strength. The classical laminate theory cannot be used to predict the mechanical properties of woven composite due to many specific factors including the density of the fiber bundles, the type of the weaving and the curvature that are essential to be considered [31].

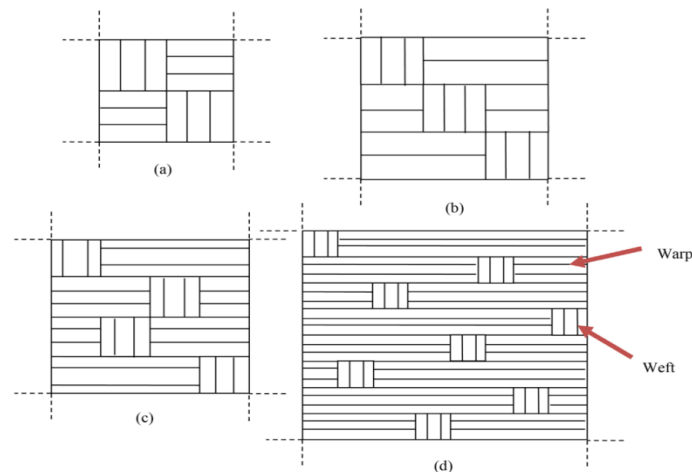


Figure 1.9: 2D-Weave composites: (a) plain, (b) twill, (c) 4-harness, (d) 8-harness [32]

Testing conditions specify the loading direction with respect to the components (axial or transverse) and loading rate (static or dynamic). For composites, most properties are highly temperature-dependent and thus temperature is also an important factor.

The composite structures absorb greater SEA than the metallic structures such as mild steel and aluminum [33]. However, the design and analysis of composite energy absorbers are difficult due to anisotropic properties of composite material, but, varying the type of fiber, matrix and fiber orientation, the designer has the ability to produce composites components with material properties improved for the specific application [33].

The composite structures have a negative environmental effect as it is very challenging to recycle the used composite materials, but, recent studies regarding natural renewable fibers show promising results in crashworthiness applications [34]. Additionally, the manufacturing cost of the composite materials is relatively higher than the metallic structures and this has limited their application to specific fields such as aerospace structures and race cars.

Composite shells deform in a manner different to similar structural components made of conventional materials (metals, polymers), since micro-failure modes, such as matrix cracking, delamination, fiber breakage etc., constitute the main failure modes of these collapsed structures. Therefore, this complex fracture

mechanism renders difficulties to theoretically model the collapse behavior of fiber-reinforced composite shells. Unlike ductile metals and thermo-plastics, the fibers and resins are brittle and they fail by fracture after an initial elastic deformation.

The composite material components (fibers and matrix), as well as the laminate design (fiber orientation), greatly affect the crashworthy capacity of structures made of composite material. Fiber content, diameter and length, matrix mechanical properties, as well as the fiber distribution in the laminate, have a significant influence on the energy absorption capability of thin-walled composite shells geometry subjected to axial loading.

### 1.3.1. Composite material

Most composite tubes are made of high strength fibers, i.e. glass, carbon and Kevlar®, embedded in a rigid cross-link matrix such as epoxy resin. In the last years the use of a thermoplastic polyetheretherketone (PEEK) matrix has shown exceptionally high SEA results [35].

In Figure 1.10 are illustrated typical values of the specific energy absorption for some metals and polymer composite materials, namely, carbon fibers in PEEK matrix (carbon/PEEK), carbon fibers reinforced plastic (CFRP) epoxy, glass fibers reinforced plastic (GFRP) epoxy, and chopped strand glass fiber mat-reinforced polyester composites (SMC) [26]. The high value of SEA for carbon fibers in a PEEK matrix (almost 200 kJ/kg) is attributed to the high fracture toughness of the PEEK matrix inhibiting crack growth, preventing this failure mode until the onset of stable progressive crushing (this will be explained later). However, the cost of PEEK is relatively high in comparison to epoxy [36] and is noted that in the process one can encounter high pressures and temperatures and difficulty with fiber wet-out [37].

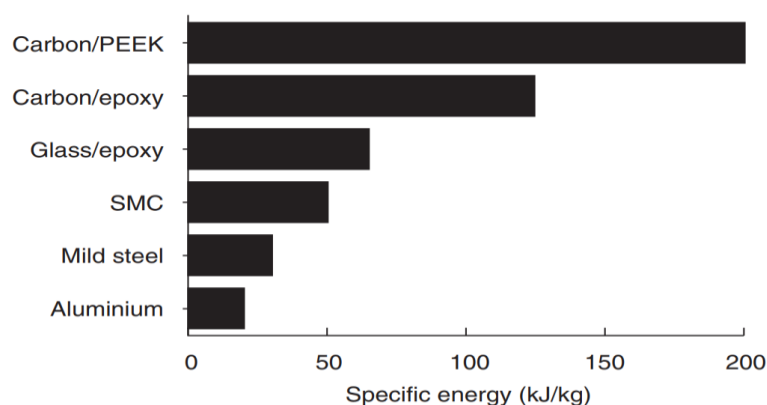


Figure 1.10: Typical values of SEA for different materials [26]

Along with the fiber stacking sequence, fiber orientation and form (whether unidirectional, woven fabric or braided fabric) are all important factors in the energy absorption behavior and response.

As it is as metal-energy-absorbing component, as well as for composite structures, the geometry could vary as much as designers could desire. The lengthwise shape is a major factor, it can be chosen a constant thickness or tapered tube, a frusta configuration or complicated geometry such as a racing car or aircraft energy absorprion components [38].

A great number of studies have been carried out on cross-sectional-geometry choice for a tube under axial loading, in a crashworthiness sense [39]. The simple circular and square section were the most analyzed over the years, as well as for the simplicity in building such components in the lay-up process. Thornton and Edwards [40] report that the square and rectangular cross-section tubes are generally less effective in absorbing energy than circular ones, suggesting that the corners act as stress concentrations leading to the formation of splitting cracks. This tends to result in unstable collapse with low energy absorption. In Table 1.2 some normalized values of the SEA of rectangular section are reported in respect to the circular one.

Table 1.2: Square and rectangular versus circular tube section

<i>Reference</i>	<i>Section</i>	<i>Circular tube SEA</i>
Mamalis [22], [41]	Square	0.8
Kindervater [42]	Rectangular	0.5

The geometry shape of a tube is defined by the cross-sectional (square, rectangular or circular) and lengthwise shape (tapered or constant). Geometry may also involve a triggering system such as chamfering of a tube end to initiate collapse.

### 1.3.2. Macroscopic failure mechanisms of axial loading

The brittle nature of both fiber and resin ensures that composite materials do not undergo the plastic deformation characteristic for ductile metals and PVC; the dominant mechanism in the present case is that of fracture and fragmentation.

Depending on the application of the component, the failure of it could be defined by a very small deformation, and in other cases the failure is considered by a total fracture or separation. In composite materials generally, the internal material failure initiates before any alteration in macroscopic appearance or behaviour.

The macroscopic collapse modes of thin-walled composite shells subjected to low-speed axial loading may be classified as:

- Stable progressive collapse modes associated with controlled crushing process,
- unstable collapse associated with extensive brittle fracture.

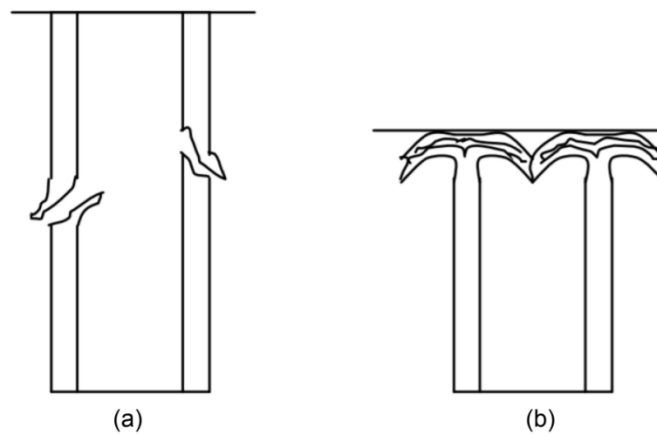


Figure 1.11: Typical collapse modes for composite tubes: (a) catastrophic failure (b) progressive failure [43]

Note that, the whole crushing process of the collapse modes of the axially loaded composite shells greatly affect the energy absorbing capability of the structural components.

After a long experimental testing campaign on FRP composite materials performed by researchers, especially Athanasios G. Mamalis [27], [44]–[46]; the following main modes of failure may be identified and classified as progressive crushing, brittle catastrophic failure and progressive folding.

### 1.3.2.1. Progressive crushing

Progressive crushing is a failure characterized by micro-fragmentation of the material, associated with large amounts of energy absorption. This failure mode is designated as Mode I failure. In Figure 1.12 are shown the definitions of material fracture modes.

and three different modes of failure were observed:

1. Mode I-A of failure, similar to a ‘mushrooming’ failure in ductile materials, is mainly characterized by progressive collapse through the formation of continuous fronds which spread outwards and inwards with the

simultaneous development of a number of axial splits at the external fronds Figure 1.13(a). This mode of collapse is observed when crushing circular and square tube, or frusta of small semi-apical angles.

2. Mode I-B of collapse is characterized by the inversion of the shell wall inwards and it is associated with axially loaded circular and square frusta of larger semi-apical angles [27].
3. Mode I-C is characterized by an outwards inversion of the shell wall and is observed only during the axial collapse of circular frusta with a  $15^\circ$  semi-apical angle. Note, difficulties to initiate progressive crushing modes in very thin- or very thick-walled shells.

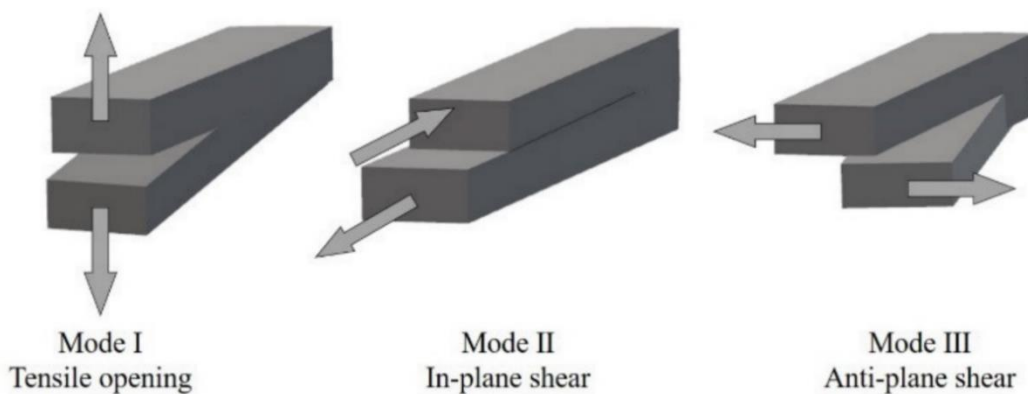


Figure 1.12: Typical fracture modes [47]

### 1.3.2.2. Brittle fracture

Brittle fracture of the component resulting in catastrophic failure with little energy absorption is designated either as Mode II or Mode III depended on the crack form.

1. Mode II is characterized by the development of a spiral or a longitudinal unstable crack propagating along the circular tube shell circumference, whilst axially collapsed square cross section are associated with the formation of longitudinal corner cracks, see Figure 1.13(b).
2. Mode III, designated as mid-length collapse mode, is characterized by the formation of circumferential fracturing of the material at a distance from the loaded end of the specimens, approximately equal to the mid-height of the shell; catastrophic failure by cracking and separation of the shell into irregular shapes is involved, see Figure 1.14

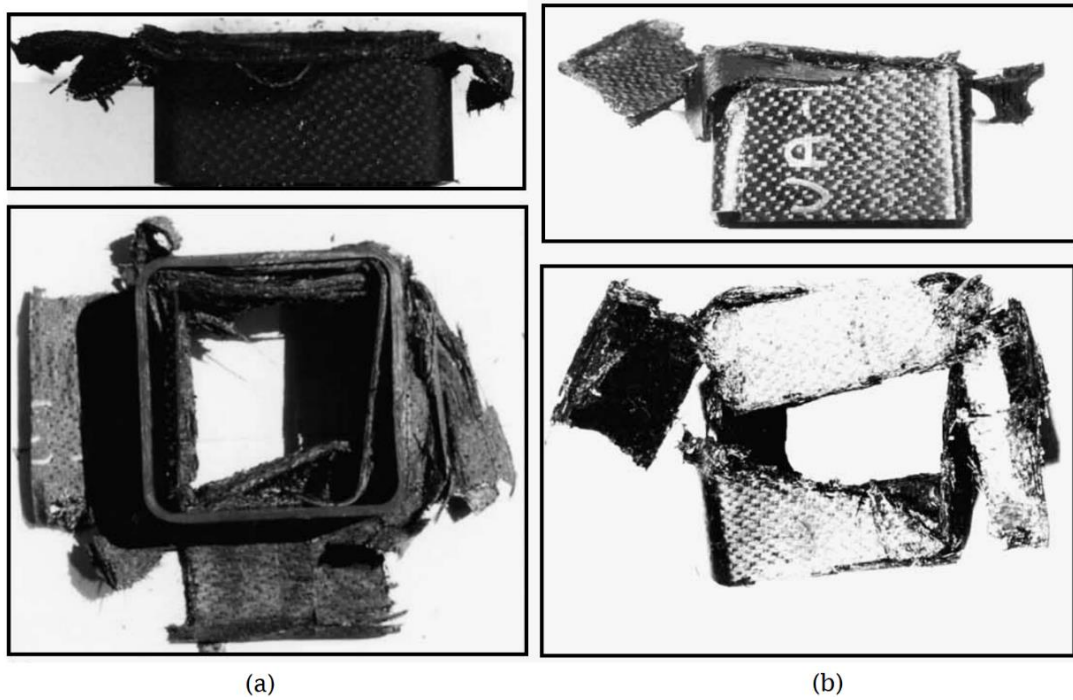


Figure 1.13: (a) Mode I-A, (b) Mode II [49].

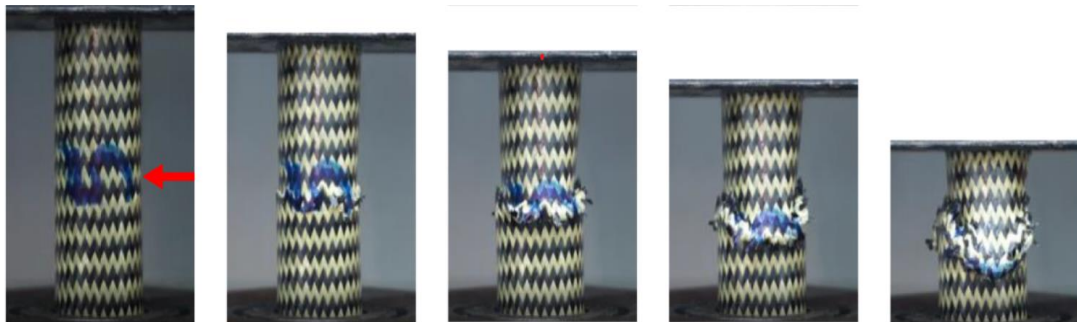


Figure 1.14: Mode III [48].

### 1.3.2.3. Progressive folding

Composite folding and hinging is a rare phenomenon, it is similar to the crushing behavior of thin-walled metal and plastic tubes. Progressive folding is designated as Mode IV and shows a very low energy absorbing capacity [27]. This mode of collapse is often associated to the axial loading of very thin tubes made of Kevlar® fibers, as shown in Figure 1.15 [49]. According to literature, Euler column buckling or progressive folding with hinge formation were not found for FRP composite tubes [50].



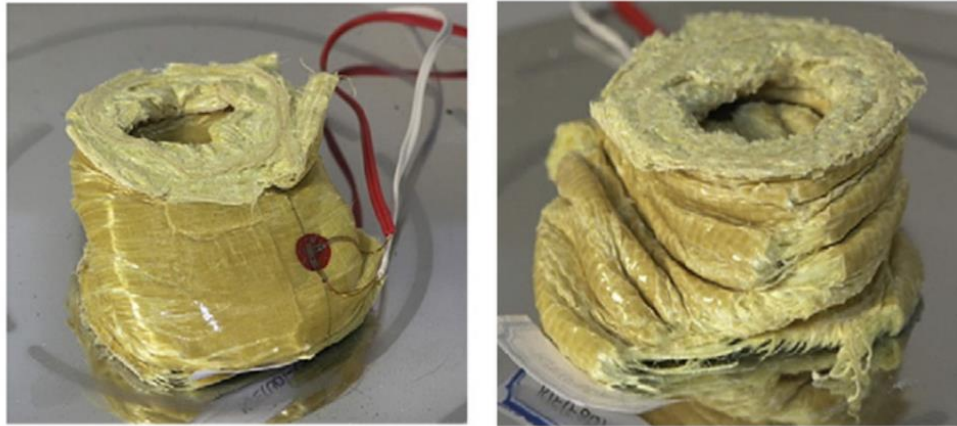


Figure 1.15: Mode IV of a Kevlar® circular tube[49].

### 1.3.3. Microscopic failure mechanisms of axial loading

Various fracture modes can be defined for a laminate composite. These modes are divided into intralaminar and interlaminar fracture modes. Intralaminar mode consists of:

- longitudinal matrix fracture,
- transverse matrix fracture,
- fibre-matrix debonding,
- fibre fracture.

Interlaminar mode is also referred to as delamination and is described as separation of layers from one another (Figure 1.16). The fracture mechanisms depend on architecture of the layers, and mechanical loading mode.

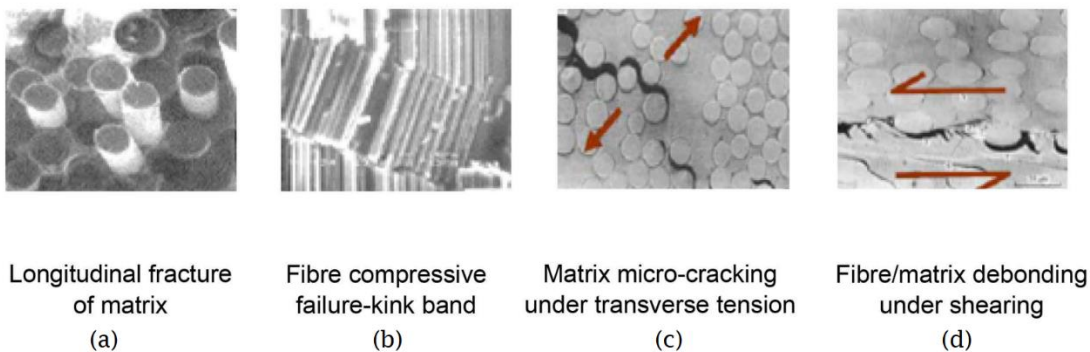


Figure 1.16: Fracture mechanisms observed in laminates [31]

Cracks generally propagate through the weakest regions of the structure of the composite material, which generally corresponds to resin-rich regions or

boundaries between hoop fibers, resulting in their debonding, or through the interface between hoop and axial plies causing delamination.

Axial loading crushing response of composite tubes can be classified into three basic modes [51]:

1. Transverse shearing or fragmentation.
2. Lamina bending or splaying.
3. Local buckling.

When a load is applied to the edge of the composite thin-walled tube, local failure of material occurs and small inter- and intralaminar cracks are formed, where their length determines whether the resulting crushing mode is transverse shearing, lamina bending or a combination of these brittle fracture modes.

### 1.3.3.1. Fragmentation

This mode is characterised by formation of fragments in the crush zone, as a result of short interlaminar and longitudinal cracks, the lengths of the interlaminar and longitudinal cracks are typically less than the thickness of the laminate.

In Figure 1.17 is shown a sketch of the fragmentation sequence for a tube with a chamfer trigger (explained in 1.3.4), starting with the crushing of the chamfer with splitting and compressive buckling in both hoop and axial directions (Figure 1.17 (b)), leading to the initial fragmentation. In the hoop direction, compressive buckling on the inside of the tube and tensile fracture on the outside of the tube occur. This process repeats itself for the full wall section (Figure 1.17(c) and Figure 1.17d).

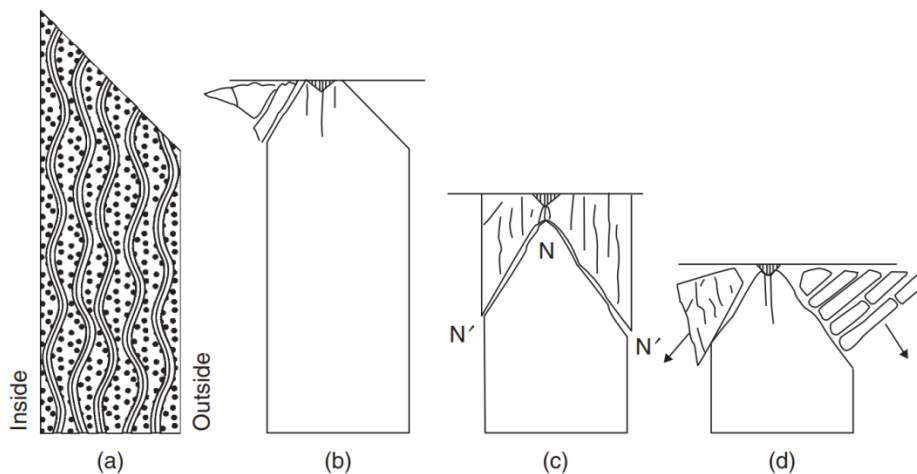


Figure 1.17: Sketch of the fragmentation sequence [21].

Transverse shearing mode is characterized by the laminate wedge-shaped-cross section with a single or multiple short interlaminar and longitudinal cracks. In this mechanism, the energy absorption is controlled by the interlaminar crack propagation and bundle fracture. The bigger is the bundle, the less is the energy absorbed because less material is cracked and less energy is adopted in the fragmentation phenomena.

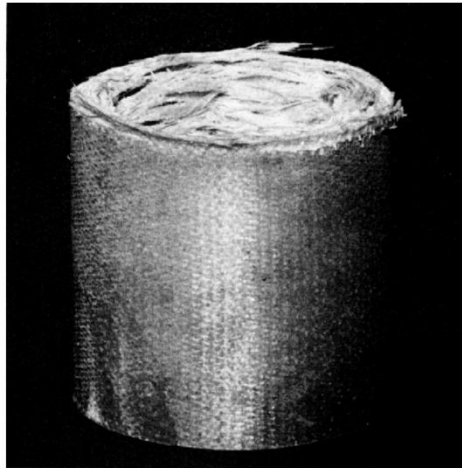


Figure 1.18: Post crushing picture of fragmentation mode by a woven GFRP tube [50]

### 1.3.3.2. Splaying mode

In the case of the lamina bending crushing mode, the lengths of the interlaminar and longitudinal cracks are typically very long, and parallel to fiber; their lengths are greater than ten laminate thicknesses. As showed in Figure 1.19(a), the lamina bundles do not fracture and fold inside and outside the tube.

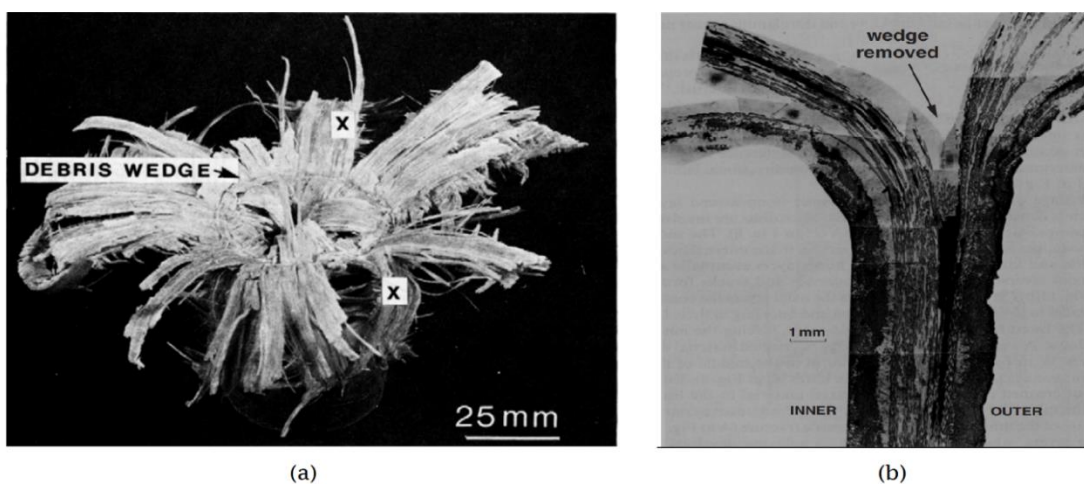


Figure 1.19: Details of lamina bending mode [21].

In the case of brittle fracturing crushing mode, the lengths of the interlaminar cracks are between one and ten laminate thicknesses.

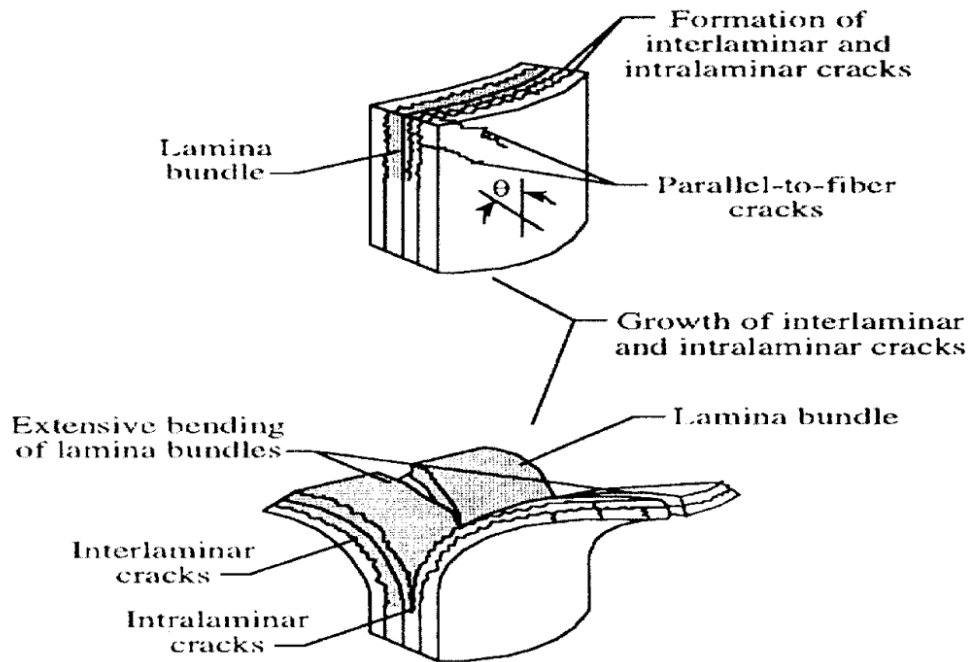


Figure 1.20: Splaying crushing mode [51].

Literature states that splaying microfracture mechanism of square, circular and hour-glass sections tube are similar ([46], [52]). The main features of this microfracture mechanism are shown in Figure 1.21, and despite the presence of a chamfer trigger, the phenomenon is the same for tube sections without such bevel [50]:

1. an annular wedge of highly fragmented material, forced down axially through the shell wall, Figure 1.21(b).
2. An intra-wall microcrack which develops ahead of the crush-zone at the apex (tip) of the annular wedge and propagates at a rate approximating the compression rate, Figure 1.21(c).
3. The central bundle wedge causes a ply delamination in the crush zone, which results in two continuous fronds that spreads radially inwards and outwards from the wall of the tube Figure 1.21(d). Note that a severely strained zone is created between the central crack and the shell wall edges showing a combined tensile-compressive type of deformation.

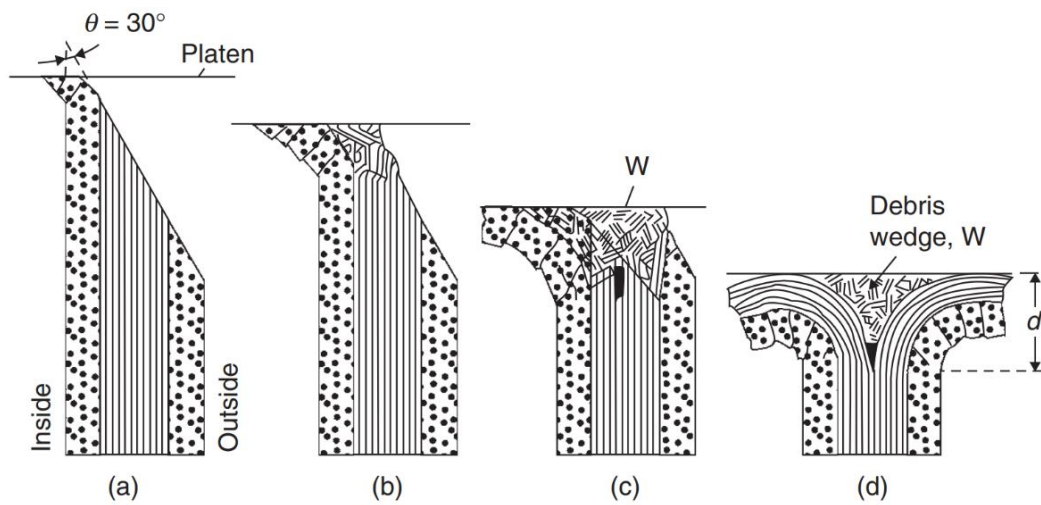


Figure 1.21: Splaying mechanism [50].

### 1.3.3.3. Brittle Fracturing

The brittle fracturing crushing mode is a combination of fragmentation and splaying crushing modes, resulting in a fragmentation of the internal material of the laminate and a splaying of the top and bottom layers of the composite shell (see Figure 1.22). This crushing mode is exhibited by brittle fiber reinforcement tubes, which main energy absorption mechanism is the fracturing of lamina bundles. When brittle fracturing occurs, the lengths of the interlaminar cracks are between 1 and 10 laminate thickness [53].

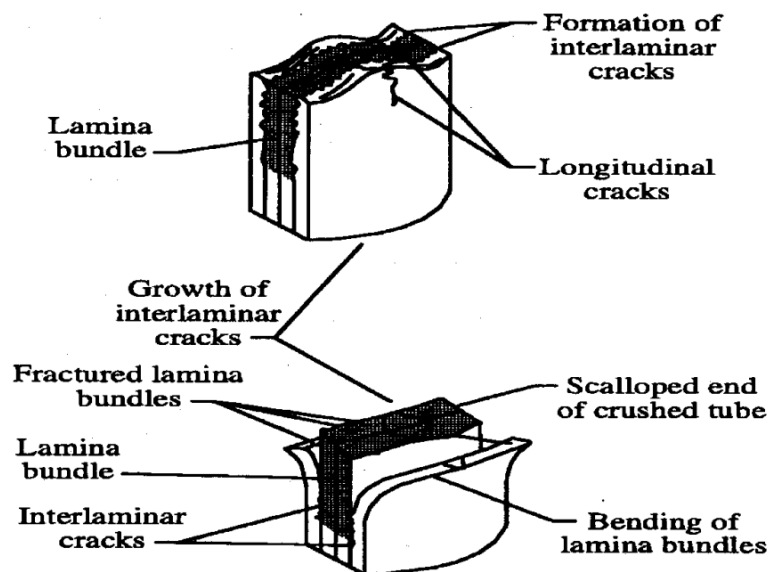


Figure 1.22: Sketch of brittle failure mode [51].

#### 1.3.3.4. Local buckling

The last crushing mode consists of the formation of local buckles by means of plastic deformation of the material, as sketched in Figure 1.23. The post-crushing integrity of ductile FRP composites is a result of fiber and matrix plasticity, i.e. significant deformation without fracture, and fiber splitting.

FRP materials exhibit the local buckling crushing mode when:

1. The interlaminar stresses are small relative to the strength of the matrix.
2. The matrix has a failure strain higher than the fiber.
3. The matrix exhibits plastic deformation under high stress.

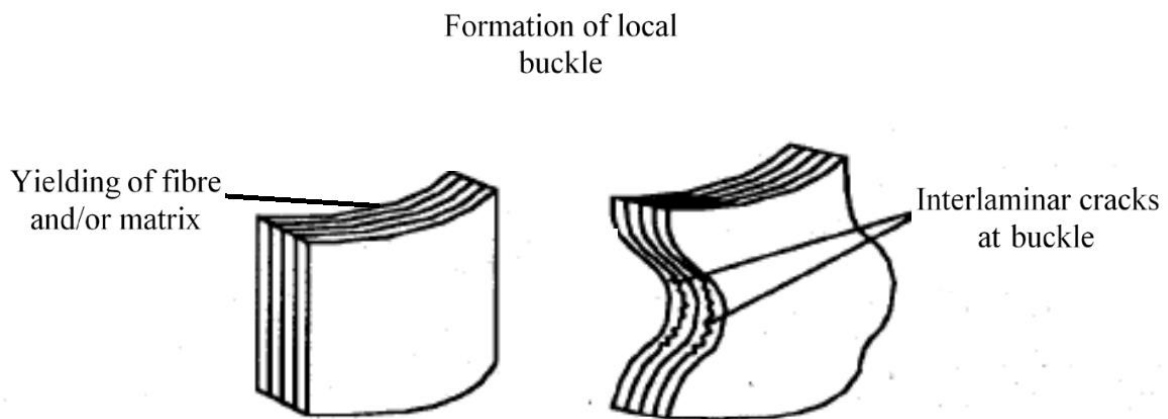


Figure 1.23: Local buckling micro-mechanism [51].

As mentioned earlier, this ductile behavior is typical for Kevlar® composite and in some cases brittle FRPC materials exhibit similar behavior.

The mechanisms that control these different crushing modes are a function of the mechanical properties of the constituent materials and the structure of the specimen:

- In the case of transverse shearing, interlaminar crack growth and lamina bundle fracture are the crushing mechanisms, whilst inter/intralaminar crack growth and friction are the mechanisms in the lamina bending crushing mode.
- The mechanisms that control the crushing process in the local buckling crushing process are plastic yielding of the fiber or/and the matrix.

By understanding the micro-mechanism and failure mechanisms experienced during collapse, the following principal sources of energy dissipation at microscopic scale may be listed [44]:

1. Intra-wall crack propagation,
2. fronds bending due to delamination between plies,
3. axial splitting between fronds,
4. flexural damage of individual plies due to small radius of curvature at the delamination limits,
5. frictional resistance to axial sliding between adjacent laminates,
6. frictional resistance to the penetration of the debris wedge,
7. frictional resistance to fronds sliding across the platen.

### 1.3.4. Trigger Mechanism

Triggering is a process that initiates failure and avoids load transfer to the whole structure by formation of stress concentration on edges of the profile geometry. Triggering mechanisms prevent composite structures from crushing catastrophically. A suitable selection of triggering helps initiating a progressive crushing so the crush load is at a relevant constant value due to various fracture mechanisms such as splaying, fracture modes, etc [31].

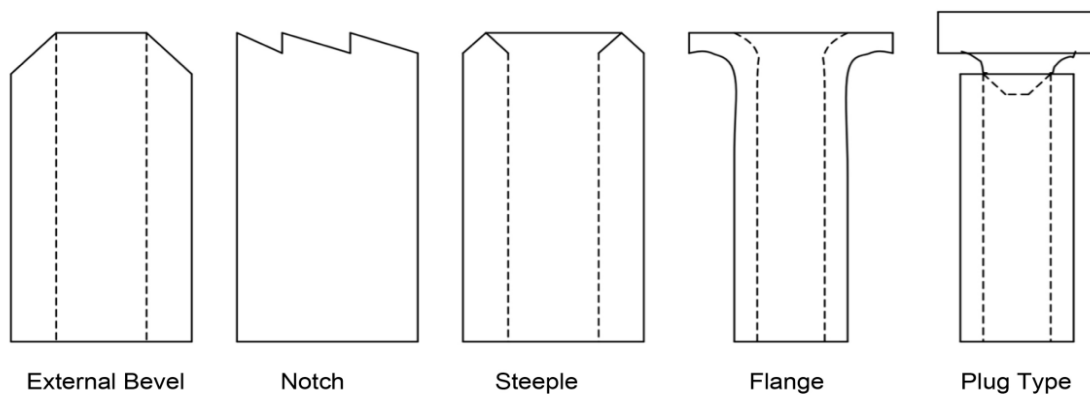


Figure 1.24: Various type of mechanisms [54]

In order to obtain a response of a crushing tube similar to the ideal square-wave type of load, it is necessary to ensure that brittle macro-fracture or buckling instability will not occur. It has been established that this cannot be achieved with tubes having square ends, and a trigger mechanism is needed to promote a form of progressive crushing. It is reported [40] that modifying one end of the tube, by introducing a chamfer, can greatly reduce the peak load experienced by the specimen without affecting the sustained crushing load, see Figure 1.25.

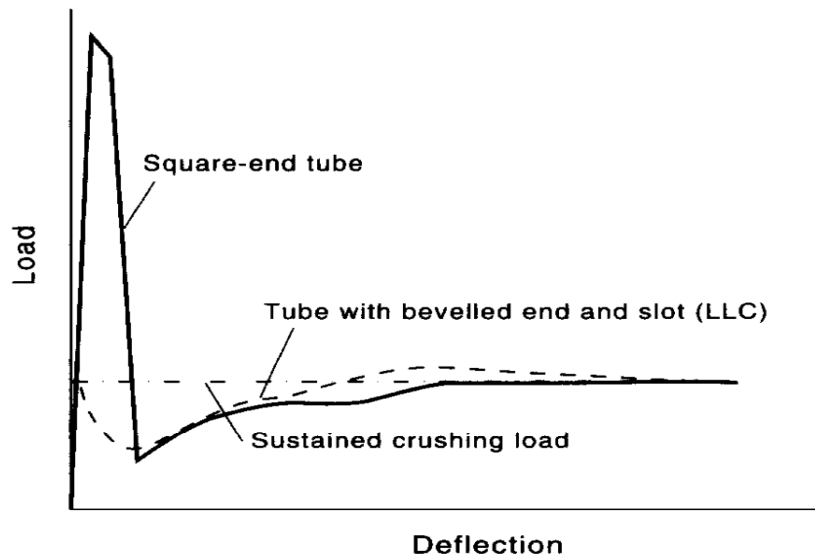


Figure 1.25: The effect of a collapse trigger mechanism [40]

### 1.3.5. Fiber Orientation

In general, the behavior of the reinforcing fibers depends upon their orientation, where  $\theta$  is the angle between the fibre direction and the longitudinal axis of the tube, see Figure 1.26. As global behavior, it can be stated that:

- Axially aligned fibers ( $\theta = 0^\circ$ ) are subjected to splaying mode, according to their flexibility and the constraints induced by other fibers. Their effective flexibility depends upon the fiber arrangement in the composite material.
- Fibers aligned in the hoop direction ( $\theta = 90^\circ$ ) can only expand outwards by fracturing and inwards by either fracturing or buckling.
- Changes in section lay-up which lead to an increase in modulus lead to higher crush strengths and energy absorption. However, such changes must be balanced against an increased tendency towards delamination and unstable collapse [40].

Considerable research has analyzed the ways orientation influences the axial impact of composites tubes:

A stable collapse a  $[45/-45]_n$  layup resulted in obtaining lower energy absorption value than  $[0/90]_n$  lay-ups [40].

Furthermore, the SEA generally increases in  $[0/90]$  aramid-epoxy and glass-epoxy circular tubes for  $45^\circ < \theta < 90^\circ$ , with increasing of  $\theta$ .



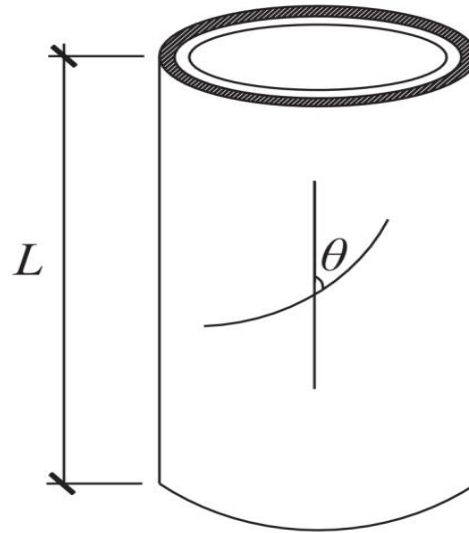


Figure 1.26: Definition of fiber orientation of a circular tube [55].

It is reported that variations in SEA of carbon-epoxy, glass-epoxy and aramid-epoxy  $[0_2/\pm\theta]$  specimens all generally increase with increasing  $\theta$  [28].

Specimens made of a commercial glass fiber and vinyl ester composite material, which consists of nine plies in the sequence of  $[(90/0/2R_c)/(2R_c/0/90)/R_{c75}]$ , show better energy absorption behavior than those made of a glass fibre composite material in which the glass fibers were in the form of chopped-strand mat with random fiber orientation in the plane of the mat[52].

Composite circular tubes were E-glass plain woven fabric and epoxy resin, under quasi-static axial load. The fabric is laid with different angles ( $0^\circ$ ,  $15^\circ$ ,  $30^\circ$ ,  $45^\circ$ ,  $60^\circ$  and  $75^\circ$ ). Results showed that the post-crushing behavior  $15^\circ/-75^\circ$  fiber orientation is not as steady as for the  $0^\circ/90^\circ$  or the  $45^\circ/-45^\circ$  fiber orientation. The visual observations showed a catastrophic failure mode immediately after reaching the maximum pre-crushing load, for the specimens of  $15^\circ/-75^\circ$  and  $75^\circ/-15^\circ$ . In addition to the load capacity, the results of the absorbed energy showed an advantage of the specimens with  $15^\circ/-75^\circ$  and  $75^\circ/-15^\circ$  fiber orientations [28].

The relative strength in the axial and hoop directions is a key factor in the fragmentation mode of collapsing.

For tubes made from a series of glass cloth prepreg materials, when the number of the hoop fibers (H) is large compared to the axial ones (A) (say H:A between 4:1 and 8.5:1), micro-fragmentation occurs. On the other hand, when the hoop constraint is weak (H:A between 1:7 and 1:8.5), no axial fiber fracture and splaying occurs. Gradually increasing the hoop resistance leads to a sharper micro-bending (with a small radius) and eventually fracture of the axial fibers [21].

### 1.3.6. Strain Rate Sensitivity

In metallic materials the stress induced from low velocity impact due to ductile nature and high potential of energy absorption may not be considered threatening. However, in composite materials at micro-scale level, low velocity impact may induce significant damages, resulting in reduction of strength and stiffness of the material [54].

Extensive work of many researchers has been studied to investigate the influence of strain rate on energy absorption of composite thin-walled structures. Researchers [56] reported that matrix stiffness and failure strain are a function of strain-rate. The energy absorption of interlaminar crack growth (delamination) may be considered as a function of crushing speed. Despite significant experimental work has been carried out on static and dynamic crushing, still conflicting results were produced [27].

Energy absorption capability of circular carbon-epoxy tubes is greatly dependent on the strain at failure of both the fiber and the matrix of the material systems tested [57]. Moreover, the friction coefficients between the various sliding surfaces during the crushing process may be influenced by changes in crushing speed.

Later Farley [56] reported that in  $[0, \pm\theta]_2$  carbon-epoxy tubes, the energy absorption is not a function of crushing speed. It was also found that the energy absorption in  $[\pm\theta]_3$  carbon-epoxy specimen is a weak function of crushing speed (over the speed range  $0.01 - 12 \text{ m/s}$ ), which resulted in an increase in energy absorption of around 35%. On the other hand, another study on carbon-epoxy tubes 20% degradation in EA capability under impact loading of up to  $9 \text{ m/s}$  [41].

Energy absorption dependence on crushing speed is related to the mechanism which controls the crushing process.

Quasi-static tests conducted on the composite nose cone of a Formula One racing car, the failure mechanism is one of global buckling of the composite skins rather than the progressive crushing and high energy absorption associated with dynamic impact of the cone [58].

Care should be exercised when using static test data to predict dynamic behavior.

## 1.4. Hybrid material crushing tubes

Although metals and composites have lots of beneficial properties, they also have some disadvantages limiting their potential applications. Composites, compared to metal alloys, display high mechanical properties: static strength, high stiffness, low density, chemical and corrosive resistance.

The disadvantages of composites include low formability, cold cracking and velocity impact resistance, moisture absorption, and relatively low operating temperature. Therefore, it is a challenge to produce a material retaining the features of both, metal component and fiber-reinforced polymer composite. Fiber metal laminates (FML) are hybrid materials complying to the above mentioned requirements [59].

#### 1.4.1. Advantages and Applications of FML

Over the years, researchers have analyzed the behavior of FML with the aim to develop a new aircraft material with a better fatigue resistance and preferably a higher specific strength and lower density.

Fiber metal laminates have been developed for the aircraft industry at the Delft University of Technology, and the only FML materials used so far on an industrial scale are GLARE laminates (Glass LAMinates REinforced), which corresponds at a precise stacking of GFRP and aluminum sequence.

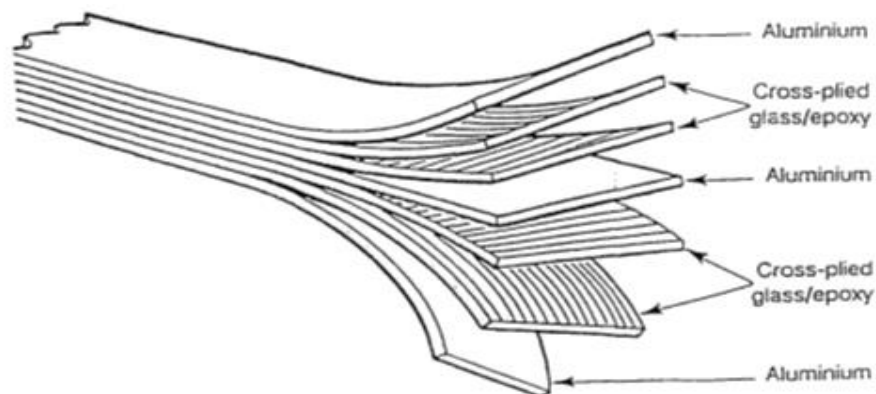


Figure 1.27: build-up of a cross-ply GLARE laminate [60]

GLARE has proven great material mechanic/response in fatigue and impact normal to shell surface, thanks to the material characteristic of both aluminum and GFRP. Advantages of fiber metal laminates depending on previous investigations are summarized in Table 1.3.

On the other hand, a long processing cycle to cure the matrix in composite plies is the major disadvantage associated to epoxy-based fiber-metal laminates. This long curing time increases the cycle time of whole production and decreases productivity [61].

The impact characteristics also make GLARE an excellent material for impact sensitive areas, such as: the cockpit crown, forward bulkheads, the leading edge.

Table 1.3: Advantage of FML [62]

<b>High strength</b>	[61]	FMLs are hybrid structures based on thin metal alloy sheets and plies of fiber-reinforced polymeric materials. Metal and fiber reinforced composites both which have high strength and stiffness result in high strength and stiffness of FML.
<b>Low density</b>	[63]	Due to the presence of thin layers of metals and composite plies, FML has low density. Therefore, FMLs are a weight - saving structural material compared to others
<b>Excellent corrosion resistance</b>	[64]	FML gives excellent moisture resistance and high corrosion resistance because it is polymer based.
<b>Excellent moisture resistance</b>	[65]	Due to the presence of metal layers at outer surface the moisture absorption in FML composites is slower when compared to polymer composites, even under the relatively harsh conditions. Additionally, prepreg layers are able to act as moisture barriers between the various aluminum layers inside the FMLs.
<b>High fatigue resistance</b>	[66]	It gives high fatigue resistance because of intact bridging fibers in the wake of the crack, which restrain crack opening. FMLs have excellent fatigue characteristics over conventional metal and composite.
<b>High energy absorbing capacity</b>	[66]	Based on investigation data, FMLs absorb significant energy through localized fiber fractures and shear failure in the metal plies.
<b>High impact resistance</b>	[66]	Impact deformation is actually a significant advantage of FMLs, especially when compared to composites

Most of these components have already been considered and investigated by several manufacturers.

The riveted joints in pressurized fuselages are exposed to severe fatigue loading in both the longitudinal and circumferential directions. It is necessary to fit the severe and biaxial-load conditions in the fuselage skin for the industrial application. Cross-ply build up GLARE, with excellent fatigue resistance, higher tensile strength and lower density. It is a better choice compared to monolith aluminum as a fuselage skin material [67].

The literature about GLARE is deep regarding crack growth and impact testing, but axial loading tube is still new and studies available to the public are few. On

the contrary, crashing testing and numerical analysis regarding simple coupling of composite-ductile material is a field where more information is already available.

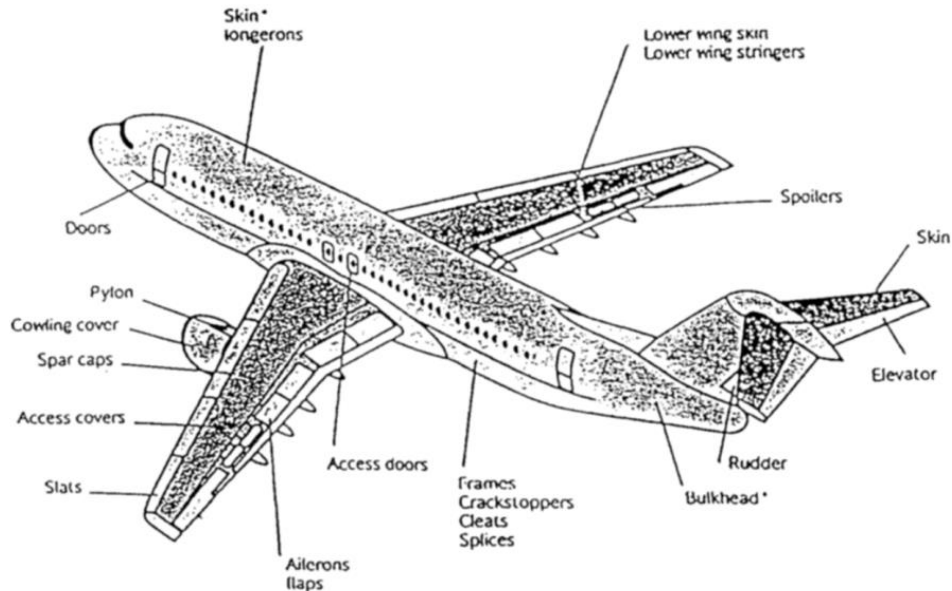


Figure 1.28: Candidate area for aeronautical GLARE

#### 1.4.2. FMLs under axial crushing load

Many researchers have worked with hybrid structures to absorb a greater amount of energy, such as composite wrapped thin-walled metal tubes or tubes reinforced with externally bonded fibers. It is found that hybrid structures combine the desirable properties of each material, the high ratio of strength to the weight of the composites and ductility and stable plastic deformation mode of the metals [68].

Note that the majority of the research is performed considering the quasi-static axial loading of tubes, and few perform impact tests.

The axial crushing of GLARE structure exhibited a mixed mode crushing phenomenon, where the crushing modes are a combination of its constituent (GFRP and Aluminum).

It is reported that top-hat FML structure under axial load shows predominant failure modes during crushing, highlighted in Figure 1.29 [69]:

1. delamination of the layers in FML,
2. splaying of the metallic layers (this failure mode is uncommon to thin metals, it is more associated with composites),
3. formation of corrugations (this damage pattern is typical of metallic structures under axial crushing loads),

4. a wide range of compressive failure modes of the composite layers (matrix debris, fiber and lamina failure).

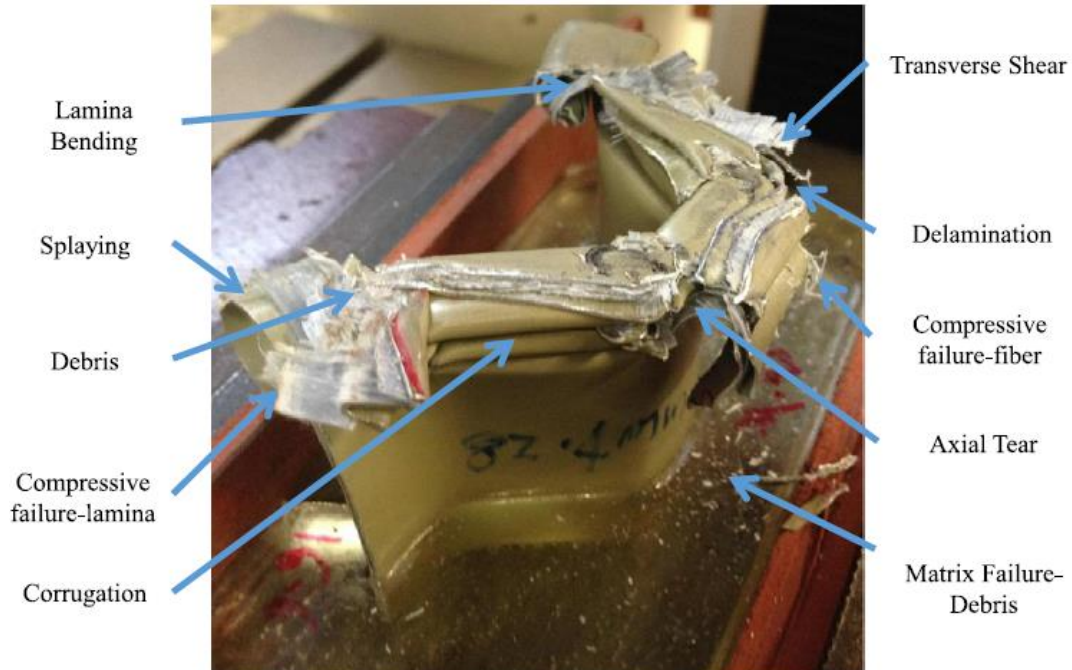


Figure 1.29: Crushing failure modes top hat GLARE structure [69].

The study reported that MCF and EA capacity of GLARE top-hat structures are superior to the equivalent bare aluminum structure by 9% and 16% respectively [69].

Despite the superiority of composite, bare composite conical frusta may collapse catastrophically under complex impact load conditions, which can lead to low EA.

Results [70] proved that the FML conical shells yielded more specific energy and higher energy-absorption capacity when compared to bare aluminum metallic frusta. However, it is found that corresponding SEA of bare composite is higher than the sum of bare metal and bare composite, as well as the FML composite wrapped aluminum conical (CWAC in Figure 1.30). On the contrary aluminum wrapped composite conical (AWCC in Figure 1.30) FML configuration had the highest SEA, which is due to different collapse modes [71]. Thus, the hybrid conical frusta with appropriate material combinations is capable of improving the EA capacity of composite structure.

The thickness of the FRP is shown to be an important parameter affecting the crushing mode. For AL-CFRP hybrid tubes, the SEA of hybrid tubes increased with the increase in the CFRP wall thickness or decrease in the AL wall thickness [72].

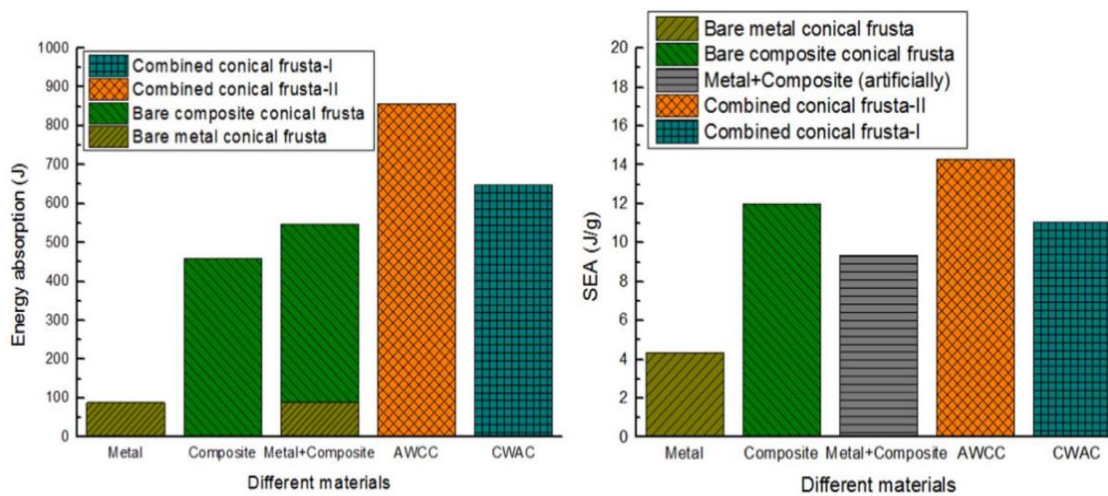


Figure 1.30: Comparison of EA and SEA among bare specimen and hybrid specimens [71].

Another study on square AL tube wrapped by braided CFRP layers with  $45^\circ$  fiber [7], showed an unexpected deformation of the composite during the crush. Both the constituent experienced an inextensional folding, typical deformation mode of a pure aluminum square tube; Figure 1.31.

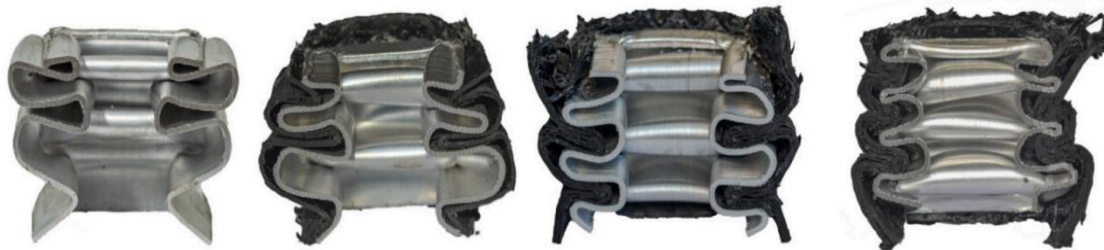


Figure 1.31: Collapse of square FML with different CFRP thickness [7].

Plastic dissipation is the main type of energy dissipation for both the aluminum and AL-CFRP hybrid tubes. Delamination and friction dissipation were only a small part of the total energy dissipation.

An interesting type of FML tube was manufactured using only one single piece of aluminum sheet. It is cut and rolled up between two prepregs CFRP lamina and another hybrid tube is produced with GFRP, Figure 1.32. Results show that both AL-CFRP and AL-GFRP tubes split into fronds and curled up. The axial splitting indicated strong interaction between CFRP layer and aluminum, prevented the uncoordinated deformation of two different materials. This FML design did not improve the energy absorption capacities under quasi-static crushing, respect to FRP. The main reason is the low- weight efficiency of aluminum layer.

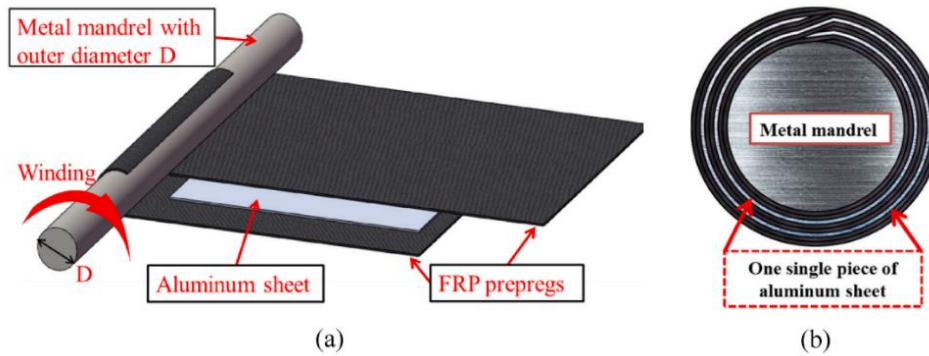


Figure 1.32: (a) Lay-up design, (b) Schematic of the cross profile [73].

Few researchers stated that the composite wrapping of metallic column show that the outer CFRP layers are bent externally with formation of considerably large fragments during crushing process. This might result in a relatively lower damage level of CFRP [74]. The configuration of such a hybrid structure may not take a full advantage of the composite crushing characteristic, therefore they explore the outer and inner composite lamination. Another study [75] analyzed two circular tubes hybrid configuration, external and internal CFRP lamination on AL tube, and compare the FML with the bare material tubes. As expected, the crash of external lamination creates big chunks of laminates that do not collaborate in the crushing. In addition, the internal AL folding delaminates the composite before the brittle failure of the composite Figure 1.33(a). On the other hand, the internal lamination results in an external inversion mode of the AL tube and the intern CFRP absorb energy in a brittle fragmentation mode Figure 1.33(b).

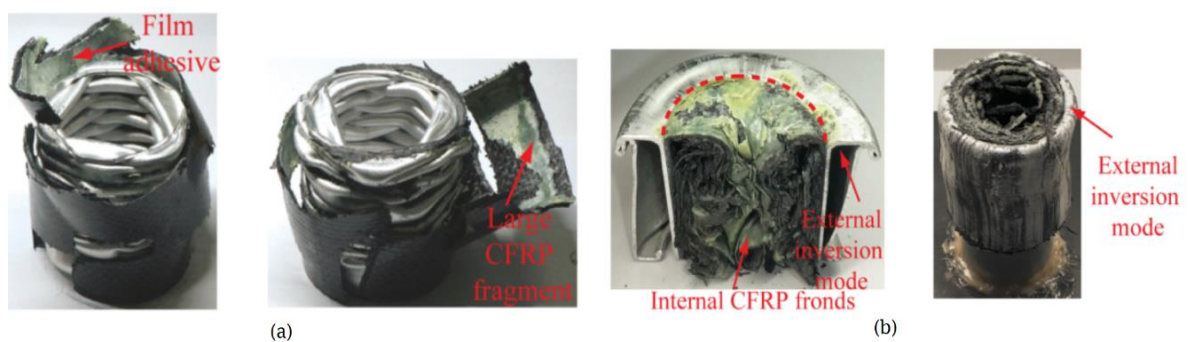


Figure 1.33: (a) External lamination and (b) internal lamination collapsing mechanism [75].

Furthermore, the SEA of external-laminated hybrid is higher than the other configuration and close to the relative bare CFRP tube, but composite components perform better considering the SEA.

Since the topic has been recently developed in comparison to composite and ductile material, an intensive study is performed integrating numerical



simulations and multi-object optimizations. Other researchers [76] dealt with hybrid circular tubes under quasi-static loading, and affirm that internal lamination performs better than external or mid lamination on AL tubes. In addition, [77] circular tubes perform better than other geometry (Figure 1.34), which was confirmed numerically. It therefore defines the best configuration (thickness and diameter of both woven-CFRP and AL) through an optimization analysis. After the optimization, numerical results state the hybrid tube (internal lamination) has a better SEA than a bare composite tube and also a higher SEA per cost.

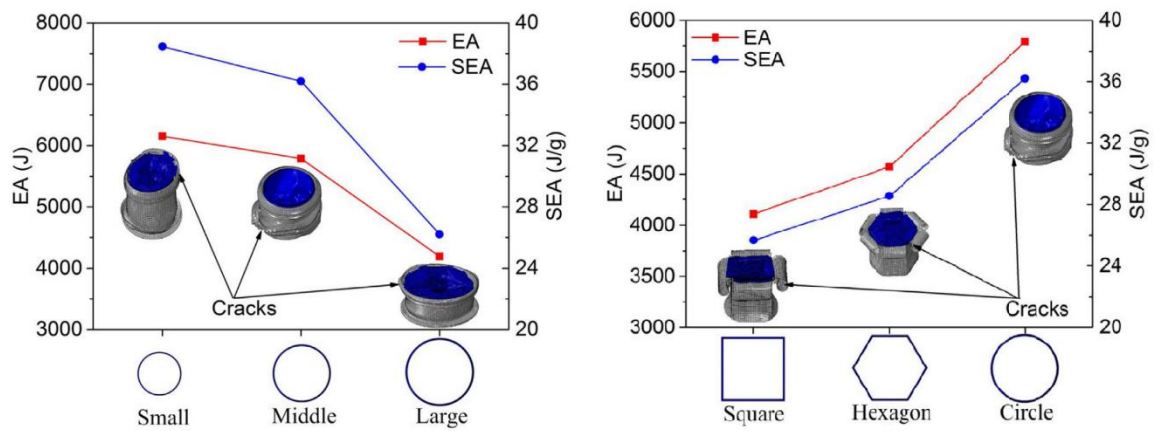


Figure 1.34: Comparison of EA and SEA with (a) different section sizes; (b) different sectional shapes [77].

## 2 Manufacturing

This chapter will present each phase needed to prepare all the components that will be tested in dynamic and static condition.

### 2.1. Materials and Components

It was decided to analyze the difference in the crushing response of inner and external lamination of an aluminum tube. Therefore, two types of hybrid tubes and two composite tubes were needed to be produced with the dimension of the external and internal laminate.



Figure 2.1: Render of the hybrid tube

A fabric prepreg CFRP lamina was chosen as composite material. Prepregs are easier in the layup phase especially if it meant to be stretched out on tube geometry. Therefore, woven fabrics are thicker than unidirectional lamina and fabrication of thick composites is less insensitive and less prone to assembly error [31].

The material is identified by the code TC2003T125/M79, and material characteristics are listed in Table 2.1.

HexTow® AS4 carbon fiber is a continuous, high strength, high strain, PAN based fiber available in 3,000 (3K) filament count tows. This fiber has been surface treated and can be sized to improve its interlaminar shear properties, handling characteristics, and structural properties.

Table 2.1: Fabric prepreg description

<b>Type of yarn</b>	HexTow® AS4C GP 3K
<b>Nominal weight</b>	200 $g/m^2$
<b>Weave style</b>	Twill 2/2
<b>Nominal cure ply thickness</b>	0.2 mm
<b>Matrix</b>	M79 epoxy resin
<b>Resin percent volume</b>	42%

HexPly® M79 is a formulated epoxy resin matrix, specially designed for prepreg applications where cure temperature is low. It cures from temperatures as low as 70°C. The matrix is highly tolerant to a wide variety of production techniques and process conditions.

As ductile material is considered an aluminum alloy 6060, the circular tube is provided by Migliari Alluminio s.r.l., the geometry and material characteristic are given by the company. Obviously, the diameter and thickness are picked in the catalog in order to be comparable to the previous works analyzed. Dimension and mechanical features are listed in Table 2.2

Table 2.2: AL tubes features.

<b>External diameter</b>	70 mm
<b>Thickness</b>	1.5 mm
<b>Density</b>	2.7 $kg/dm^3$
<b>Young modulus</b>	6700 $kg/mm^2$
<b>Treatment</b>	Hardened, annealed



Figure 2.2: Aluminum tubes.

In order to create a better adhesion between the constituents of the hybrid, a structural adhesive at the interface between aluminum and the first lamina was applied. In the manufacturing of the FML tube, an epoxy resin film was applied. 3M Scotch-Weld® is a structural thermo-setting adhesive film which is designated for both solid panel and honeycomb sandwich construction. Figure 2.5(a) shows the result after the application.

## 2.2. Lay-up procedure

### 2.2.1. Tube manufacturing

The fiber orientation during the lay-up is  $\theta = 0^\circ$  and the number of plies of the tube laminate is 15. These values are chosen because of similarity to the results of an optimization research [77].

The total length of the tubes is 150 mm. This length is chosen to be more practical during the process of the internal lamination.

This study differs from others due to the will of laminate directly inside the AL tube instead of manufacturing a composite tube and gluing the ductile component inside.

In order to facilitate the application of the internal lay-up process, sheets of fabric composite are cut for each layer of the coating and each layer overlaps by a minimum quantity (2-3 mm). The lay-up is sketched in Figure 2.3.

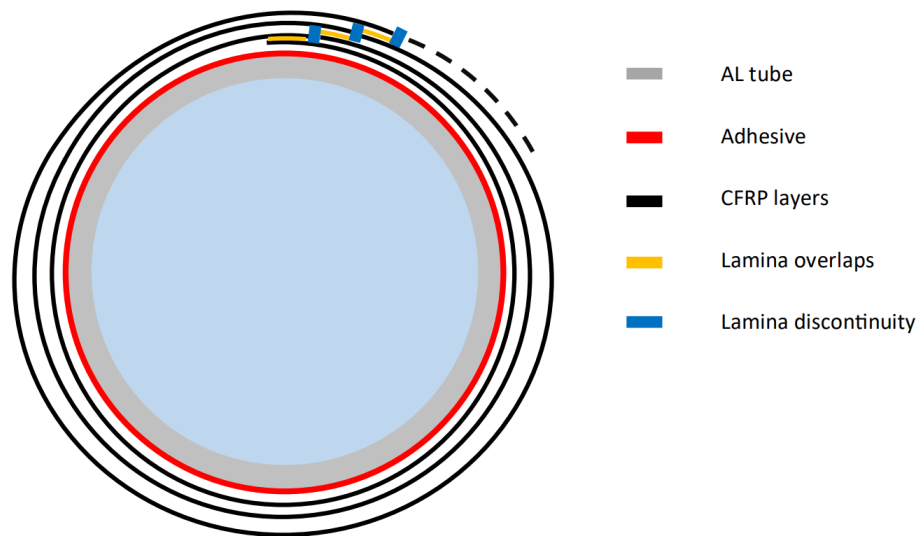


Figure 2.3: Cross sectional sketch lay-up

The procedure of manufacturing the hybrid tube and the CFRP tube is the same because the AL tube will function as mandrel. However, for the construction of the bare composite component, the adhesive is obviously not applied, and it must be removed after the curing process.



Figure 2.4: Cut prepregs during the lamination.

In order to extract the mandrel, the surface must be treated with the following steps:

1. Clean the metal tube,
2. Three layers of Marbocote® RS415 ECO acting as mold sealing and primer,
3. Five layers of Marbocote® TRE 45 ECO of release agent,
4. One layer of release film.

The composite lamination will start after this procedure. Figure 2.5(b) shows the lamination after the application of the release film.



Figure 2.5: Close up picture of (a) internal application of structural adhesive, (b) the overlapping spot for external lamination.

### 2.2.2. Intermediate compaction

During the lay-up, it is good practice to compact the unfinished laminate, especially if it is made of a considerable number of laminae. In our case, two methods are adopted which depend on the internal or external lamination:

- During the external lamination process, after every two layers, the component is wrapped with heat-shrink-tape that contracts when warmed up (see Figure 2.6). The protection film of the last applied prepregs is not removed because the procedure is finalized using a heat gun pointed around the tape. Otherwise, the heat could start polymerization in the resin and interact with the tape.



Figure 2.6: Heat-shrink-tape applied during lamination process.

- During internal lamination process, a vacuum bag is prepared with an unsealed opening in order to reuse the bag without fabricating a new one. This procedure of vacuum bag is explained later. Figure 2.7: shows the blue adhesive tape that permits the opening of the bag. Despite not being permanently closed, the vacuum pressure measure is the same as a sealed vacuum bag, around 0,85 bar.



Figure 2.7: Reusable vacuum bag for mid-lamination compaction

### 2.2.3. Tensile specimen lay-up

Since the material must be characterized, the need to produce coupons to be tested is essential. Following ATSM norms [78], the thickness of the specimen to be tested is known, therefore a plain lamination is performed from which are cut the coupons after the cure in order to obtain the needed geometry.

Table 2.3: ASTM3039 specimen dimensions.

Fiber configuration	Width	Length	Thickness
Woven fabric	25 mm	250 mm	2.5 mm

In order to perform tensile test, lamination has the same fiber orientations ( $0^\circ$ ) as the CFRP tubes. However, a further lamination is made with an orientation of  $45^\circ$  to build in-plane shear test specimen.

As can be seen in Figure 2.8, on both sides (top and bottom) of the fabric sheets, are placed a layer of peel-ply tissue, to engrave the surface. This creates a better adhesion zone after the cure process to attach the GFRP tabs to the coupons.

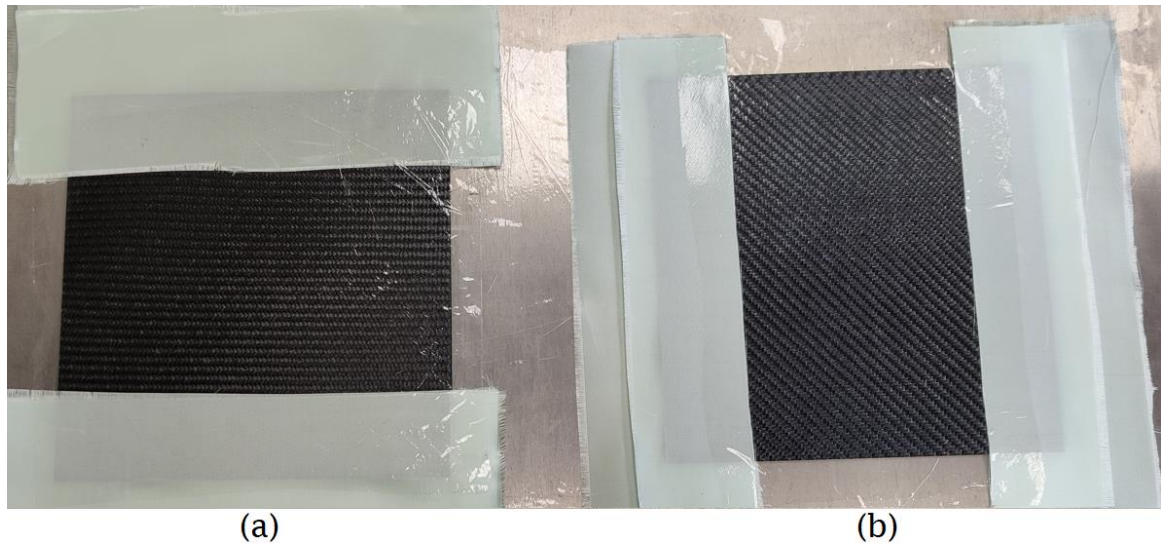


Figure 2.8: (a) 0° and (b) 45° pre-pregs lamination.

### 2.3. Autoclave curing process

The autoclave processing is one of the most common manufacturing methods for composite materials. In order to crystallize and become rigid, Epoxy resin needs to reach a certain temperature while pressure is applied on the laminate in order to maintain the same geometry of the mold meaning a circular tube.

The process still has some shortcomings, such as thermal spike in curing process, which leads to non-uniform temperature distribution. This will cause residual stress (these aspects are not investigated in the study).

#### 2.3.1. Vacuum-assisted bag molding

Circular composite tubes are usually constructed with the use of an external mold and an internal elastic bladder, to apply pressure during the cure and create an uniform surface finish [37]. In order to perform the same mechanical pressure to internal and external lamination FML during polymerization, the vacuum-assisted bag molding (VABM) method is used, where the mold is the aluminum tube. The VABM process use a sealed plastic bag which is depressurized in order to compact all lamination layers.

Thermocouple sensors are applied on the A1 tube in order to measure the component temperature inside the autoclave during the curing.

A vulcanized rubber pad is applied to create a uniform surface during the process and to avoid external irregularities due to the wrinkles of the plastic bag during the vacuum. It has the following advantages:



- easy to cut, prepare and apply on simple geometry like round tube,
- easy detachment after the autoclave process (compared to external rigid mold)
- reusable item after the curing cycle.

The rubber pad applied on the external laminated tube is shown in Figure 2.9.

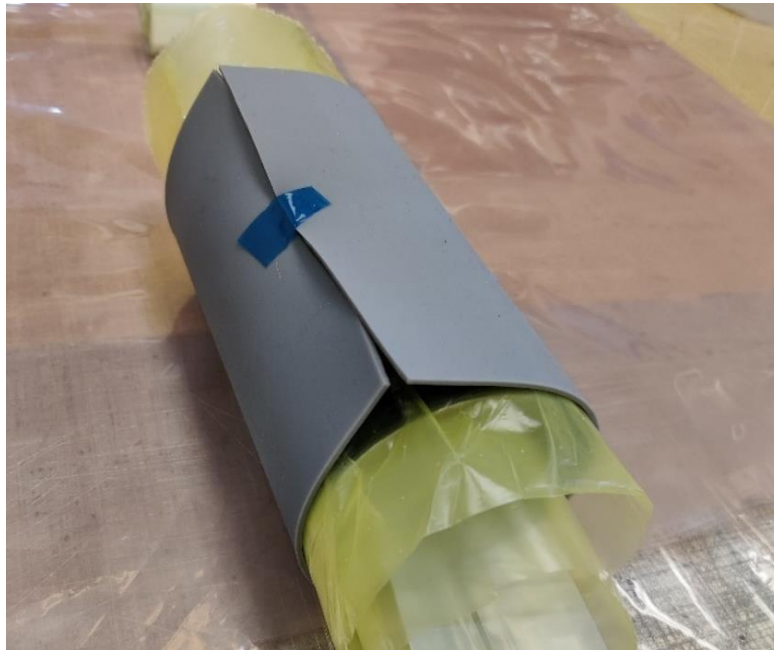


Figure 2.9: Rubber pad during the preparation of a vacuum-bag.

It must be said that during vacuum the rubber pad for internal lamination works better because it expands and stretches on the internal face of the tube. It positions itself better therefore, the pressure is uniform during the cure.

On the other hand, when the rubber is placed on the external surface of the tube (external lamination), the vacuum-bag tends to compress the pad and to create buckles on the surface. The rubber pad buckles will cause surface defects (resin pockets).

The component is placed inside a sealed plastic bag with valves to apply vacuum and compact the lamination. In order to ensure a good compaction during the process, especially for internal lamination tubes, a circular plastic “bladder” was placed inside the tube. The external and internal plastic bags are sealed together by a butyl tape. The complete and sealed vacuum-bag is presented in Figure 2.11.

A sketch of the vacuum-bag system, with all the inside elements, is shown in Figure 2.10.

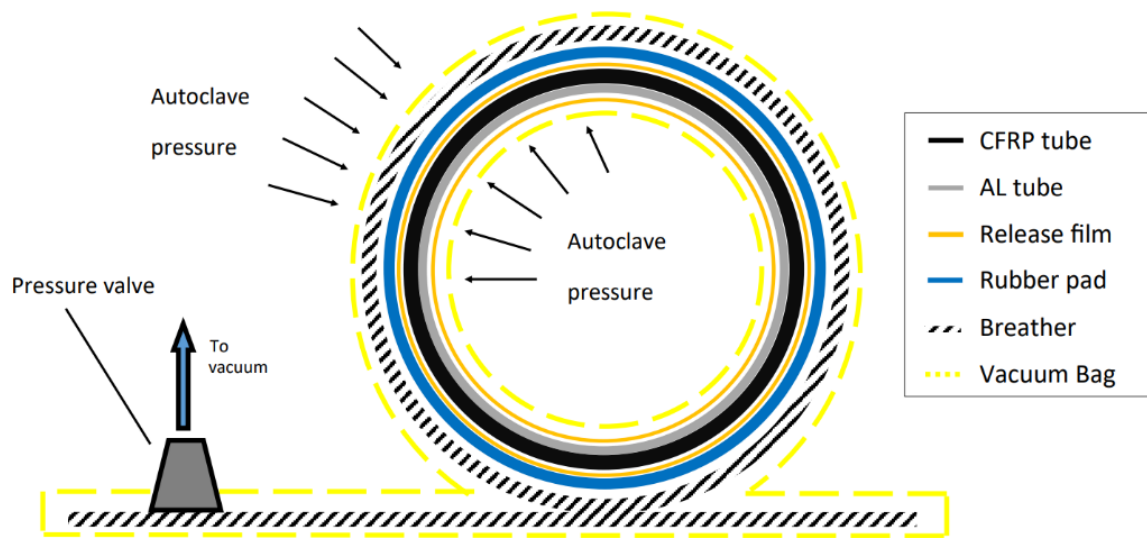


Figure 2.10: Vacuum-bag elements



Figure 2.11: Sealed vacuum-bag

### 2.3.2. Curing cycle

Once the vacuum-bag is placed inside the autoclave with all the valves and sensors connected, the curing cycle begins.

Pressure is applied on the “soft” laminated component, while temperature increases until reaching resin glass temperature and lets the matrix polymerize. During the cooling down, the matrix reaches its state of rigidity and structurally

supports the fibers. While the temperature increases, the viscosity of the resin inside the prepregs decrease, and the outside pressure applied on the laminate tends to compact the layers, thus creating a better adhesion between the elements.

The curing cycle parameters are the ones suggested by the prepregs manufacturing company for the M79 epoxy resin, which are presented in Table 2.4. These values are used for all the lamination configurations.

Table 2.4: Typical M79 epoxy cure cycle by HexPly®

<b>Heat-up rate</b>	1°C/min
<b>Cure temperature</b>	80°C
<b>Cure time</b>	360 min
<b>Pressure gauge vacuum</b>	0.9 bar
<b>Pressure autoclave</b>	3.0 bar

This type of resin, and therefore its suggested curing cycle, respects the needs of avoiding extreme temperature during the curing process to ward off excessive aluminum thermal deformation in the process.

## 2.4. Test specimens

### 2.4.1. Energy absorption tube specimens

After the curing process, the extraction from the mandril (for the bare composite tube) and the cleaning of resin deposit at the ends of the tube, the tube specimens are ready to be tested.

The components are identified with a code name to easily distinguish the type:

- C\_S is the bare CFRP tube obtained with an internal lamination and extracted from the AL tube, which acted as external mold,
- C\_L is the bare CFRP tube obtained with an external lamination and extracted from the AL tube, which acted as internal mold,
- H\_I is the hybrid tube obtained with an internal lamination,
- H\_E is the hybrid tube obtained with an external lamination.

All the bare and hybrid tubes have three specimens for each type, unfortunately, the third C\_L tube was broken during the extraction phase from the mandril. Since the remaining specimen gives consistent results in the test (see later), it was decided not to manufacture another item.

In Table 2.5 are presented the dimensions of the specimens of Figure 2.12.

Table 2.5: Geometric measure of tested tubes.

Specimen ID	$D_e$ [mm]	$D_i$ [mm]	$t$ [mm]	$m$ [g]	
C_L	1	77.1	69.8	3.5	180
	2	77.1	69.8	3.5	175
C_S	1	67.0	59.3	3.5	150
	2	66.8	59.8	3.5	150
	3	66.8	59.9	3.4	150
H_E	1	77.2	67.0	5.1	300
	2	77.1	67.0	5.1	305
	3	77.2	67.0	5.1	300
H_I	1	70.0	59.7	5.0	280
	2	70.0	59.7	5.1	280
	3	70.0	59.5	5.2	285
AL	1	70.0	67.0	1.5	125

Where  $D_e$  is the external diameter,  $D_i$  is the internal diameter,  $t$  is the thickness and  $m$  is the weight of the items. All the measures were taken by using a 1/20 mm caliper by measuring the specimen in three different points and then averaging out. All the specimens measure 150 mm in length.

All the specimens tested are presented in Figure 2.12.



Figure 2.12: Tube specimens.

### 2.4.2. Tensile test specimens

The manufacturing process for the laminates shown in Figure 2.8 is the same as presented above. But in this case, a plain aluminum sheet is used as mold in order to maintain the laminate flat. After the autoclave process, the laminate sheet is cut into coupons with dimensions defined in Table 2.3.

As regulations suggest [78], on the coupon ends it is necessary to apply tab-end needed to transfer the load from the wedge grips of the tensile test machine to the specimen itself, thus reducing stress concentrations and protecting the specimen.

Therefore, GFRP tabs are applied with the same structural adhesive used in the lay-up lamination for the FML tubes. Another curing cycle in contemplation of gluing the components together is needed. The vacuum-bag for the curing of the resin is shown in Figure 2.13.

The specimens are identified as:

- TS the coupons for the shear plain tensile test, which are four items,
- T1 the coupons for the tensile test, which are five items.

In Table 2.6 are summed up all the specimen dimensions, where  $t$  is the thickness and  $w$  is the width of the elements. The measures are taken as the previous tube measurements.

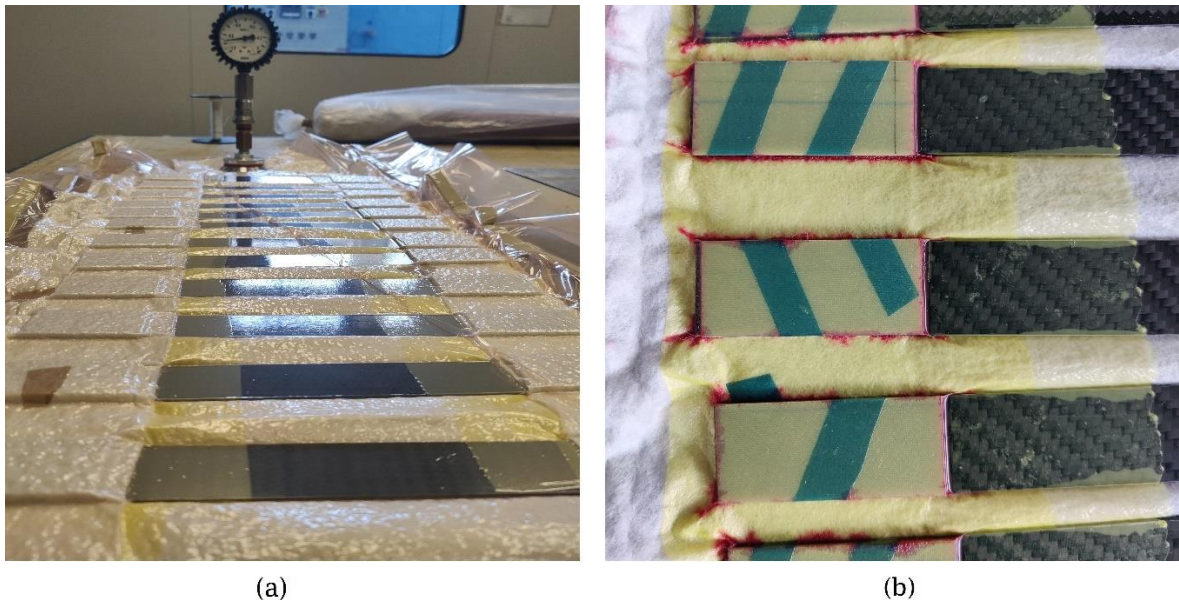


Figure 2.13: (a) Vacuum-bag coupons with tabs, (b) tabs close-up after curing cycle.

Table 2.6: Tensile and plain shear test specimen dimensions.

Specimen fiber orientation					
45°			0°		
Specimen ID	$t$ [mm]	$w$ [mm]	Specimen ID	$t$ [mm]	$w$ [mm]
TS1	2,55	24,72	T10	2,53	26,12
TS2	2,62	24,71	T11	2,65	23,25
TS3	2,75	24,74	T12	2,64	24,85
TS4	2,81	24,66	T13	2,58	24,65
			T14	2,72	24,65

In order to gain a better precision on the measure of the stress-strain relationship, some of the specimens are tested with dual grid biaxial strain gauge (KYOWA® KFGS-3-350-D16-11). The biaxial configuration is needed to compute the Poisson's ratio during the deformation. One last step before testing is to glue the sensors at the half length of the specimen, as shown in Figure 2.14.

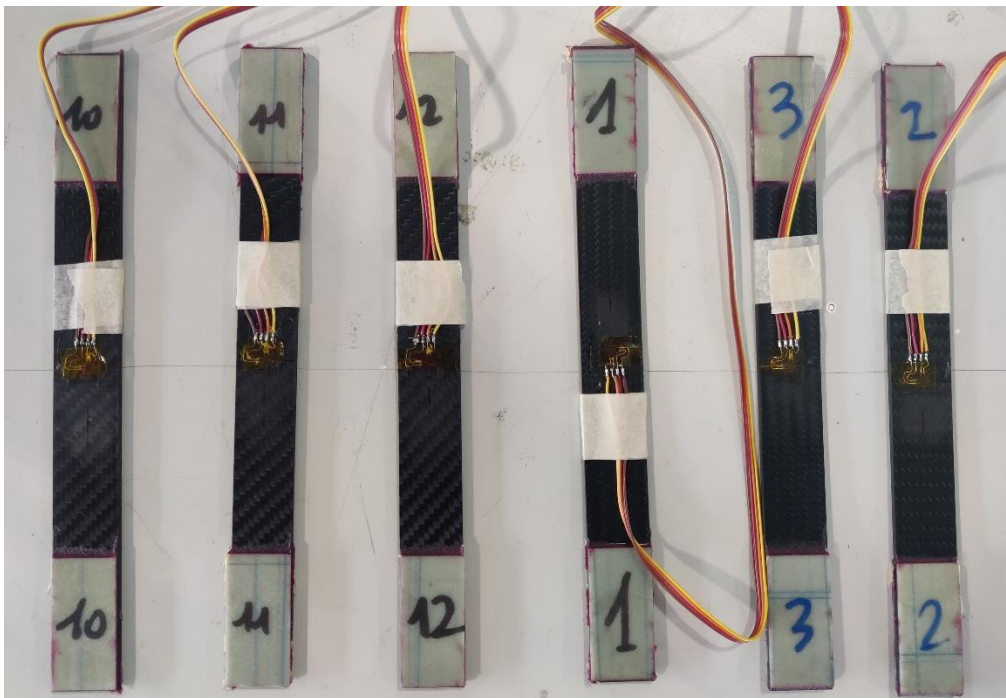


Figure 2.14: 0° and 45° fiber orientation specimens with strain gauge.

## 3 Experimental Testing

The following chapter is dedicated to the experimental part of the study. The activities are subdivided into two main groups: experimental characterization and crushing tests. The scope of the first group is to identify the material properties in terms of elastic constants and strength-related parameters, while the second group focuses on the study of the energy absorption properties of the built tubes.

### 3.1. Material characterization

For the analysis and design of a structure subjected to loading, in general, the experimental characterization of the material used must be done primarily. Material characterization refers to the determination of the material properties through tests conducted on suitably designed specimen. Understanding the material response over the entire range of loads is necessary if advanced design procedures are employed for efficient material utilization [27].

In this study, a simple characterization of the material to have a basic comprehension of material limit load behavior was performed, with the final aim of designing a numerical model to use. It is known that in order to perform a material characterization tensile and shear test are not completely sufficient. Still, since the thesis is a primitive approach to the FML argument, the material experimental characterization is approximative.

In this sub-chapter, stress-strain curves obtained from quasi-static tension tests are recovered. The parameters needed to define the elastic constitutive model, are extracted from stress-strain curves. Consider the orthotropic composite ply under in-plane stresses  $\sigma_1$ ,  $\sigma_2$ , and  $\tau_{12}$  in Figure 1.31(b).

Inherent to this study is an assumption of plane stress, where the out-of-plane stresses  $\sigma_3$ ,  $\tau_{23}$ , and  $\tau_{13}$  shown in Figure 1.31(a) are assumed to be small and neglected. Such an assumption is common both in structural analysis of composites and in basic testing, although the design of most structural configurations demands 3D analysis and a full set of orthotropic elastic constants.

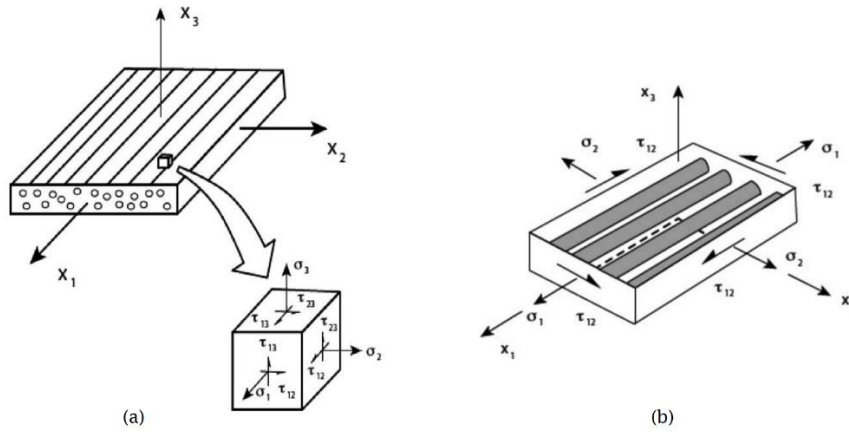


Figure 3.1: (a) Stress state on a material chunk, (b) stress state under in plane loading [79].

For a 2D plane stress state, the in-plane elastic constitutive relation between stresses and strain is:

$$\begin{bmatrix} \varepsilon_1 \\ \varepsilon_2 \\ \gamma_{12} \end{bmatrix} = \begin{bmatrix} 1/E_1 & -\nu_{12}/E_1 & 0 \\ -\nu_{21}/E_2 & 1/E_2 & 0 \\ 0 & 0 & 1/G_{12} \end{bmatrix} \begin{bmatrix} \sigma_1 \\ \sigma_2 \\ \tau_{12} \end{bmatrix} \quad (3.1)$$

where  $E_1$  and  $\nu_{12}$  are the elastic modulus and Poisson's ratio for loading along the  $x_1$  direction,  $E_2$  and  $\nu_{21}$  are the modulus and Poisson's ratio for loading along the  $x_2$  direction.  $G_{12}$  is the effective shear modulus of the composite in the  $x_1x_2$  plane.

Woven fabric composites loaded by the stresses  $\sigma_1$  and  $\sigma_2$  have similar response, therefore we can approximate the material property with  $E_1 \approx E_2$  and  $\nu_{12} \approx \nu_{21}$  [37].

### 3.1.1. Tensile Testing

Static tests were performed on MTS 810 Material Testing Systems. The machine has the capability of measuring applied load and crosshead displacement. Moreover, to the aforementioned biaxial strain gauges, a single-axis extensometer MTS 634.11F-54 is applied. Extensometers are less common in composite testings than strain gages. An extensometer is relatively expensive and may be damaged or destroyed upon failure of the test specimen which often tends to be violent because of the release of elastic strain energy upon failure. The test configuration is represented in Figure 3.2.

As stated earlier, the material characteristic of symmetric fabric laminate can be considered equal in the in-plane directions (Figure 1.31(b)). In addition, the limit load strengths can be approximately equal ( $X_1^T \cong X_2^T$  and  $X_1^C \cong X_2^C$ ), while the shear strength ( $X_S$ ) is quite small as it is governed by the matrix [79].  $X_1^T$  is the limit force



at which the laminate brakes under tensile loading in the  $x_1$  direction;  $X_1^C$  is the limit force at which the laminate brakes under compressive loading in the  $x_1$  direction.  $X_S$  is the in-plane limit shear load, which will be defined later.

Considering the latest assumption, the tensile tests are performed only for  $0^\circ$  fiber direction, assumed equal to the response in the  $90^\circ$  orientations.



Figure 3.2: Tensile system setup.

It is important to realize these definitions of stresses and strains in heterogeneous materials such as composites. Mechanical properties such as modulus ( $E$ ), Poisson's ratio ( $\nu$ ), and stress strength ( $\sigma^T$ ) are defined in terms of volume averaged stresses and strains, that is:

$$E_x = \frac{\sigma_x}{\varepsilon_x} \quad (3.2)$$

$$\nu_{xy} = -\frac{\varepsilon_y}{\varepsilon_x} \quad (3.3)$$

$$\sigma_x = \frac{P}{A} \quad (3.4)$$

The subscripts “ $x$ ” and “ $y$ ” refer to axial and transverse directions of a test specimen and  $P$  is the load in axial direction (applied by the test machine) and  $A$  is the cross-sectional area of the specimen (see Figure 3.3).

Under tensile load of as specimen the negative value ( $\varepsilon_y < 0$ ) is expected.

The load  $P$  is measured directly by the tensile testing system, axial and transverse strains are recorded by the gauges.

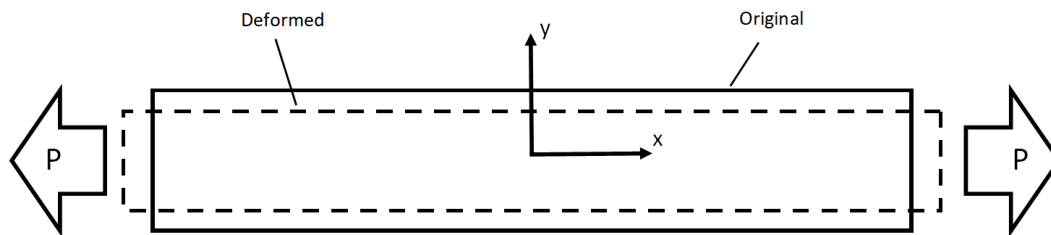


Figure 3.3: Schematic of tensile test specimen.

Standards suggest the computation of the chord modulus of elasticity to be computed in the initial elastic range between 1000÷3000 micro-strains in axial direction, so equation(3.1) is written as:

$$E_x = \frac{\Delta\sigma_x}{\Delta\varepsilon_x} \quad (3.5)$$

Where  $\Delta\sigma_x$  is the difference in applied tensile stress between the two strain points, and  $\Delta\varepsilon_x$  is equal to 2000 micro-strains [78].

Same consideration for equation(3.3), the Poisson's ratio becomes:

$$\nu_{xy} = -\frac{\Delta\varepsilon_y}{\Delta\varepsilon_x} \quad (3.6)$$

$\Delta\varepsilon_y$  is the difference in lateral strain between the two longitudinal strain points defined above.

In Figure 3.4 the strain-stress curves of the tensile test specimens are reported. The response between the coupons is similar in slope and limit load. It can be noticed that the transition region is not present in the material behavior.

The examination of the failure mode is the last important step of the experimental procedure. It is useful to understand mode and location of the failure in order to validate the test, since a specimen that breaks at some obvious flaw must be ignored. Three out of five specimens underwent a brittle failure inside the gage

section, while two of them failed at the interface of the tabs. All the failures are compliant with the rules (Figure A.2).

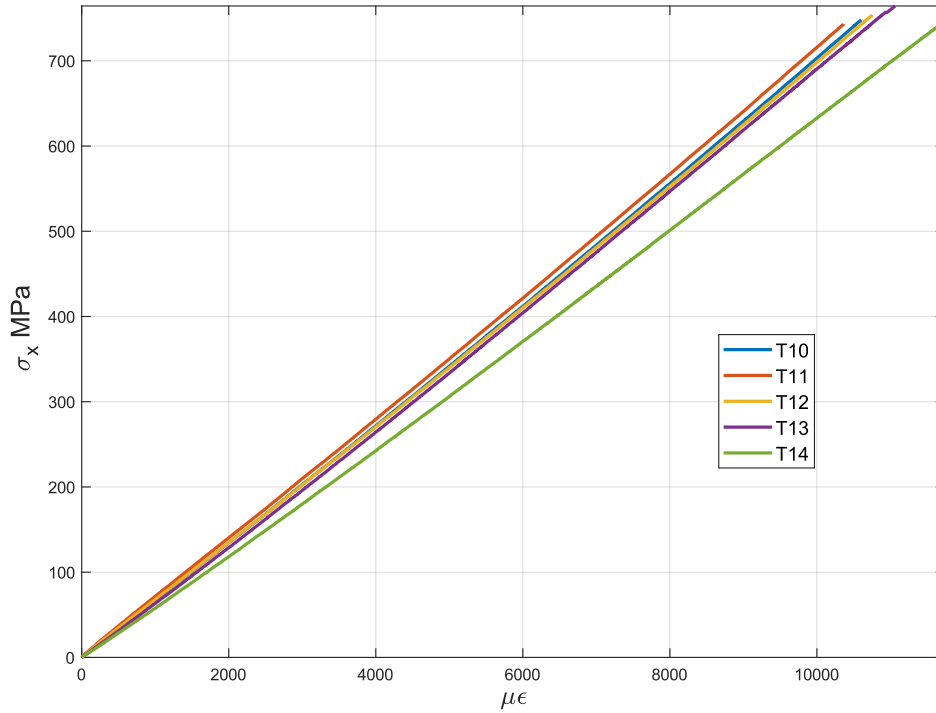


Figure 3.4: Tensile stress-strain for 0° orientation specimens.

The material properties obtained as results from tensile tests are presented in Table 3.1. At the end of the table are reported the average value, standard deviation and coefficient of variation based on the test population.

Table 3.1: Tensile test results

Specimen ID	$\sigma_x^T$ [MPa]	$\epsilon_x^T$	$\nu_{xy}$	$E_x$ [GPa]
T10	747.88	0.0106	0.0255	67.60
T11	743.01	0.0103	0.0447	69.03
T12	753.75	0.0107	0.0452	67.13
T13	764.32	0.0110	/	66.37
T14	746.54	0.0117	/	61.14
Average	751.16	0.0108	0.0385	66.30
SD <sup>1</sup>	8.273	0.040	0.112	3.02
CV%	1.10	3.78	29.08	4.55

<sup>1</sup> SD is the standard deviation and CV is the coefficient of variation.

$\sigma_x^T$  and  $\varepsilon_x^T$ , reported in Table 3.1, are the axial stress and strain at failure, respectively.

The mechanical properties of T13 and T14 coupons are obtained by the use of extensometer without strain gauges, therefore it is not possible to compute the Poisson's ratio.

### 3.1.2. In-plane shear

The in-plane shear response is determined via test method ASTM D3518. A 45° balanced and symmetric laminate tensile coupon shown in Figure 3.5 can be employed to determine the shear properties of the fabric ply in the principal material coordinate system, thus following the same procedure of test method D3039.

The state of stress in each lamina of the 45° laminate is not pure shear. Each lamina contains tensile normal stresses,  $\sigma_1$  and  $\sigma_2$ , in addition to the desired shear stress,  $\tau_{12}$  (Figure 3.5). Moreover, an interlaminar shear stress,  $\tau_{23}$  (Figure 3.1), is present near the laminate free edge [79]. Normally, this consideration could be neglected, and the stress state approximated, making the tensile shear test method an appropriate and a simple test for determining the shear modulus and strength of the ply.

Determination of the shear stress and strain in the principal planes ( $x_1, x_2$ ) of the 45° plies, Figure 3.5, is based on a stress analysis of the 45° specimen.

The in-plane shear stress  $\tau_{12}$  and shear strain are:

$$\tau_{12} = \frac{\sigma_x}{2} \quad (3.7)$$

$$\gamma_{12} = \varepsilon_x - \varepsilon_y \quad (3.8)$$

The axial stress  $\sigma_x$ , in equation (3.4), is computed by the use of equation (3.4).

The strain  $\varepsilon_x$  and  $\varepsilon_y$  in equation (3.8) are the measured values by means of a double grid strain gauge, as shown in Figure 2.14.

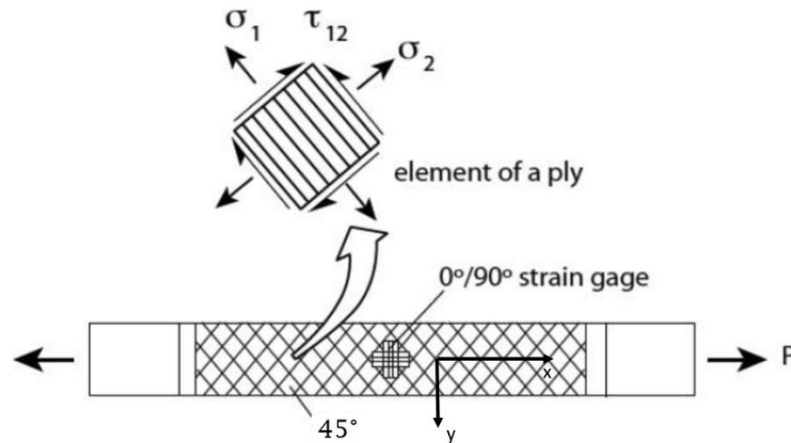


Figure 3.5: 45° tensile test specimen for measuring in-plane shear response [79].

The in-plane shear modulus,  $G_{12}$ , is readily determined by plotting  $\tau_{12}$  vs  $\gamma_{12}$  and establishing the slope of the initial portion of the curve. Regulation suggests  $G_{12}$  evaluation over a range of 2000÷6000 micro-strain in shear strain [80]. Hence, shear modulus is computed as:

$$G_{12} = \frac{\Delta\tau_{12}}{\Delta\gamma_{12}} \quad (3.9)$$

Here  $\Delta\tau_{12}$  is the difference in applied shear stress between the two shear strain points, and  $\Delta\gamma_{12}$  is the difference between the two shear strain points (nominally 0.004 strain).

If ultimate failure does not occur within 5 % shear strain, the data shall be truncated to the 5 % shear strain mark [80]. When the data is truncated, for the purpose of calculation and reporting, this 5% shear strain point shall be considered the maximum shear stress. The method is known for underestimating the ultimate shear stress not only due to large deformation effects (fibers rotation or scissoring), total thickness and free-edge effect.

The following presents the shear stress-strain relationship of the 45° coupons in Figure 3.6, and the mechanical properties in Table 3.2.

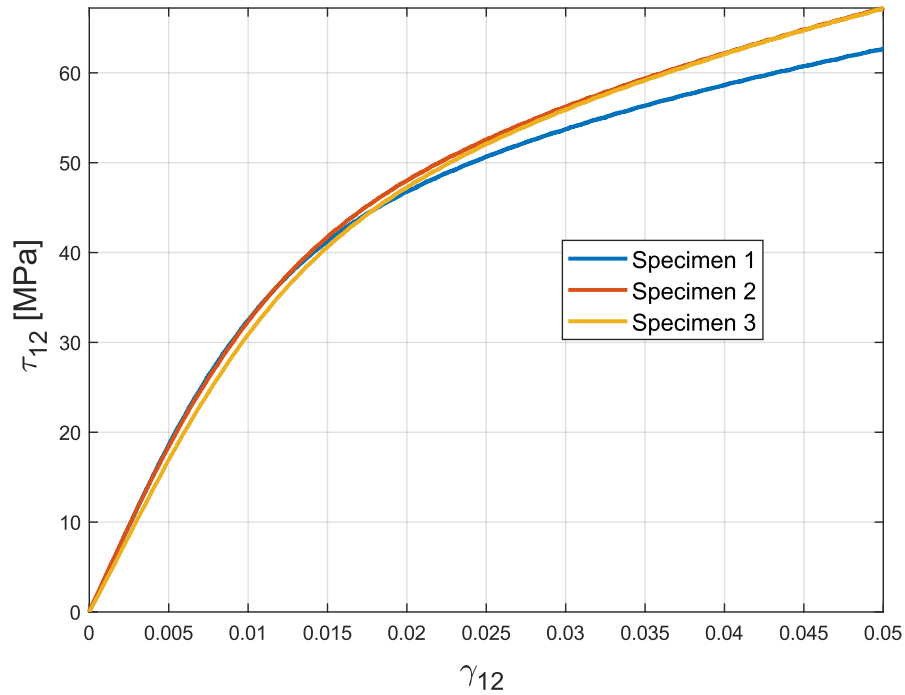


Figure 3.6: In-plane shear stress-strain relationship.

Table 3.2: In-plane shear test results

Specimen ID	$G_{12}$ [Mpa]	$\tau_{12}^{5\%max}$ [Mpa]
TS1	2818	62.65
TS2	2822	67.21
TS3	2638	67.12
Average	2758	65.66
STD	104.4	2.6
CV %	3.78	3.96

Only three out of four specimens are reported in Table 3.2. The fourth in-plane shear coupon is tested without strain gauges and shear strain is impossible to compute. The last specimen gives the same results in a matter of failure mode and ultimate axial load  $\sigma_x$  and strain  $\epsilon_x$  (measured by extensometer).

All the specimens fail in the same brittle  $45^\circ$  failure, typical of the test for fabric laminate (as shown in Figure A.3).

## 3.2. Drop tower testing

The most common method for testing energy absorption is by conducting impact tests. Drop towers have been developed for reliable, repeatable impact tests. There are several drop towers commercially available, however, these models are very expensive and in many cases are unsuitable for aerospace material experiments based upon their range of drop energy.

Test device consists of a mass with a chosen weight raised at a certain height to transform potential energy in kinetic and to reach the required velocity at impact. The LaST drop test system is a double rail mass with a maximum height of 5 meters and a mass range to 500kg.

In order to measure the crushing load, two accelerometers (for redundancy purpose) are placed on the impacting mass to capture solicitations during the impact. The signal is directly recorded by the acquisition system with a frequency of 12.5 KHz. The drop tests are recorded using a Phantom VEO® high speed camera 60000fps to capture the crushing dynamic behavior of specimens during tests and better comprehend sensors data.

In order to constrain the specimens at the base plate, plugs were produced that constrain inside the tubes, see Figure 3.7(a). Holes inside the plugs are drilled in order to permit air and debris to be expelled during the crushing of CFRP material.



(a)



(b)

Figure 3.7: (a) Specimen ready to be tested, (b) test system.

Two square aluminum tubes are placed next to the specimen during the impact test that act as shock absorber, to avoid hard impact in case of catastrophic failure that could damage the test system, as shown in Figure 3.7(a).

The length of the shock absorber is such that each of the tubes crushing displacement is maximum 100 mm (Figure 3.7(a)).

After the dynamic tests, the variations in force over displacement are analyzed for each specimen through proper signal filtering to eliminate high frequency contents introduced by vibration and noise of the test system. Standards SAE J211(Society of Automotive Engineers) suggests the use of CFC (Channel Frequency Class) filtering type, which is based on a Butterworth 4-pole phase-less digital filter [81]. In this study, filtering type CFC180 was utilized for acceleration acquisition analysis, because the channel class is a standard recommendation for acceleration filtering.

To compute the SEA value after the test, equation(1.4) is rewritten as:

$$SEA = \frac{EA(\delta)}{\rho_{material} * V(\delta)} \quad (3.10)$$

Where  $V(\delta)$  is the volume of the damaged material function of the stroke  $\delta$ , in our case it corresponds to the volume of the tubes, computed using data of Table 2.5. In equation (3.10),  $\rho_{material}$  is the material density which value is computed for aluminum, composite and hybrid materials by simply dividing the tube mass by the volume of each 150mm length specimens. Their values are reported in Table 3.3.

Table 3.3: Effective material density

$\rho_{AL} [kg/m^3]$	$\rho_{CFRP} [kg/m^3]$	$\rho_{Hybrid} [kg/m^3]$
2.581	1.401	1.762

The impacting mass of 350 kg remains the same during the tests, the velocity is different for each material type, and its value is defined by the expected energy absorption capacity considering other SEA values found in literature [11], [75]. The energy is transformed in impacting velocity (kinetic energy), therefore, it is transformed in height ( $h$ ) from which the impacting mass is dropped off (potential energy). For large composite tubes and hybrid tubes, the dropping height is increased for different tests of the same type, because the impacting mass does not reach the shock absorber.



The hypothetical velocity computed from the potential energy is defined as  $V_{teo}$ . Moreover, the velocity at the impact is computed by integrating the sampled acceleration over time and is defined as  $V_{impact}$ .

If the crushing platform touches the shock absorber, the stroke is stopped at 100mm, else the stroke is computed by frame analysis of the high-rate video recorded. This post-tests measurement is processed using video analysis software Phantom Camera Control®.

### 3.2.1. Aluminum tube

The impacting velocity for AL tube test is 4.2 m/s, dropping the mass from 0.9 m.

For the dynamic loading, it is noted that the aluminum tube translates part of impact kinetic energy into strain energy, and the impactor continues to drop onto the stop blocks. The crushing process of the aluminum column initiates at the top end and deforms plastically with an axisymmetric mode in the early stage of the crushing process. With increasing crushing process, the deformation evolves into a non-axisymmetric pattern Figure 3.8.



Figure 3.8: AL tube crushing dynamic.

In Figure 3.9 is reported the crushing load over the impacting plate displacement during the crushing. The negative value after 10mm is an error of measurement that filtering could not eliminate.

The peaks load before 40 mm are sharper and correspond to the buckling loads which cause a change in geometry during the ring collapsing mode. After 40 mm of stroke there are more flat and large bumps in loading, this is caused by the collapsing mode switching from concertina to non-axisymmetric mode.

In Table 3.4 are reported the crashworthiness parameters obtained in post-processing.

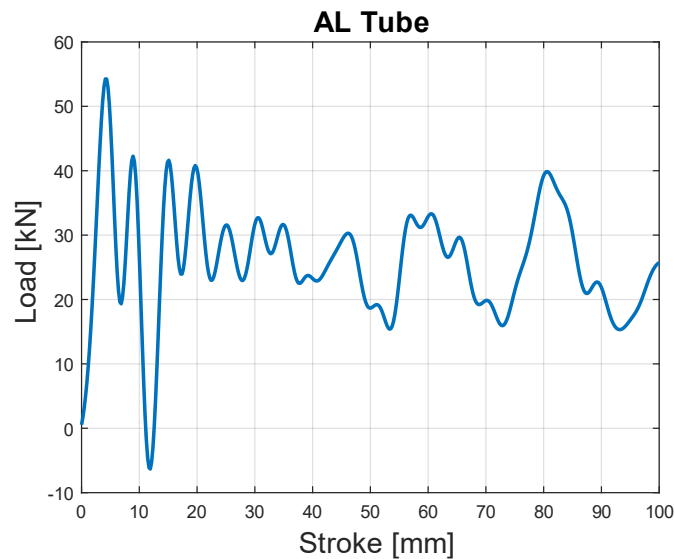


Figure 3.9: AL tube crushing load during the stroke.

Table 3.4: AL tube crushing data.

$MF$	$IPCF$	$EA$	$\delta$	$SEA$	$V_{impact}$	$h$	$V_{teo}$
$kN$	$kN$	$J$	$mm$	$J/g$	$m/s$	$m$	$m/s$
25.9	54.2	2599	100	31.2	4.1	0.90	4.2

## 3.2.2. Composite tubes

### 3.2.2.1. Internal lamination bare composite tubes

The composite test are divided into two groups, the C\_S and C\_L tubes, starting with the small diameter tubes the impacting velocity expected is 5.6 m/s dropping the impacting plate from 1.60 m of height. All the three tubes reach the shock absorber, therefore the dropping height is not increased.

The brittle fragmentation failure is the same in all the C\_S tube tests, with the only difference in C\_S\_3 specimen which initiate the crushing front from the bottom and not from the top as the other specimens, see Figure 3.10: (a) C\_S\_1 and (b) C\_S\_3 specimens.

Load-displacement curves of the small carbon fiber tubes are reported in Figure 3.12.

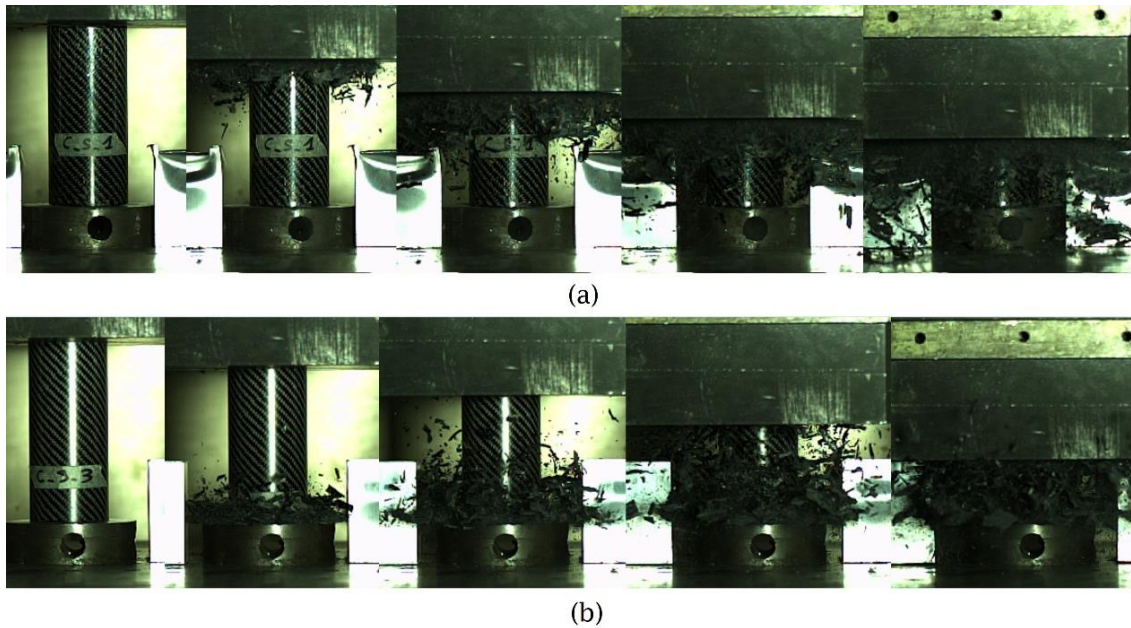


Figure 3.10: (a) C\_S\_1 and (b) C\_S\_3 specimens.

Less oscillations and higher loads can be noticed in respect to the ductile specimen, as expected from notions ( see Figure 3.12) . The right-end of the curve for C\_S\_3 is different in respect to the other two specimens, and the reason is that due to the fragmentation mode from the bottom and the design of the tube-plug (Figure A.4), all the debris are not trapped inside the tube during the crushing. On the contrary, when the crushing front starts at the top end of the specimen, the debris are captured inside the tube which create and higher load response due to compaction of material inside the specimen during the phenomena, see Figure 3.11.

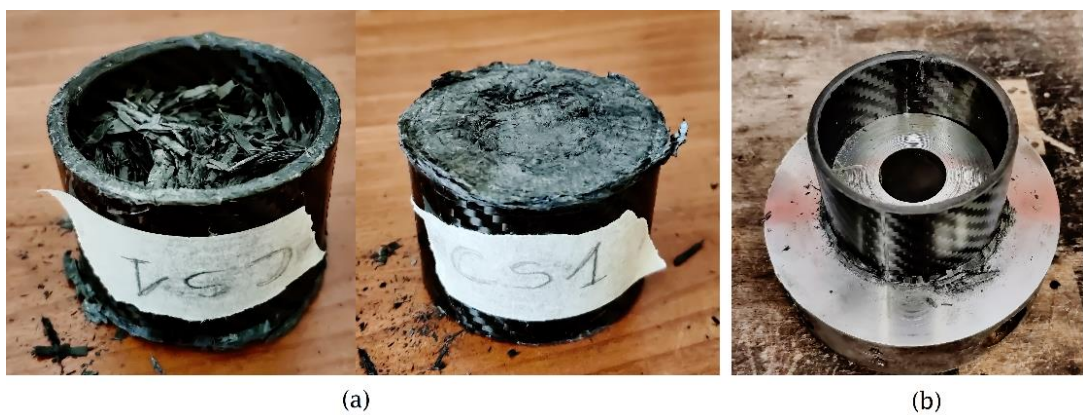


Figure 3.11:(a) full of debris C\_S\_1 and (b) empty C\_S\_3 specimens.

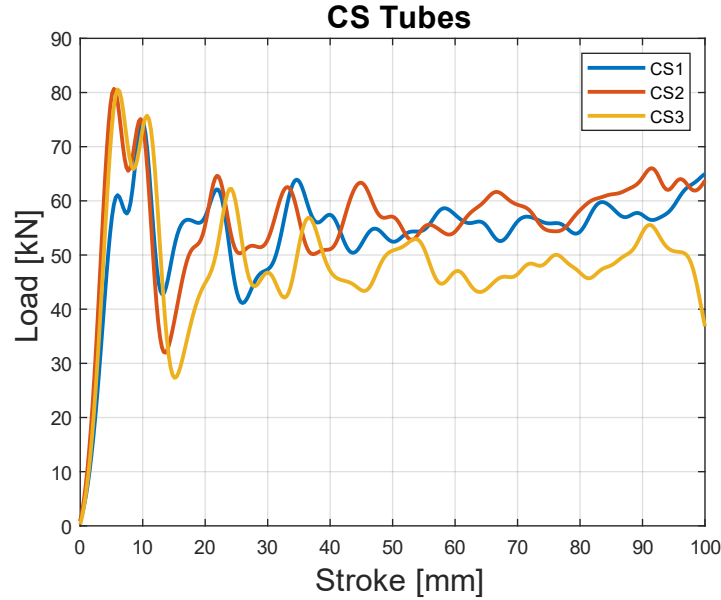


Figure 3.12: Internal lamination bare composite tubes

In Table 3.5 are reported the crashworthiness parameters obtained in post-processing. It must be noticed that SEA of C\_S\_1 specimen is almost the same value as C\_S\_3, despite the evident difference in Figure 3.12. This depends on the geometry measurements (Table 2.5) that define the volume  $V(\delta)$  of  $Weight_{damage\ material}$  (equation (1.4)).

Table 3.5: Internal lamination bare composite tubes crushing data

	$MF$ $kN$	$IPCF$ $kN$	$EA$ $J$	$\delta$ $mm$	$SEA$ $J/g$	$V_{impact}$ $m/s$	$h$ $m$	$V_{teo}$ $m/s$
C_S_1	54.2	74.6	5428	100	50.7	5.4	1.6	5.6
C_S_2	56.4	80.7	5646	100	57.8	5.5	1.6	5.6
C_S_3	48.4	80.6	4845	100	50.3	5.4	1.6	5.6

### 3.2.2.2. External lamination bare composite tubes

Testing the C\_L tubes the impact velocity is the same as before (5.6 m/s), but for the first test (C\_L\_1) the impacting plate does not reach the shock absorber, which can be seen in the last frame of Figure 3.13(a). Therefore, it was chosen to increase the velocity to 6.0 m/s to exploit all the available tube length. In the last frame of Figure 3.13(b) The crushing mass touching the left shock absorber can be seen.

Large CFRP tubes during the crash have the same brittle fracturing failure mode as the previous small ones.

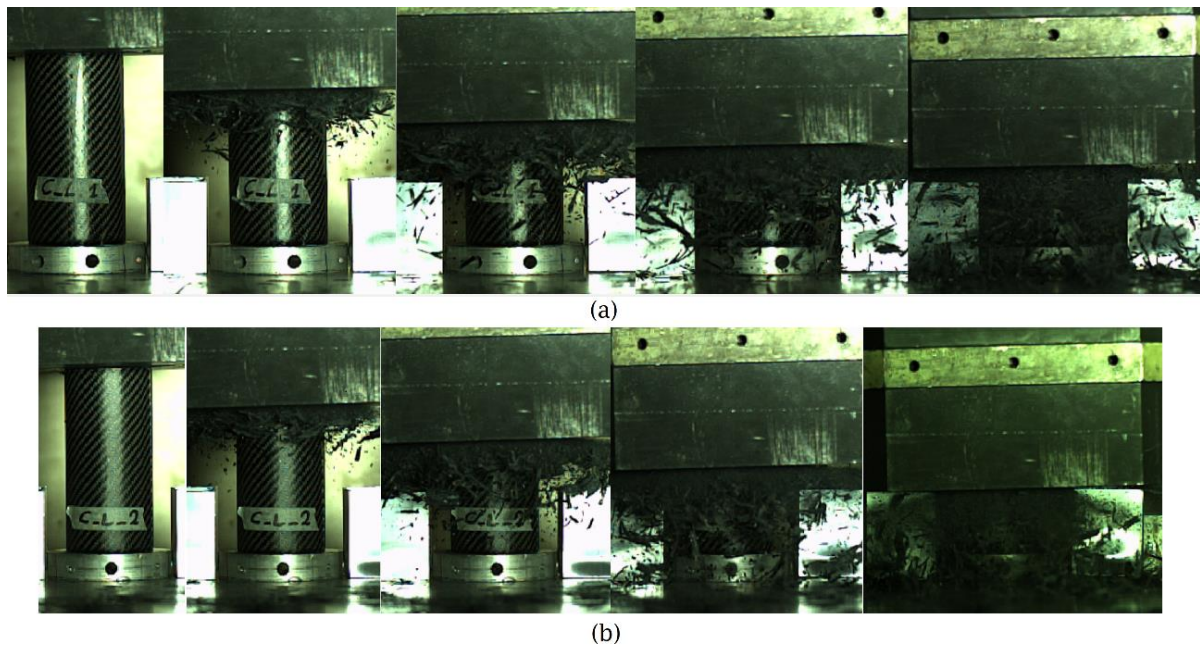


Figure 3.13: (a) C\_L\_1, (b) C\_L\_2 crushing dynamic.

In Figure 3.14 the CFRP tubes after the impact are shown. It can be notice that the splaying mode is more evident in these specimens, respect to Figure 3.11., because the circumferential plateau caused by the wedge ( Figure 1.21) is more evident.



Figure 3.14: Post-crush (a) C\_L\_1 and (b) C\_L\_2 specimens.

Moreover, in Figure 3.14(a) a minor compaction of debris inside the tube is noticeable, due to a reduced stroke. In addition, a large bent lamina bundle that did not break during the test. The composite “petal” is accountable to the lamination overlapping point, which creates higher stiffness and higher structural integrity during the crash that did not permit the completely detachment.

In Figure 3.15 are reported the load over displacement of large composite tubes, the curves are similar to each other, with higher initial peak for C\_L\_2 test because the impact velocity is higher respect to C\_L\_1. The trend is similar to C\_S tubes, with a relatively constant load after the initial peak load. The test for C\_L\_2 actually does not reach a stroke of 100mm due to the fact that the impacting mass is tilted on the left and touches the shock absorber too early, This can be seen in Figure 3.13(b). In addition, the right leg of the curve of the C\_L\_1 test has a little load increment with the stroke, and the reason could be the following:

- The higher impact velocity of C\_L\_2 test ignites a crushing mode that absorbs less energy respect lower velocity,
- C\_L\_2 specimen splaying mode is not symmetrical but tends to expel more debris on the outside, postponing the compaction of material (note, specimen in Figure 3.14(b) is subjected to a stroke length higher than 100mm).

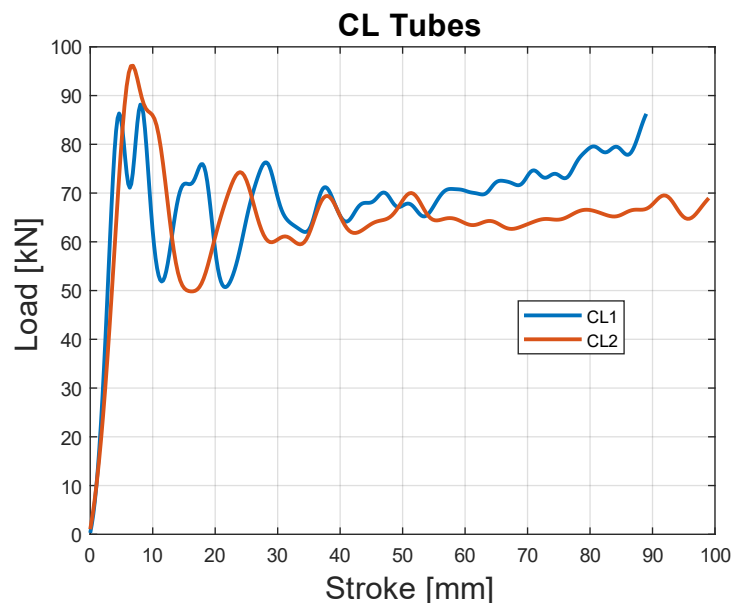


Figure 3.15: Load-displacement of external lamination bare composite tubes

In Table 3.6 are reported the results of the crushing test. Values in terms of mean load and specific energy are similar and the peak force for higher impacting velocity is higher es expected. The energy absorbed is not exactly equal to the potential energy, despite reaching null velocity before the shock absorber, because some impact energy is transformed into other forms of energy (kinetic energy of debris and heat). In terms of SEA, C\_L\_1 performs similar to C\_L\_2 in spite of higher mean load. This is because of higher stroke length in the second test.

Table 3.6: External lamination bare composite tubes crushing data.

	$MF$ $kN$	$IPCF$ $kN$	$EA$ $J$	$\delta$ $mm$	$SEA$ $J/g$	$V_{impact}$ $m/s$	$h$ $m$	$V_{teo}$ $m/s$	$Eng_{teo}$ $J$
C_L_1	63.08	88.15	5437	89	56.58	5.5	1.60	5.6	5493
C_L_2	61.28	96.12	6003	99	54.78	5.9	1.85	6.0	6351

### 3.2.3. External lamination hybrid tubes

A total energy absorption is expected, in respect to the previous test. Consequently, the dropping height is increased to 2.0 m and it increased during the tests since the shock absorber are not hit.

Figure 3.16 shows the behavior of external laminated aluminum tubes during the crushing test. The external fronds, which are (especially for specimen H\_E\_3 and H\_E\_2) typical of the splaying fracturing mode eventually detach after few centimeters, thus generating bigger debris in respect to bare composite tubes, can be noticed. During the interaction with the impacting mass, the large debris are probably generated because of the expulsion of material only outside of the tube, because of the internal ductile tube that blocks the composite debris. The behavior of H\_E\_3 and H\_E\_1 specimen differ due to the delamination between composite laminate and aluminum, and complete detachment during the crash, see Figure 3.17(a), (c).

In Figure 3.16(c) a crack propagating in longitudinal direction from the top end (start of the crushing front) is evident. This eventually reaches the bottom and lets the composite chunk of material to completely detach itself during the crushing phenomena.

The break of external lamination of specimen H\_E\_3 is not evident in Figure 3.17(a) because the broken half happened on the back of the specimen.

By analyzing the videos of the impact, the moment the composite broke can be captured, due to a sudden small change of shape of the tube. The breakage in pieces of the external lamination is caused by the deformation of internal ductile tube.

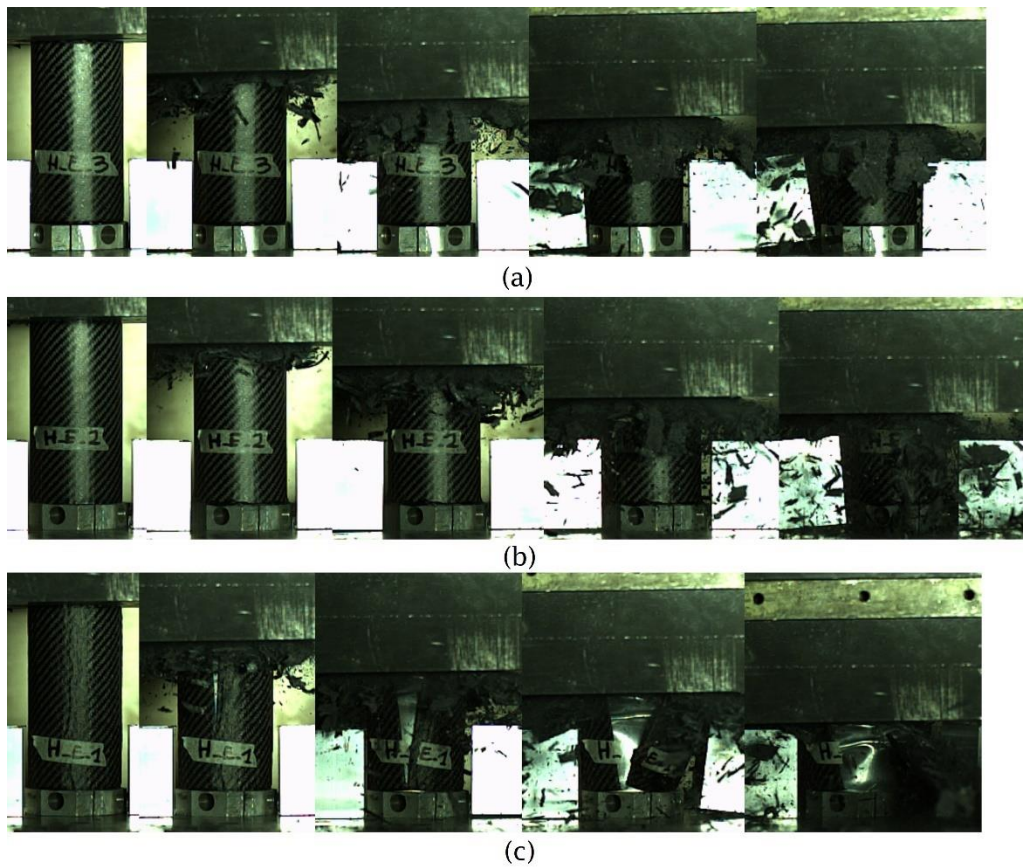


Figure 3.16: Crushing dynamic of (a) H\_E\_3, (b) H\_E\_2, (c) H\_E\_1.

Despite an initial inward deformation mode mixed with a splaying-delamination mode (evident from the black stripes marks on the inside of post-crash hybrid tube Figure 3.16), the stress in the aluminum tube causes a crack propagation, delamination and detachment. Then the aluminum tube starts folding with a diamond mode Figure 3.17(a), (c).

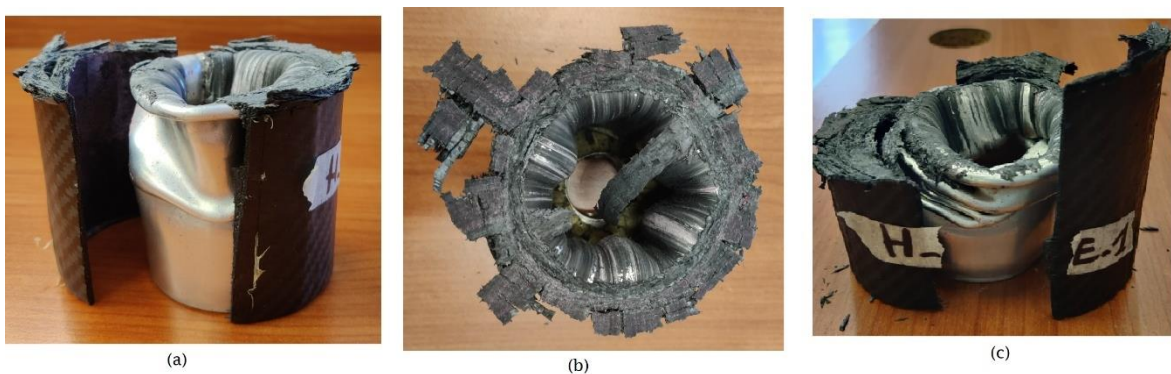


Figure 3.17: Post-crush specimens (a) H\_E\_3, (b) H\_E\_2, (c) H\_E\_1.

It must be noticed that, despite the delamination of H\_E\_3 specimen, the detached material still collaborates during the crushing. The latest assumption is made



considering the detached half of H\_E\_3 specimen, it has the same longitudinal length of the front material that remains glued to the internal tube. On the contrary for specimen H\_E\_1 which is broken in three parts, the front-side chunk of material that detaches during the crushing does no longer participate in the energy absorption. This is evident by the length of the remaining materials, the other two pieces of the external lamination interact with the impacting mass till the end, see Figure 3.17(c).

In Figure 3.18, the reacting forces during the crushing mass displacement are reported. The graph legend is reported with the dropping height associated to each specimen. It is evident that the loads are greater in respect to bare material tubes. As the impact velocity increases, the initial peak load increases as well. For both H\_E\_1 and H\_E\_3 tests, the curve tends to decrease after 60 mm of stroke due to the damage of the composite lamination. More peaks due to the folding of AL tube can also be noticed.

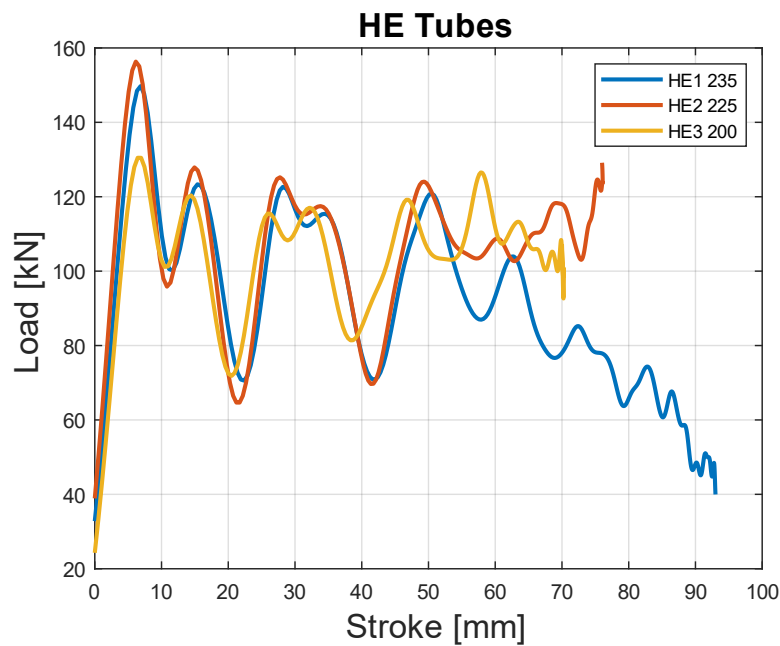


Figure 3.18: Load-displacement of external lamination hybrid tubes.

Table 3.7: External lamination hybrid tubes crushing data.

	$MF$ $kN$	$IPCF$ $kN$	$EA$ $J$	$\delta$ $mm$	$SEA$ $J/g$	$V_{impact}$ $m/s$	$h$ $m$	$V_{teo}$ $m/s$	$Eng_{teo}$ $J$
H_E_3	91.87	129.59	6391	70	50,69	6.0	2.0	6.2	6867
H_E_2	99.96	155.58	7382	76	52.97	6.4	2.25	6.6	7725
H_E_1	70.64	149.21	7783	93	45.33	6.6	2.35	6.8	8068

Table 3.7 reports the defining parameters of crushing test. It is evident how the catastrophic collapse of specimen H\_E\_1 results in lower specific energy index in respect to the other tubes. On the other hand, despite delamination of H\_E\_3, the SEA value is similar to the second test which performs better. This is because the delamination takes place almost at the stroke end.

#### 3.2.4. Internal lamination hybrid tubes

The impacting velocity starts from 6.8 m/s and is increased during the tests to exploit the entire length of the FML tube. Figure 3.19 shows the crushing dynamic of the internal laminated hybrid tubes. The external folding mode of the AL tube in all the tests is evident as well as the small quantities of debris escaping outside the ductile tube.

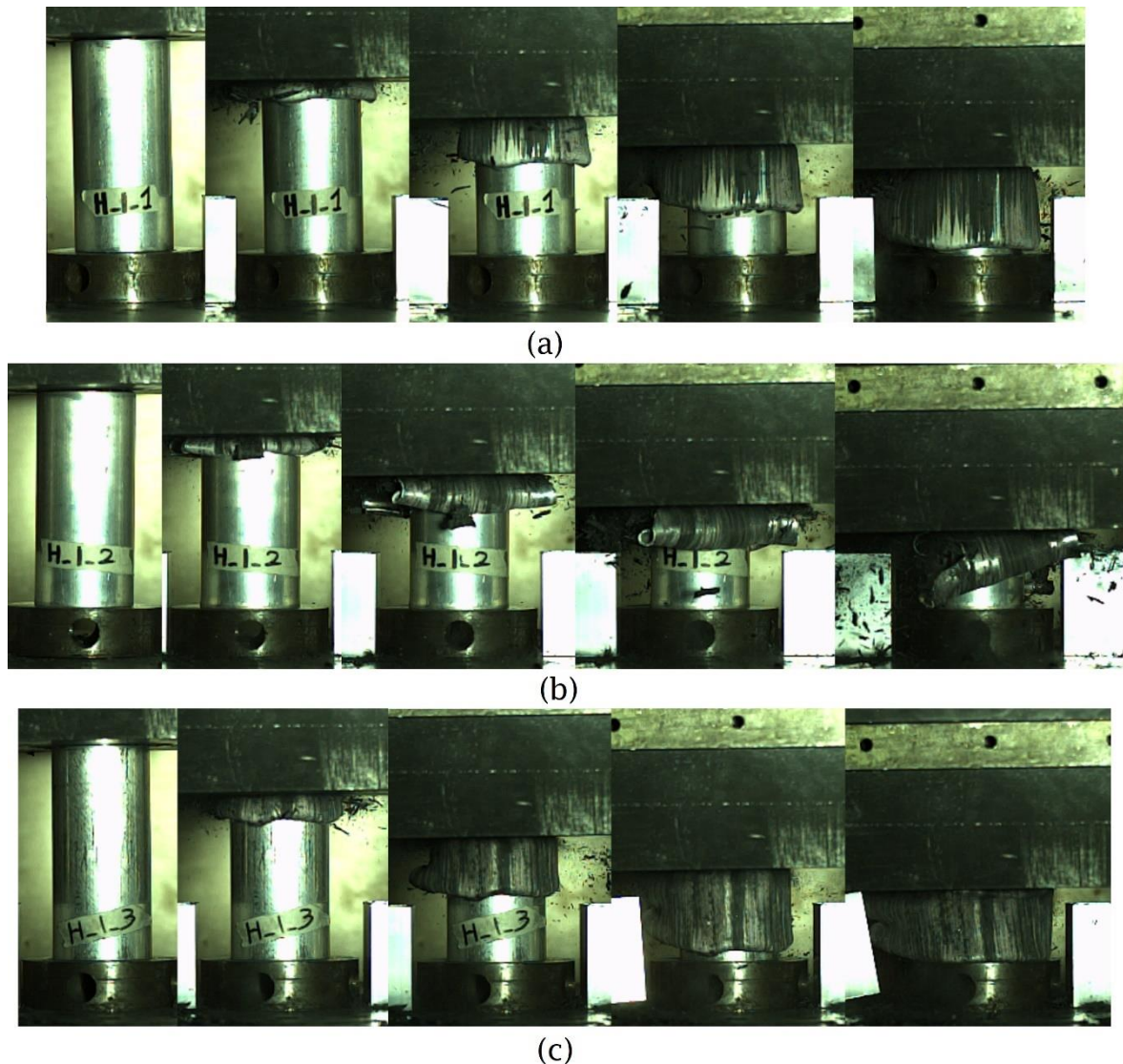


Figure 3.19: Crushing dynamic of (a) H\_I\_1, (b) H\_I\_2, (c) H\_I\_3.

The outside folding of the aluminum is different to the “mushroom” deformation mode, typical of high velocity impact of ductile tube (Figure 1.6). The deformed aluminum top end travels to the bottom end with the same velocity of the impacting mass instead of pointing outward, while on the back of tube a crack propagates opening the ductile sheet. See Figure 3.20. The outward folding mode is considered a progressive crushing mode [77].

It must be noticed, in Figure 3.19 and in high frame videos of the test is evident composite debris dust expelled from the plug holes at the base of the tubes. Therefore, air pressure is reduced, and small debris are expelled during the crushing.



Figure 3.20: Post-crush H\_I\_1 specimen.

FML tube H\_I\_2 exhibit a completely different mode in respect to the other specimens (Figure 3.19). Figure 3.21 shows the specimen after the impact. The four petals created during the impact are evident. In the same picture, a bigger area of debris on the top end is evident.



Figure 3.21: Post-crush H\_I\_2 specimen.

In Figure 3.23 The reacting forces during the crushing mass displacement are reported. The graph legend is reported with the dropping height associated to each specimen. The curves of the three specimens have similar trends while increasing the velocity, even for the different deformation mode of H\_I\_2 which shows a lower initial peak load despite higher velocity in respect to H\_I\_1. Furthermore, it can be stated that the deformation mode of specimen H\_I\_2 is not catastrophic because of the steadiness of the load curve during the stroke.

In addition, the different crushing mode postpones the compaction of the inside composite debris because more material can escape from the top end during the impact. All the specimens exhibit a steep trend in the right-leg of the curve, which is caused by the compaction of the internal composite debris.

Specimen H\_I\_3 exhibits higher reaction forces at the end of the stroke because, in addition to the compaction of debris, the external folding mode that reaches the bottom end is compacted (Figure 3.19(c)) and becomes, once again, a structure which deformation opposes to the impacting mass.

In Figure 3.22 the deformed external ductile frond by a compression load is evident, which differs from specimen H\_I\_1 in Figure 3.20 (because in the external folding does not touch the bottom plate).



Figure 3.22: Post-crush H\_I\_3 specimen<sup>2</sup>.

---

<sup>2</sup> The inside of the tube is empty because the photo was taken after debris removal.

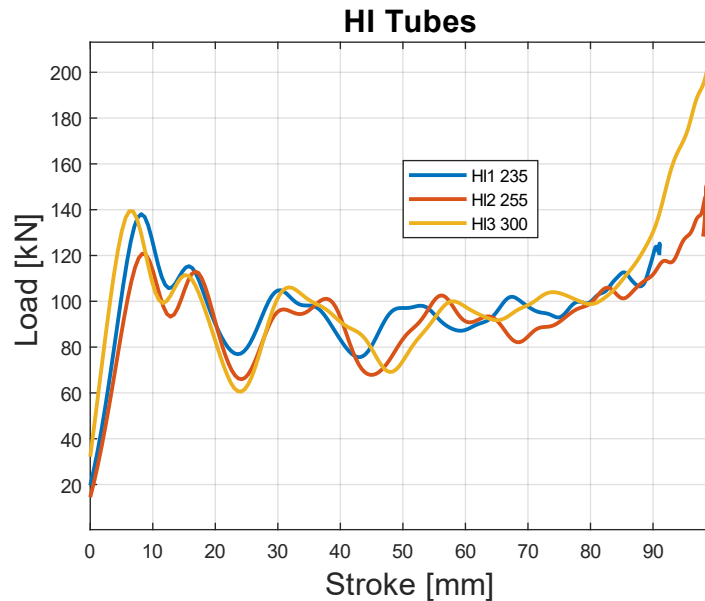


Figure 3.23: Load-displacement of internal lamination hybrid tubes.

In Table 3.8 the crashworthiness parameters of internal lamination FML tubes are reported. The IPCF (initial peak forces) are also reported, but they do not correspond to the maximum force generated during the impact, because for H\_I\_2 and H\_I\_3, the maximum load during the impact happens at the end of the stroke, respectively 150.64 kN and 210.77 kN. As previously mentioned, the increment is caused by the compaction of the composite debris inside the AL tube.

Table 3.8: Internal lamination hybrid tubes result data.

	$MF$ $kN$	$IPCF$ $kN$	$EA$ $J$	$\delta$ $mm$	$SEA$ $J/g$	$V_{impact}$ $m/s$	$h$ $m$	$V_{teo}$ $m/s$	$Eng_{teo}$ $J$
H_I_1	90.46	137.86	7835	91	52.00	6.6	2350	6.8	8068
H_I_2	95.89	120.80	8357	98	50.48	6.8	2550	7.1	8755
H_I_3	109.46	139.38	9781	100	55.23	7.4	3000	7.7	10300

### 3.3. Comparative analysis

Table 3.9 reports all the results from the tests. The higher loads involved in hybrid tests are evident, due to the higher thickness of the tubes, therefore more mass is involved. It is evident that the specific energy of hybrid tube is close to the composite tube value, except for specimen H\_E\_1, which is subjected to a catastrophic failure. The absorbed energy of C\_L is higher in respect to C\_S specimen tests because more material is involved during the crush. The large

tubes perform slightly better than the small bare composite tubes in terms of SEA and MF (mean force) values.

Checking the Crushing Force Efficiency (CFE) of all the specimens, for FML tubes values are close or even better in respect to bare composite specimens. This means that they have almost the same efficiency in terms of replicating an ideal energy absorber structure (Figure 1.1).

Table 3.9: Results of the specimen tested.

	<i>MF</i> <i>kN</i>	<i>IPCF</i> <i>kN</i>	<i>EA</i> <i>J</i>	$\delta$ <i>mm</i>	<i>SEA</i> <i>J/g</i>	<i>CFE</i>	$V_{impact}$ <i>m/s</i>
AL	26.38	54.26	2662	100	31,95	0.49	4.1
C_S_1	52.48	74.57	5166	100	50,94	0.70	5.5
C_S_2	54.58	80.68	5365	100	57,97	0.68	5.9
C_S_3	48.30	80.56	4877	100	52,54	0.60	5.4
C_L_1	63.08	88.15	5437	89	56,58	0.72	5.5
C_L_2	61.28	96.12	6003	99	54,78	0.64	5.9
H_E_3	91.87	129.59	6391	70	50,69	0.71	6.0
H_E_2	99.96	155.58	7382	76	52.97	0.64	6.5
H_E_1	70.64	149.21	7783	93	45.33	0.47	6.6
H_I_1	90.46	137.86	7835	91	52.00	0.66	6.6
H_I_2	95.89	120.80	8357	98	50.48	0.79	6.8
H_I_3	109.46	139.38	9781	100	55.23	0.78	7.4

Comparing the best performance of energy absorption, it can be stated that H\_I specimen performs better than H\_E tubes, if compared with the bare composite components:

- The difference in terms of SEA between the best internal laminated tubes, H\_I\_3 and C\_S\_2 is 5.7%.
- The difference in terms of SEA between the best external laminated tubes, H\_E\_2 and C\_L\_1 is 7.7%.

Obviously, the peak load values are functions of filtering, meaning that by changing the class of filter is going to modify the CFE values. Moreover, for H\_I\_2 and H\_I\_3 specimens, their CFE value is drastically reduced if the maximum loads at the end of curve are considered, respectively 0.63 and 0.52. Considering all the trials, the best SEA is obtained with bare composite tube C\_S\_2, between the FML tubes. The best configuration is the internal lamination with test H\_I\_3 because of the increasing load trend, thanks to compaction of CFRP debris inside the tube.

The stroke of the tests is influenced by the impact velocity. Consequently, energy absorbed values are not comparable. In order to compare the crushing performance of the specimens, all the force-displacement curves are truncated at 70 mm of stroke, the minimum stroke recorded. In Figure 3.24, the crushing load curves of the specimen tested are reported. Noted as both H\_E and C\_L specimens, they have higher loads because of more mass interaction during the crash.

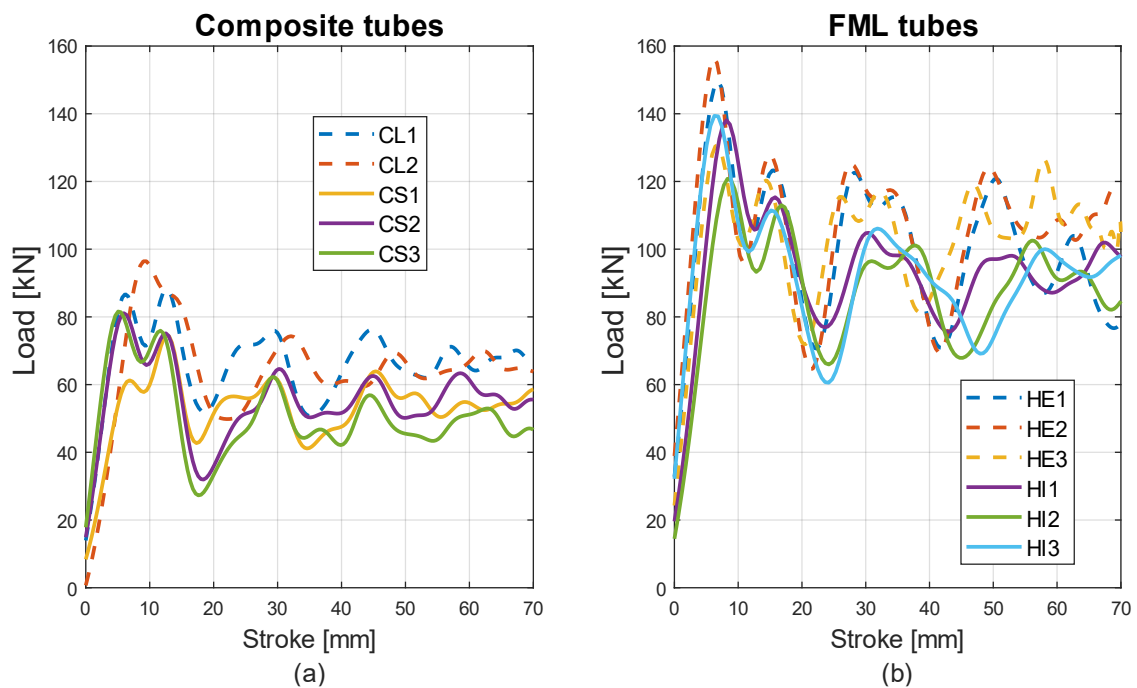


Figure 3.24: Load-displacement curves of (a) bare composite and (b) hybrid tubes

In the initial part of the stroke (0-30 mm) the curves of both H\_I and H\_E have similar trends and peaks similar to the bare composite tube, which means the composite crushing behavior dominates the initial part of the hybrid crushed tubes. Stroke efficiency index is not reported because the impact velocity varies in the tests with the aim of using all the length available.

Figure 3.25 reports the trend of comparable hybrid tube with the bare material specimen and the summation of the latest. Figure 3.25(a) presents the tubes performed with internal lamination method (H\_I and C\_S). Considering the curve of the sum of loads of bare material with the internal laminated FML, it can be stated that H\_I configuration does not increase the initial peak load because its value is similar to the sum. Moreover, the load reduction after the initial peak is reduced in the hybrid tube and the load curve is generally above the curve of the sum, meaning a better performance of the FML tube.

In Figure 3.25(b) The tubes performed with external lamination method (H\_E and C\_L) are reported. Also in this case, the post-peak trend of the hybrid tube performs better than the summation of the bare material tubes. The initial peak of H\_E tube is higher than the sum.

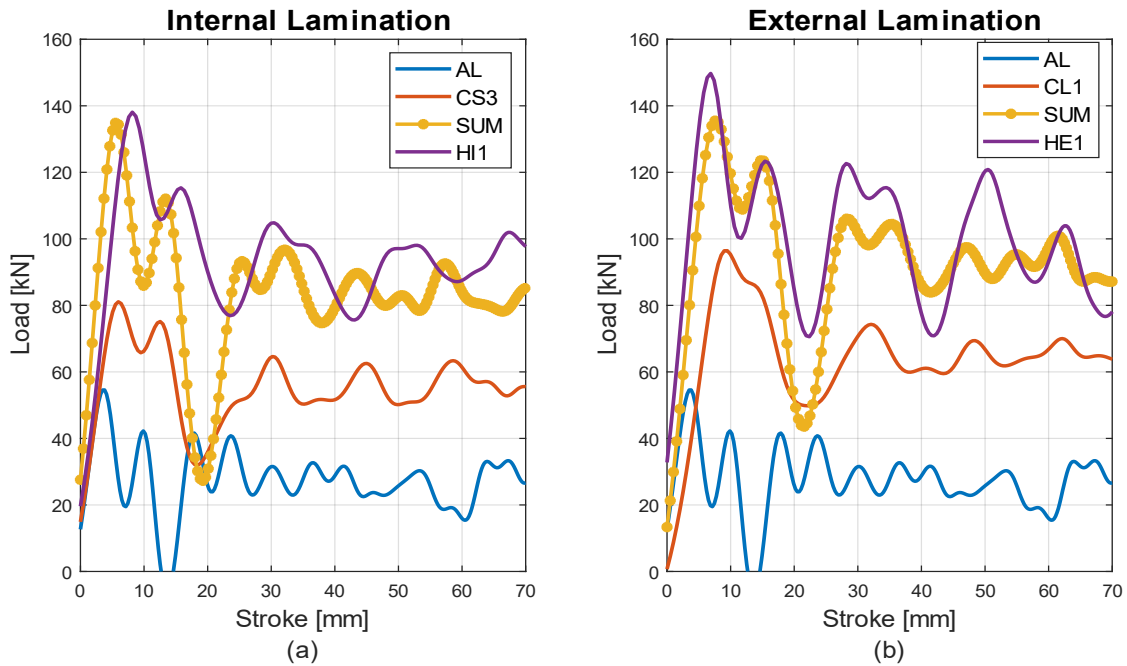


Figure 3.25: Hybrid vs. AL+CFRP

Table 3.10 reports the results in terms of energy absorption of the tests computed considering only 70mm of stroke. The values are averaged between the component of the same group (C\_L, C\_S, H\_E, H\_I). Considering the difference of energy between hybrid and sum of bare material, it is evident that FML tubes perform better than summation, meaning that interaction between two material is beneficial. In addition, the internal lamination configuration has a beneficial difference greater than external lamination.

Table 3.10: Crashworthiness parameters relative to 70 mm of stroke.

	Absorbed energy [J]				SEA [J/g]		
	Average CFRP	Sum AL+AvgCFRP	Average Hybrid	Difference Hybrid-Sum	Average Hybrid	Average CFRP	Difference
Internal Lamination	3725	5647	6433	+14%	49.7	54.5	-9.85%
External Lamination	4575	6496	7233	+11%	50.7	55.3	-9.16%



The performance in terms of SEA over 70 mm of displacement is won by the bare composite material. Moreover, the externally laminated FML tubes perform similarly to H\_I series. This is because the breakage of the external lamination is evident on the load curve in the range between 50-100 mm of stroke.

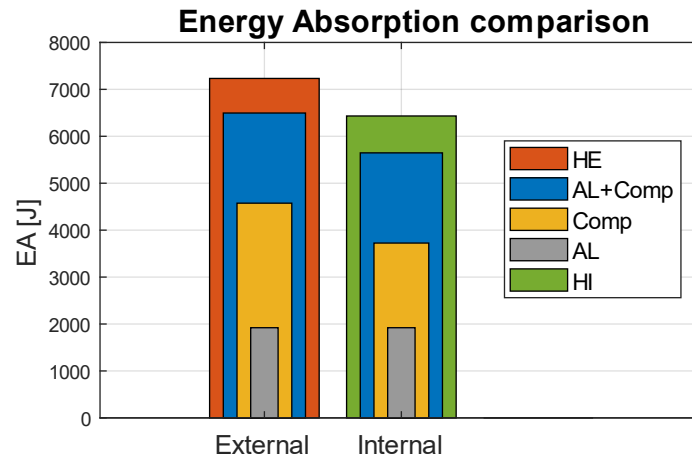


Figure 3.26: Bar graphic data of Table 3.10.

All the tested specimens are shown in Figure 3.27.



Figure 3.27: Post-crush specimens.

## 4 Numerical simulation

Simulating the complex failure modes of the hybrid FML materials is challenging, but their ability to predict simple to complex mechanical behavior under certain conditions is advantageous. Finite elements models are useful, especially if considered the very low cost compared to experimental studies. In addition, simulation provides insights into failure mechanisms and failure progression which are not observable during physical testing.

### 4.1. Numerical model

In structural design, the use of Finite Element Method (FEM) codes is a popular choice as it gives the chance of both speeding up the process and increasing precision. On the other hand, the designer must be sure that the model is correctly representing the reality. One of the aspects that have to be taken into consideration is the choice of a truthful material model, especially when dealing with composite materials that do not behave in a simple way.

The first step to be done when approaching numerical modeling of composites is the choice of the structural model. The plate theory was developed for this purpose, where the plane-stress condition is applied and the corresponding numerical equivalent is represented by the shell element. Layup sequence is implemented using Classical Lamination Theory (CLT)<sup>3</sup>, where each through-the-thickness integration point corresponds to a determined ply. Shell elements are very efficient but they lack precision in respect to solid elements. On the other hand, the use of solid elements will result in an exponential increase of the computational time. Thick shell elements were developed in order to consider the out-of-plane shear resistance by adding additional degrees of freedom, discarding Kirchhoff hypothesis. Here the laminated tube and the metal tube are modeled by a single shell element and the connection between the constituent is achieved by adding additional constraints. Despite the missing capability of representing composite interlaminar behavior, the shell approach is the most preferred one thanks to its balance between accuracy and efficiency. Steel-composite hybrid tubes were geometrically modeled as two-layer cylindrical shells and good results

---

<sup>3</sup> CLT is a commonly used predictive analytical model which makes it possible to analyze complex coupling effects that may occur in composite laminates. It is able to predict strains, displacements and curvatures that develop in a laminate as it is mechanically and thermally loaded. The method is similar to isotropic plate theory, with the main difference appearing in the lamina stress-strain relationships [95].

are provided, so the single layer for each material is applied as approximation of the real problem [82].

The simulations performed in this thesis are obtained through the commercial software LS-DYNA®, a popular dynamic explicit solver mostly suited for crash and impact simulations. The following presents and briefly explains the theory of the material models employed to define composite and ductile material, as well as the adhesive interface between the constituent of the hybrid tubes.

#### 4.1.1. Laminated composite fabric material model

LS-DYNA presents a vast choice in terms of orthotropic material models [83]. A brief overview of the composite material cards is reported in [84], while reference [85] shows a comparison between different models, suggesting the use of material type 58 to model the composite shell tube

The material model in LS-DYNA was based on Hashin's damage mechanics model [86]. The model has the capability of modeling the damage independently in the principal directions of orthotropic materials. Failure is assumed to be caused by stresses acting on the planes. The failure criteria are divided into tensile and compressive mode, and gathered into quadratic polynomial form as follows:

- (a) In tensile fiber mode  $E_1, E_2, G_{12}, \nu_{12}, \nu_{21} = 0$  after lamina failure

$$\sigma_1 > 0 \text{ then } e_f^2 = \left(\frac{\sigma_1}{X_t}\right)^2 - 1 \quad \begin{cases} \geq 0 & \text{failed} \\ < 0 & \text{elastic} \end{cases} \quad (4.1)$$

- (b) Compressive fiber mode causes fiber buckling. Hence, the parameters  $E_1, \nu_{12}, \nu_{21} = 0$

$$\sigma_1 < 0 \text{ then } e_c^2 = \left(\frac{\sigma_1}{X_c}\right)^2 - 1 \quad \begin{cases} \geq 0 & \text{failed} \\ < 0 & \text{elastic} \end{cases} \quad (4.2)$$

- (c) When the matrix begins to crack, the enters the tensile matrix mode, causing the values of  $E_1, G_{12}, \nu_{12}$  to be zero.

$$\sigma_2 > 0 \text{ then } e_m^2 = \left(\frac{\sigma_2}{Y_t}\right)^2 + \left(\frac{\tau_{12}}{S_c}\right)^2 - 1 \quad \begin{cases} \geq 0 & \text{failed} \\ < 0 & \text{elastic} \end{cases} \quad (4.3)$$

- (d) When the lamina fails, the material constants  $E_1, G_{12}, \nu_{12}, \nu_{21}$  are set to zero. Accordingly, the failure mode is called the compressive matrix mode.

$$\sigma_2 < 0 \text{ then } e_d^2 = \left(\frac{\sigma_2}{2S_c}\right)^2 + \left(\frac{\tau_{12}}{S_c}\right)^2 - 1 \quad \begin{cases} \geq 0 & \text{failed} \\ < 0 & \text{elastic} \end{cases} \quad (4.4)$$

As it is presented in Figure 3.1,  $\sigma_1$  is the stress in the fiber direction,  $\sigma_2$  is the stress perpendicular to fiber direction,  $\tau_{12}$  is the shear stress in the lamina plane,  $\nu_{12}$  and  $\nu_{21}$  are the major and minor Poisson's ratio, respectively. The parameters  $X_t, X_c, Y_t, Y_c, S_c$  are the limit strength.

For the plane stress condition, the constitutive equation is given as:

$$\begin{pmatrix} \sigma_1 \\ \sigma_2 \\ \tau_{12} \end{pmatrix} = \frac{1}{C} \begin{pmatrix} (1-\omega_1)E_1 & (1-\omega_1)(1-\omega_2)v_{21}E_2 & 0 \\ (1-\omega_1)(1-\omega_2)v_{12}E_1 & (1-\omega_2)E_2 & 0 \\ 0 & 0 & C(1-\omega_s)G \end{pmatrix} \begin{pmatrix} \varepsilon_1 \\ \varepsilon_2 \\ \gamma_{12} \end{pmatrix} \quad (4.5)$$

$$C = 1 - (1-\omega_1)(1-\omega_2)v_{21}v_{12} \quad (4.6)$$

Variables denoted as  $\omega_i$  ( $i=1, 2, s$ ) are called damage function, defined for  $\omega_i < 0$ .

The failure surfaces which bound the elastic region can be **extrapolated** starting from the failure criteria by substituting the stresses of equation(4.1):

$$f_{\parallel} = \frac{\sigma_1^2}{(1-\omega_{1c,t})^2 X_{c,t}^2} - r_{\parallel c,t} = 0 \quad (4.7)$$

$$f_{\perp} = \frac{\sigma_2^2}{(1-\omega_{2c,t})^2 Y_{c,t}^2} + \frac{\tau_{12}^2}{(1-\omega_s)^2 S_c^2} - r_{\parallel c,t} = 0 \quad (4.8)$$

Where the loading surfaces are  $f_{\parallel}$  for the fiber modes and  $f_{\perp}$  for the matrix modes. The damage threshold  $r$  defines the size of the elastic region.

A more general solution has been developed in order to allow for almost complete uncoupling of the failures. If the failure criteria are taken as independent, non-smooth failure surfaces are obtained as:

$$f_{\parallel} = \frac{\sigma_1^2}{(1-\omega_{1c,t})^2 X_{c,t}^2} - r_{\parallel c,t} = 0 \quad (4.9)$$

$$f_{\perp} = \frac{\sigma_2^2}{(1-\omega_{2c,t})^2 Y_{c,t}^2} - r_{\perp} = 0 \quad (4.10)$$

$$f_s = \frac{\tau_{12}^2}{(1-\omega_s)^2 S_c^2} - r_s = 0 \quad (4.11)$$

Sets of parameters  $\epsilon_i$  ( $i = 1T, 1C, 2T, 2C, S$ ) and  $SLIM_i$  ( $i = T1, C1, T, C2, S$ ) are introduced. Values for tension and compression, in direction 1 and 2, take into account accounts for the one-sidedness of the phenomenon, while direction 12 (defined as  $S$  in parameters index) is assumed to be independent from the sign of the shear stress.  $\epsilon_i$  is defined as the strain at the maximum stress response and  $SLIM_i$  is the ratio of the limiting stress to the peak stress ( $1 \leq SLIM_i < 0$ ),  $SLIM_i = 1$  corresponds to no strain softening.

A parameter study indicated that varying  $\epsilon_i$  changed the slope of the pre- and post-peak response, a greater  $\epsilon_i$  value results in a smaller slope of the stress-strain response.  $SLIM_i$  sets a predefined limiting stress. At the limiting stress, the damage law is described by [87]:

$$\omega = 1 - \frac{SLIM_i X_i}{E \epsilon_i} \tag{4.12}$$

Typical stress–strain curves for various values of  $Ei$  and  $SLIMi$  are shown in Figure 4.1.

In Figure 4.1 it is evident how parameter  $SLIMi$  define the minimum stress limit of damaged material.

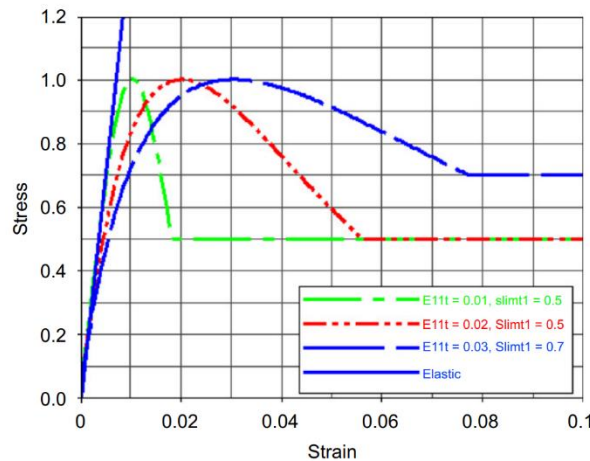


Figure 4.1: Examples of stress–strain responses for various  $Ei$  and  $SLIMi$  values, MAT58b.

An overview of the material model implementation is now given by highlighting the most relevant parameters. Table 4.1 is a representation of the material card [83].

Table 4.1: \*MAT\_058 card overview

MID	RO	EA	EB	EC	PRBA	TAU1	GAMMA1
GAB	GBC	GCA	SLIMT1	SLIMC1	SLIMT2	SLIMC2	SLIMS
AOPT	TSIZE	ERODS	SOFT	FS	EPFS	EPSR	TSMD
XP	YP	ZP	A1	A2	A3	PRCA	PRCB
V1	V2	V3	D1	D2	D3	BETA	LCDFAIL
E11C	E11T	E22C	E22T	GMS			
XC	XT	YC	YT	SC			

In LS-DYNA model the letters  $A, B, C$  correspond to material axis 1,2,3 define in Figure 3.1.

In addition to elastic constants and the strength-related parameters, in \*MAT\_058 material definition there are important non-physical variables that can change significantly the material behavior:

- ERODS: This is the maximum effective strain which determines the element deletion (complete failure). If lower than zero, element fails when effective strain calculated from the full strain tensor exceeds ERODS.
- FS: Failure Surface type, which define the use of equations (4.7),(4.8) or (4.9),(4.10),(4.11). If failure criteria are taken as independent, non-linear shear behavior can be obtained through parameters GAMMA1, TAU1, GMS, SC. In Figure 4.2 is represented the method.

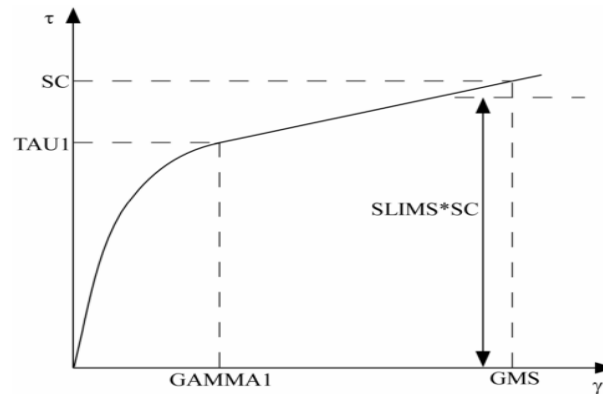


Figure 4.2: Stress-strain diagram of shear [83].

- TAU1, GAMMA1: Are the stress and strain limits of the first slightly non-linear part of the shear stress versus shear strain curve. Values are used to define the curve of shear only for FS=-1.
- SOFT: This is a parameter related to the crash-front algorithm. In order to obtain a realistic crack propagation, once an element is deleted, all adjacent to it are subject to a stress reduction during the softening part.
- TSIZE: Element is deleted when the time step is smaller than the given value.

In the following are reported all the data to define the composite fabric material.

Table 4.2: CFRP Laminate MAT058 parameters.

$\rho$	1.41 g/mm <sup>3</sup>	Table 3.3
$E$	66.30 GPa	$EA = EB$ , Table 3.1
$\nu$	0.0385	Table 3.1
$\varepsilon_T^{max}$	0.0108	$E11T = E22T$ , Table 3.1
$\varepsilon_C^{max}$	0.024	$E11C = E22C$ , value obtained from [75].
$X^C$	570.0 MPa	$XC = YC$ , value obtained from [75].
$X^T$	751.16 MPa	$XT = YT$ , Table 3.1
$G$	2758 MPa	Table 3.2
$\gamma^{max}$	0.05	Table 3.2
$\tau^{max}$	65.6 MPa	Table 3.2

Table 4.3: Continue of Table 4.2.

$\gamma_1$	0.02	Extrapolated from Figure 3.6
$\tau_1$	46.6 MPa	Extrapolated from Figure 3.6
<i>ERODS</i>	0.35	Defined with trials and errors
<i>SOFT</i>	0.55	Suggested in [88]
<i>SLIMT2</i>	0.01	Small but not zero residual strength is assumed after tensile failure to avoid numerical instabilities [88]
<i>SLIMT1</i>	0.1	Recommended in [83]
<i>SLIMC</i>	0.8	SLIMC1=SLIMC2=SLIMS, suggested value in [83] is 1, reduced after trials and errors.
<i>FS</i>	-1	

#### 4.1.2. Piecewise linear plasticity material model

The LS-DYNA material type 24 (\*MAT 024) is the most widespread material model in use today for the modeling of impact phenomena relative to elasto-plastic, isotropic materials with an arbitrary stress versus strain curve and arbitrary strain rate dependency designable in the model.

\*MAT 024 is based on Von Mises theory to describe the material behavior; it follows Von Mises yield surface to determine the yield condition as shown in Figure 4.3.

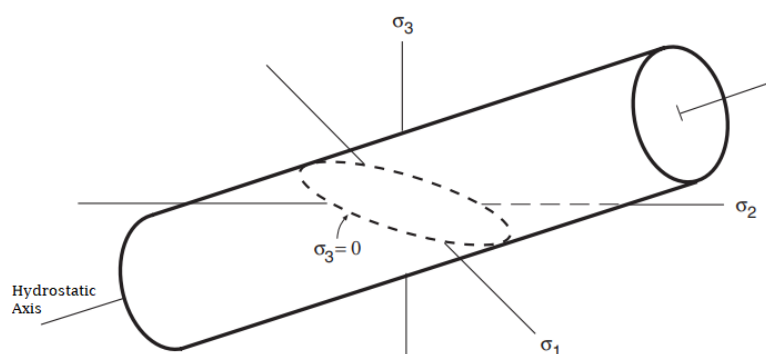


Figure 4.3: Von Mises criterion [89].

The elastic region is modeled as rate independent up to an arbitrarily or otherwise determined yield point, beyond which the stress-strain curve at the lowest strain rate of interest is decomposed into an elastic-plastic model. This produces a curve of stress function plastic strain, hereafter referred to as the plasticity curve. The accuracy of this model, when applied to plastics, depends on the stress-strain

relationship being linear up to the chosen yield point, that this initial linearity is not rate dependent and that the shape of the plasticity curve is uniform and independent of strain rate. This is simply not true for most plastics, but valid for ductile material. Due to the lack of data regarding the rate dependency of the material, it is considered as rate independent also in the plasticity region.

The plastic material behavior is defined by a curve of points expressed from yielding point to the failure limit point.

The plastic curve is not directly measured by tensile test, but obtained via Ramberg–Osgood power law relation [89]:

$$\sigma_p = H \varepsilon_p^n \quad (4.13)$$

$$H = \frac{\sigma_{yield}}{\left(\frac{\sigma_{yield}}{E}\right)^n} \quad (4.14)$$

Where  $\sigma_p$ ,  $\varepsilon_p$  are stress and strain in the plastic region ( $\sigma > \sigma_{yield}$ ),  $n$  and  $H$  are the strain hardening exponent and the strain hardening coefficient. Hardening parameters are obtained fitting test loading curves, in our case for Aluminum 6061 the value of exponential value is  $n = 0.13$  [90].

In Table 4.4 is reported the material card for \*MAT\_024.

Table 4.4: \*MAT\_024 card overview

MID	RO	E	PR	SIGY	ETAN	FAIL	TDEL
C	P	LCSS	LCSR	VP			

In addition to the familiar elastic parameters, the variables useful in the conducted simulation are:

- SIGY: yield stress value.
- LCSS: Load Curve of plasticity region, the first value in stress must be equal to SIGY.

Figure 4.4 reports the plastic stress-strain curve of ductile material employed in the experimental test, obtained by using equation (4.13),(4.14) and material characteristic given by the material manufacturer. The data of the curve are directly associated to \*mat\_024 card via LCSS card option.

The following table reports all the data to define the ductile material.



Table 4.5: Aluminum 6060 MAT024 constants.

$\rho$	2.258 $g/mm^3$	Table 3.3
$E$	65.7 $GPa$	Suggested by material manufacturer
$\nu$	0.33	Suggested by material manufacturer
$\varepsilon^{max}$	0.14	Suggested by material manufacturer
$\sigma_{yield}$	137.3 $MPa$	Suggested by material manufacturer

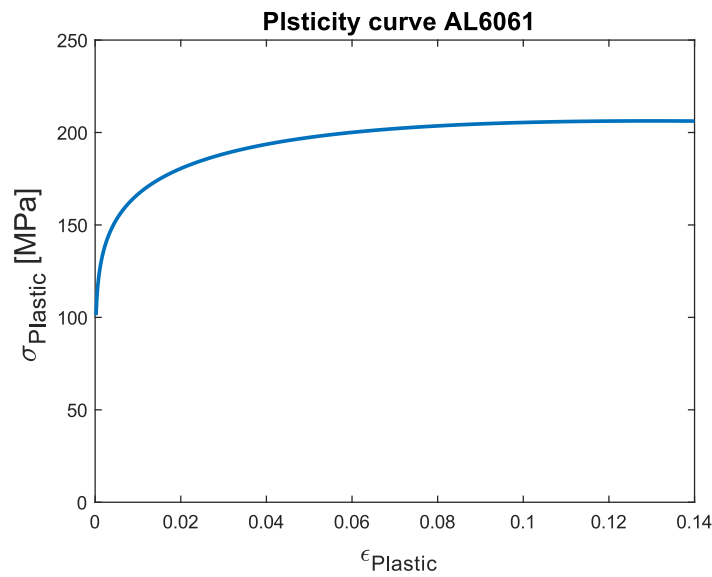


Figure 4.4: Plastic region for AL6061.

#### 4.1.3. Aluminum-composite delamination model

The interaction between composite and ductile tube is modeled as delamination phenomena. Delamination modelling has several approaches in LS-DYNA. Tiebreak contacts have been vastly used, and it is proven to be a robust contact algorithm and relatively simple. Depending on the model of study, different contacts can be employed to achieve better prediction [91].

In the case of study, in order to replicate the adhesive interface CFRP-AL tube and model delamination behavior between the constituent, the contact card is applied. \*CONTACT\_AUTOMATIC\_ONE\_WAY\_SURFACE\_TO\_SURFACE\_TIEBREAK.

One-way contact types allow for compression loads to be transferred between the slave nodes and the master segments.

The algorithm ties nodes that are initially in contact by creating a linear spring, and the debonding of the surface initiates when the maximum stress criterion is

met, which leads to scaling down of the stress by a linear damage curve until the critical separation is reached and the spring is removed [92].

The failure stress tiebreak criterion is defined as:

$$\left(\frac{|\sigma_n|}{NFLS}\right)^2 + \left(\frac{|\sigma_s|}{SFLS}\right)^2 \geq 1 \quad (4.15)$$

In which  $\sigma_n$  and  $\sigma_s$  are the normal and shear stresses acting at the interface, and NFLS, SFLS are the normal and shear strength of the tie, respectively.

In Table 4.6 is reported the material card for Tiebreak contact:

Table 4.6: \*AUTOMATIC\_ONE\_WAY\_SURFACE\_TO\_SURFACE\_TIEBREAK card overview

SSID	MSID	SSSTYP	MSTYP	SBOXID	MBOXID	SPR	MPR
FS	FD	DC	VC	VDC	PENCGIK	BT	DT
SFS	SFM	SST	MST	SFST	SFMT	FSF	VSF
OPTION	NFLS	SFLS	PARAM	ETAEN	ERATES		

The variables useful in the conducted simulation are:

- FS, FD: Static and dynamic friction coefficient respectively.
- SST, MST: Optional thickness for slave and master surface (overrides true thickness). This option applies only to contact with shell elements. These parameters have no bearing on the actual thickness of the elements, it only affects the location of the contact surface.
- NFLS, SFLS: the same as equation (4.15).
- PARAM is the critical distance at which the failure occurs (i.e., deletion of tiebreak and advancing of delamination).
- OPTION: Type of response of the contact. OPTION=8 is the most common option for the use of tiebreak contacts for delamination analysis. Tiebreak is active for nodes which are initially in contact. Failure stress must be defined for tiebreak to occur. After the failure stress tiebreak criterion is met, damage is a linear function of the distance between points initially in contact. When the distance is equal to PARAM damage is fully developed and interface failure occurs. After failure, the contact behaves as a surface-to-surface contact [83].

Constants defining the contact card are reported in the following Table 4.7.

Table 4.7: Tiebreak contact card parameters.

FS	0.15	Suggested in [93]
FD	0.14	Suggested in [93]
SST	3.5 mm	Table 2.5
MST	1.5 mm	Table 2.5
NFLS	12 MPa	Suggested in [94]
SFLS	36 MPa	Suggested in [94]
PARAM	0.025 mm	Suggested in [91]

## 4.2. Model build-up

Other important choices taken to model the hybrid tube and replicate the drop tower test are described in the following subchapters.

Among all element formulation implemented in LS-DYNA for shells, a fully integrated (4 points per integration point) element formulation (ELFORM=16) was chosen because of its accuracy and cost. Both metal and composite tubes are modeled with a mesh size of 2x2 mm. Aluminum tube shell has the number of through shell thickness integration points set to 2 by default.

The composite stacking sequence is defined by \*PART\_COMPOSITE card, which provides a simplified method of defining a composite material model for shell elements. The material ID, thickness and material angle are defined for all the through-thickness integration point, representing the layers of the laminate.

For both AL and CFRP tube surfaces a contact definition is applied to avoid auto-penetration of the surfaces during the crash, via the card \*CONTACT\_AUTOMATIC\_SINGLE\_SURFACE.

The constrain of the plug at the base of the tubes is simulated applying a boundary condition only on the displacement of the first nodes of the base. Moreover, a fixed

planar rigid wall at the base of the tube representing the base plate of the drop tower system, is defined.

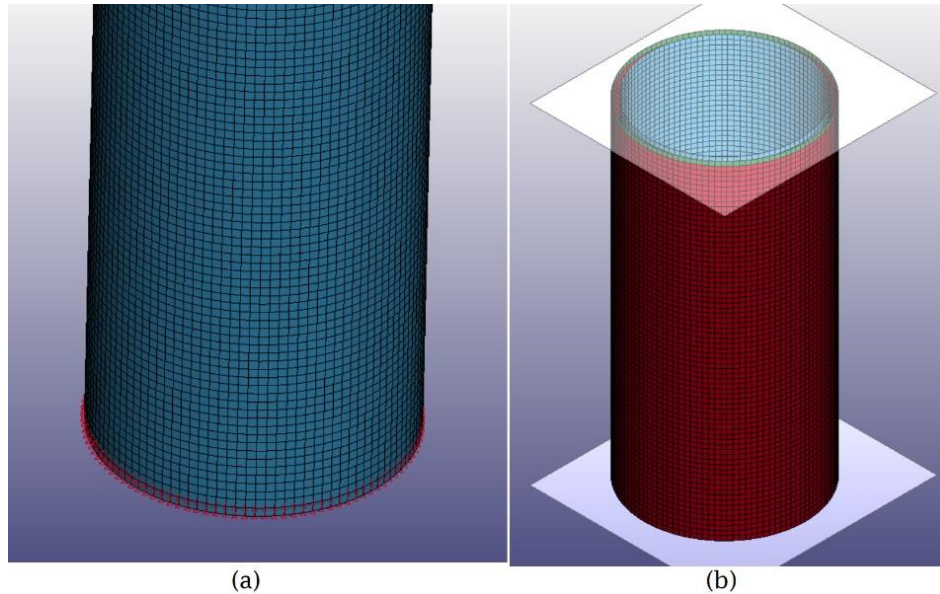


Figure 4.5: Model (a) constrained nodes, (b) rigid walls.

The impacting mass is modeled via a moving planar rigid wall at the top of the tube. A mass of 350 Kg as the performed test is imposed on the rigid wall. A velocity corresponding to the impact velocity measured from test results is associated (Table 3.9).

The moving rigid wall directly extrapolates the stroke, velocity and the forces exercised from the tube crushing reaction during the impact.

In the early phase of the modeling and testing, the global response of the bare composite tube model is never a progressive crushing, but it is a catastrophic response, not corresponding to the test results. Therefore, a defect is introduced at the top of the numerical model to initiate the crushing front. The defect is modeled with a reduction of thickness in the first millimeter of the composite tube end, in Figure 4.6 is showed the constituent of the hybrid tube with visible thickness to better comprehend the design of the defect.

It is known that the defect acts as a trigger (1.3.4) and the real composite tube is not finished with such feature. It is a choice made to obtain primitive simulation results taking into account that the trigger mechanism does influence the initial impact force and do not much influence the total energy absorption. But this was necessary to obtain results close to reality.

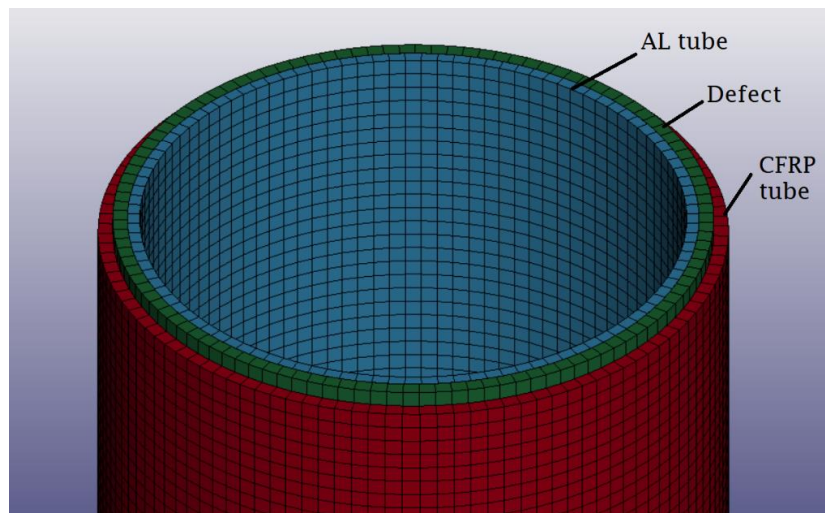


Figure 4.6: External lamination hybrid tube FE model.

The data acquisition during the simulations is performed with a frequency of 50 KHz, the results are then filtered with the same class (CFC180) employed in the experimental tests.

## 4.3. Results

The results from the simulations are here presented, the crashworthiness parameters are reported in the subchapter and the error respect to the experimental results is considered as:

$$Error\% = 100 \cdot \frac{Numerical - Experimental}{Numerical} \quad (4.16)$$

### 4.3.1. Aluminum tube numerical model results

Figure 4.7 reports the aluminum tube after the impact simulation. It is noted that the number of folding for the ring mode and diamond mode are the same as experimental results, the difference between the results is two rings folding mode at the base of the FE model tube base

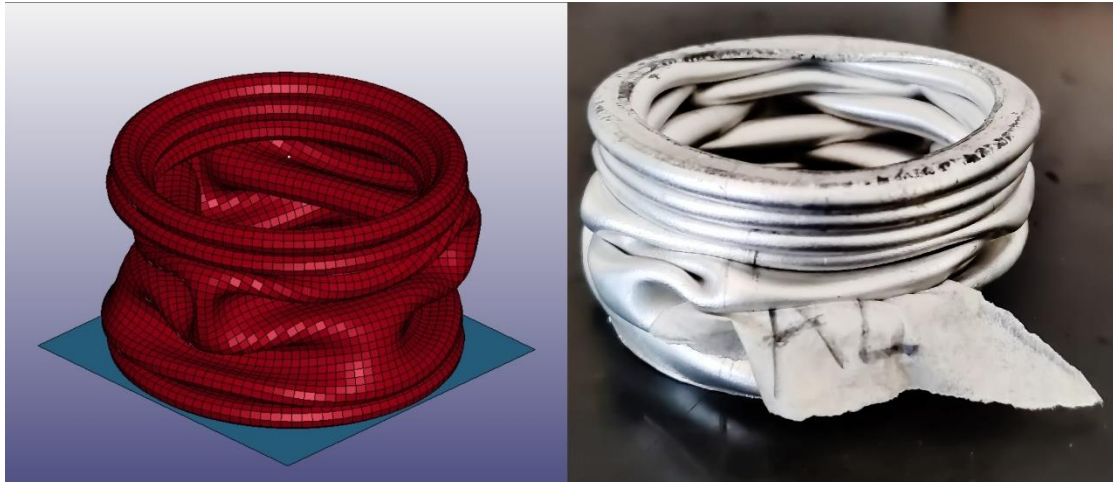


Figure 4.7: Model after impact numerical vs experimental

Figure 4.8 presents the load trend during the impact of the numerical model, reported with the experimental result. From the graph, it is evident the IPCF of the numerical model is lower than real test and the rest of the curve has the same peak in terms of load value at the same stroke. The last peak of the experimental curve, which corresponds to the diamond mode folding, is not reported by the FE model. This difference is probably caused by the ring mode at the base that triggers the peaks of the diamond folding mode later in the stroke. Table 4.8: AL tube comparison of numerical model impact results reports the crush parameters.

Table 4.8: AL tube comparison of numerical model impact results.

	$MF$ $kN$	$IPCF$ $kN$	$EA$ $J$	$\delta$ $mm$	$SEA$ $J/g$	$CFE$
Experimental	26.38	54.26	2662	100	31.95	0.49
Numerical	27.39	40.327	2838	100	34.056	0.68
Error	+3%	-34%	+6%	/	+6%	+27%

The impacting mass of both experimental and numerical simulation reach over 100 mm of displacement, therefore the stroke and all the parameters are calculated over 100 mm of stroke.

Despite the differences in Initial Peak Crushing Force (IPCF) and final peak in the displacement, the mean force, energy and specific energy absorbed are close to the experimental test. By analyzing the results, it can be stated that the numerical model is a good representation of the real test. The initial load reports a difference more than 30% in respect to experimental test, that reflects a similar trend in CFE difference value.

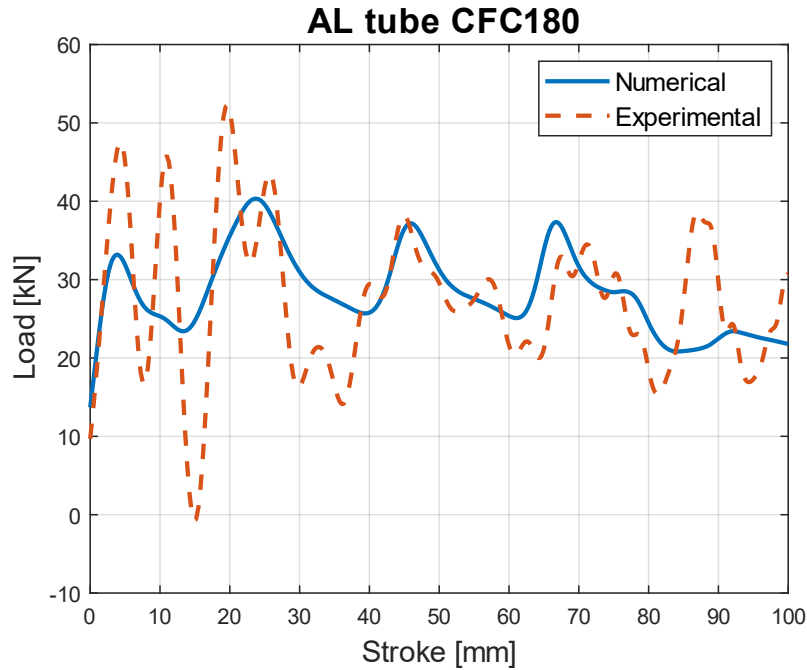


Figure 4.8: Numerical vs experimental load curves AL tube.

#### 4.3.2. Numerical model: composite tube

The following models the behavior of the large composite tube under axial crushing loading with an impact velocity of 5.5 m/s, the C\_L\_1 specimen.

Figure 4.9 shows the simulation of the impact. Debris is not evident in the picture because of LS-dyna representation of the deleted elements during the simulation. Therefore, the shell elements deleted that cause the reduction of length during the impact, are elements that reach the failure strain and do no longer participate in the phenomena, see Figure 4.10(a). This behavior is comparable to the brittle fragmentation of real tested specimen.

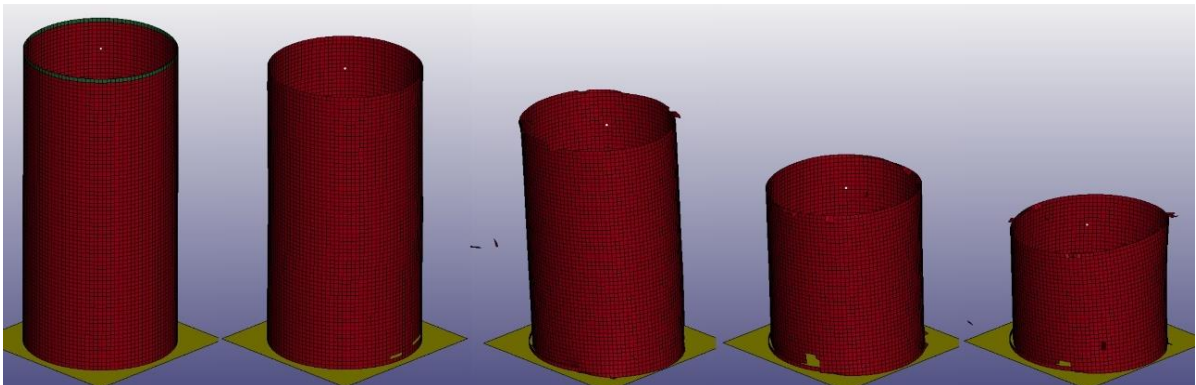


Figure 4.9: C\_L\_1 numerical simulation.

Notice the simulation does not catch the actual crushing dynamic of the experiments, because of the second crushing front that propagates from the bottom, see Figure 4.9 and Figure 4.10.

Despite the design of a defect on the top of the tube, that actually initiate a crushing front, the base constrain nodes are eventually stresses to the point of failure.

The bottom crushing front causes the rotation of the tube during the collapse (third frame of Figure 4.9). Figure 4.10 (b1) shows the large damage at the bottom that causes the rotation of the tube during the crushing (Figure 4.10 (b2)). The composite tube progressively fails, in a controlled manner, despite the rotation of the longitudinal axis.

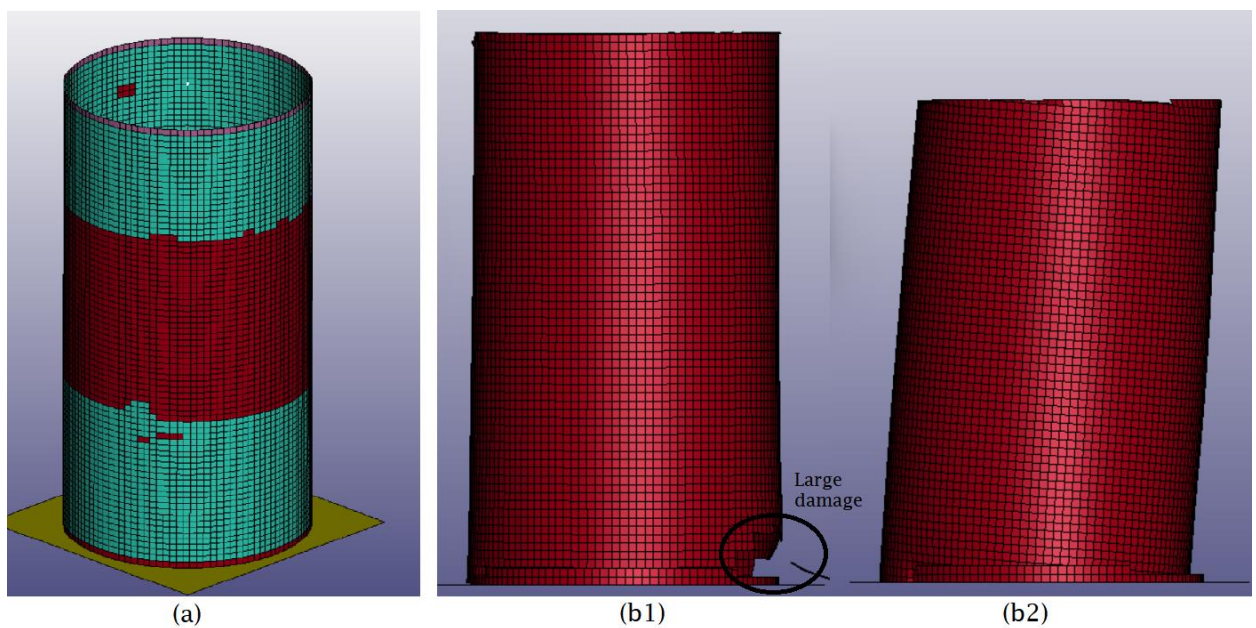


Figure 4.10: (a) deleted shell elements in simulation, (b) damage causing the rotation.

Figure 4.11 shows the load trend of the simulation during the displacement of the impact mass. It is evident that the model cannot capture the initial impact load, showing almost half of the test IPCF. After 20 mm of stroke the numerical results show an increasing trend in crush load, which is caused by the double crush front initiating from top and bottom.

If the class of filter is changed, the final leg of the curve is influenced by wider oscillations and the last peak acts on a wider time interval in respect to the



previous peaks. Therefore, the high value load is not an isolated peak at the end of the stroke, it is not reduced by the filtering as much as the previous peaks, see Figure 4.12.

Table 4.9 reports the crush parameters of the simulation.

Table 4.9: C\_L\_1 tube comparison of numerical model impact results

	<i>MF</i>	<i>IPCF</i>	<i>EA</i>	$\delta$	<i>SEA</i>	<i>CFE</i>
	<i>kN</i>	<i>kN</i>	<i>J</i>	<i>mm</i>	<i>J/g</i>	
Experimental	63.08	88.15	5437	89	56.58	0.72
Numerical	56.87	64.61	5084	91	47.35	0.88
Error	-11%	-36%	-7%	+2%	-19%	+18%

Right from the load curve it is evident that the simulation does not capture the right global behavior of the CFRP tube, especially the initial peak load. On the contrary, the mean force, total stroke and energy absorption values are close to the real experiment. Obviously, the SEA is reduced by almost 20% because of less energy absorbed with more stroke, meaning more material needed.

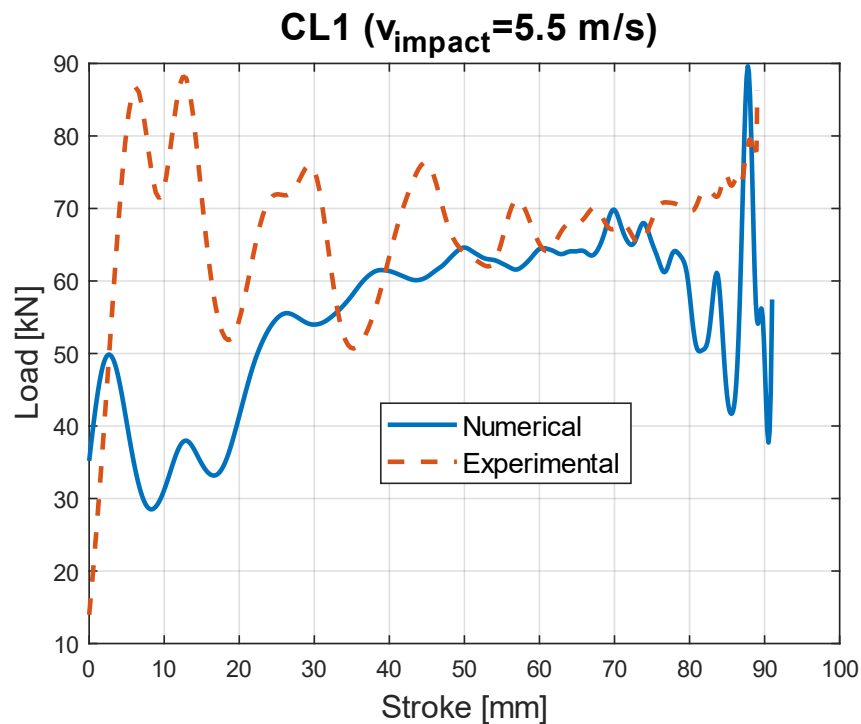


Figure 4.11: Numerical vs experimental load curves C\_L\_1 tube.

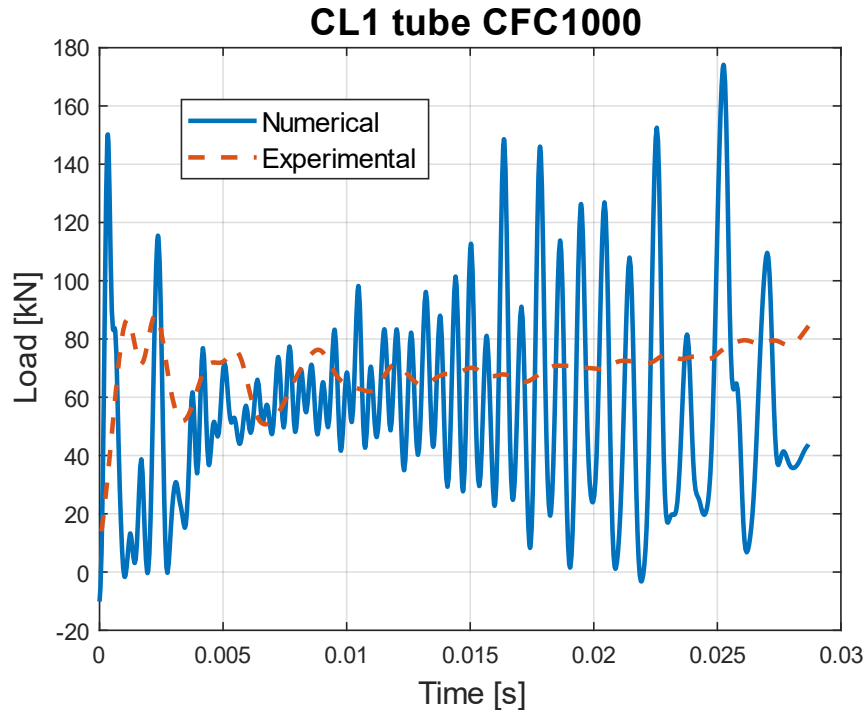


Figure 4.12: Higher class of filtering for C\_L\_1.

### 4.3.3. External lamination hybrid tube numerical model results

The analyzed hybrid tube is H\_E\_1, dropped from the 2.35m with an impact velocity of 6.6 m/s, to be compared with H\_I\_1 tested with the same velocity.

Figure 4.13 reports the external laminated tube behavior during the impact.

In the initial frames the shell elements that reach failure cannot be seen because are directly eliminated, on the other hand, big chunks of composite material remain during the simulation because are generated from crack propagation that will cause the delamination and detachment from the internal tube.

The longitudinal crack, that does not reach the bottom immediately, is also a difference respect to the experimental test (Figure 3.16(c)), but it propagates by steps. In the simulation, the propagation of the longitudinal crack is initiated by the deformation of the aluminum.

Every diamond mode folding propagates the cracks and cause the delamination of composite elements, as it is shown in Figure 4.13 .

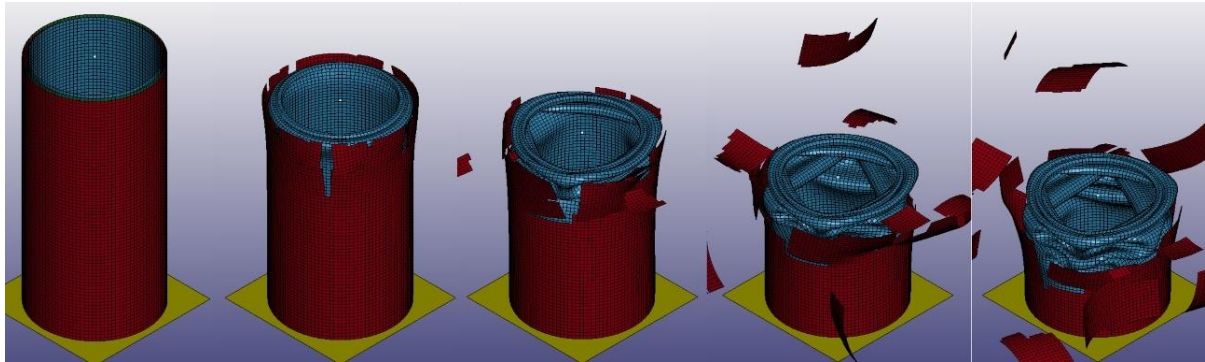


Figure 4.13: H\_E\_1 numerical simulation.

Comparing the post crush experimental specimen and the simulated test, the initial inward folding of Figure 3.17(c) is not captured by the FE model. Instead of inward folding, in the first instants the composite tube resist without axial crack propagation and initiate a ring mode that is contained inside another ring folding mode. It is defined double-ring folding mode, see Figure 4.14.

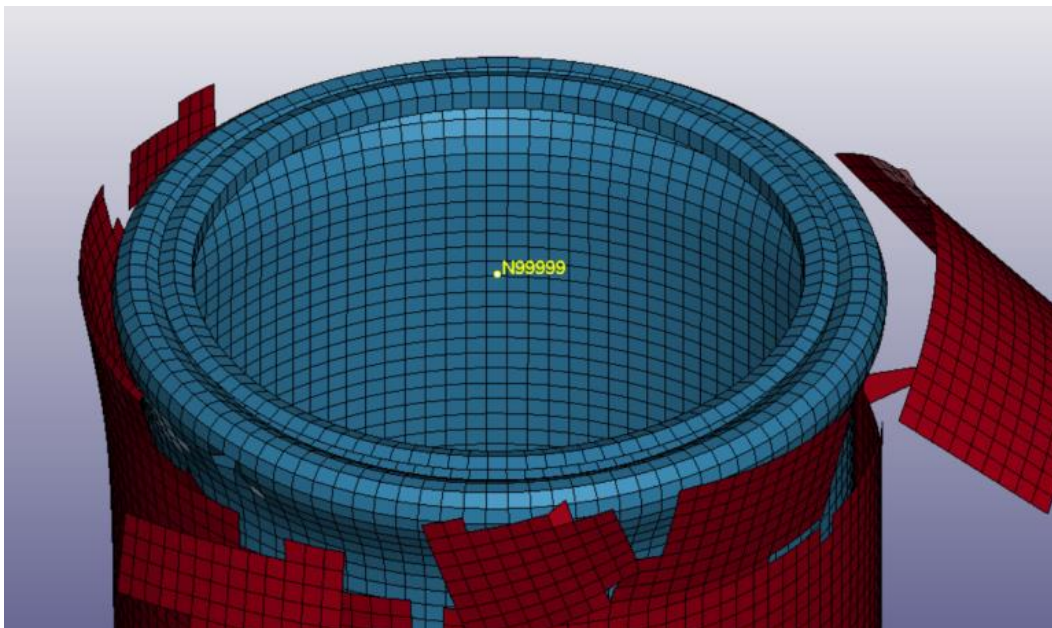


Figure 4.14: Double-ring folding mode.

Figure 4.15 presents the load trend during the impact of the numerical model, reported with the experimental result. The graph shows peak load remains above 140kN of value before 20mm of displacement. This is due to longitudinal cracks

which are not generated yet and the FE model reacts to the impact mass with brittle fragmentation of the tube. After 20 mm of displacement is present a drop of impact load, caused by the generated crack by the double-ring folding of the internal tube. The continued delamination by steps cause the chunk of shell elements to avoid interaction with the impacting mass, therefore, crushing load is defined only by the internal aluminum tube. In the experimental test of H\_E\_1 specimen, when the longitudinal crack is created, the composite tube still participates with a localized brittle failure (Figure 3.16(c)).

Despite the drop of crushing load after 20 mm the impacting mass reach null velocity after 88 mm of stroke, less than the experimental trial. This is caused by the initial peak load, that remain at higher values, absorbing energy of the crash.

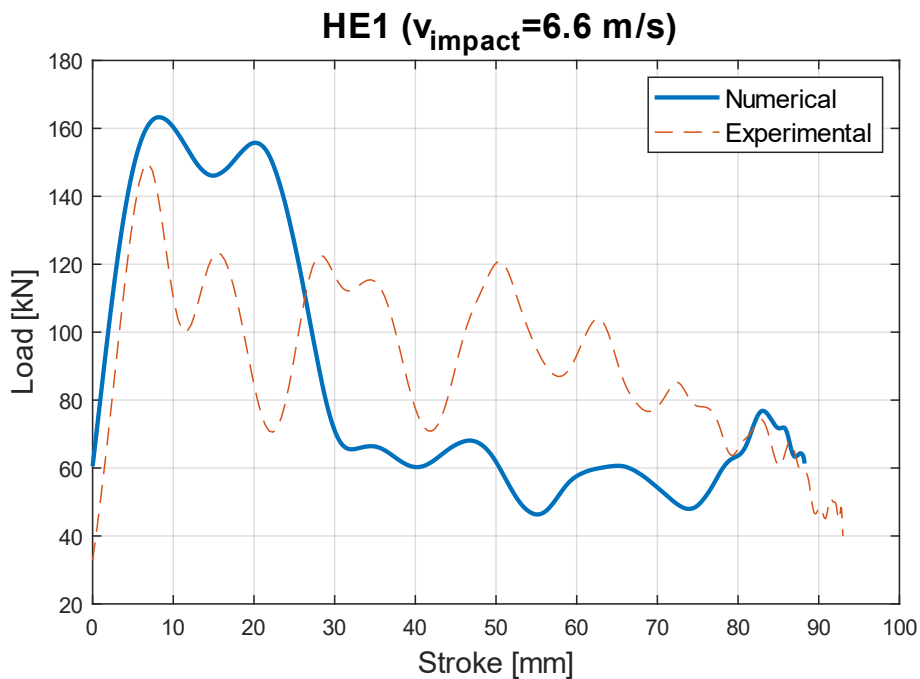


Figure 4.15: Numerical vs experimental load curves H\_E\_1 tube.

Table 4.10 reports the crush parameters. All the crashworthiness parameters remain under 10% of difference in respect to the experimental model. This means that despite the difference in the dynamic behavior of the model, the simulation can capture the global phenomena.

Table 4.10: H\_E\_1 tube numerical model impact result.

	<i>MF</i> <i>kN</i>	<i>IPCF</i> <i>kN</i>	<i>EA</i> <i>J</i>	$\delta$ <i>mm</i>	<i>SEA</i> <i>J/g</i>	<i>CFE</i>
Experimental	70.64	149.21	7783	93	45.33	0.47
Numerical	74.55	163.28	7585	88	41.93	0.45
Error	+4%	+8%	-2%	-5%	+8%	+3%

#### 4.3.4. Internal lamination hybrid tube numerical model results

The FML tube modeled is the H\_I\_1 specimen, with an impacting mass velocity of 6.6 m/s. From Figure 4.16, the difference of dynamics of the outer ductile tube is evident, in respect to experimental tests, compared to the outward folding of Figure 3.19. The simulation cannot capture the mushrooming folding of aluminum tube, so a ring mode folding is obtained. The axisymmetric mode is not progressive because the rings initiated at the beginning on top, bottom and middle due to a local delamination between the constituent. After, the folding propagate from the bottom because the crushing front of the internal CFRP tube starts from the bottom, see Figure 4.17.

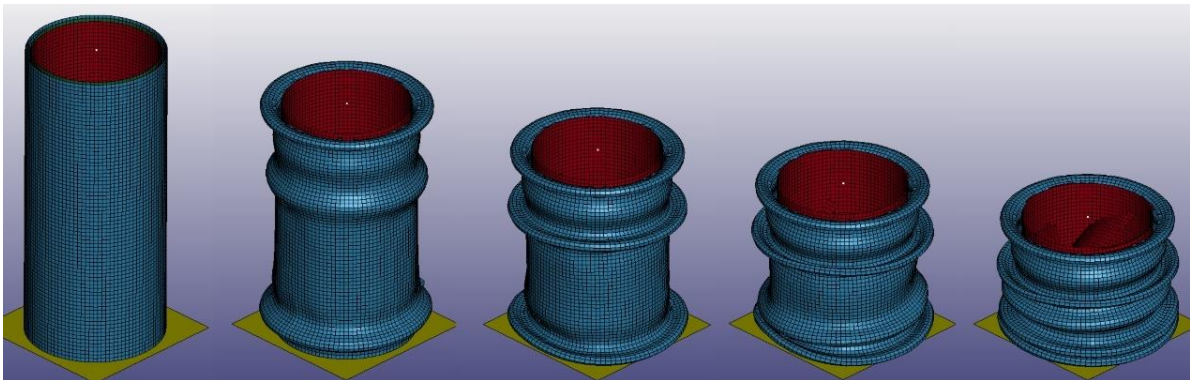


Figure 4.16: H\_I\_1 numerical simulation.

In Figure 4.17 is reported only the internal composite tube during the simulated crushing. In respect to experimental results, the FE model initiate the crash front from the bottom, due to a catastrophic failure at the bottom.

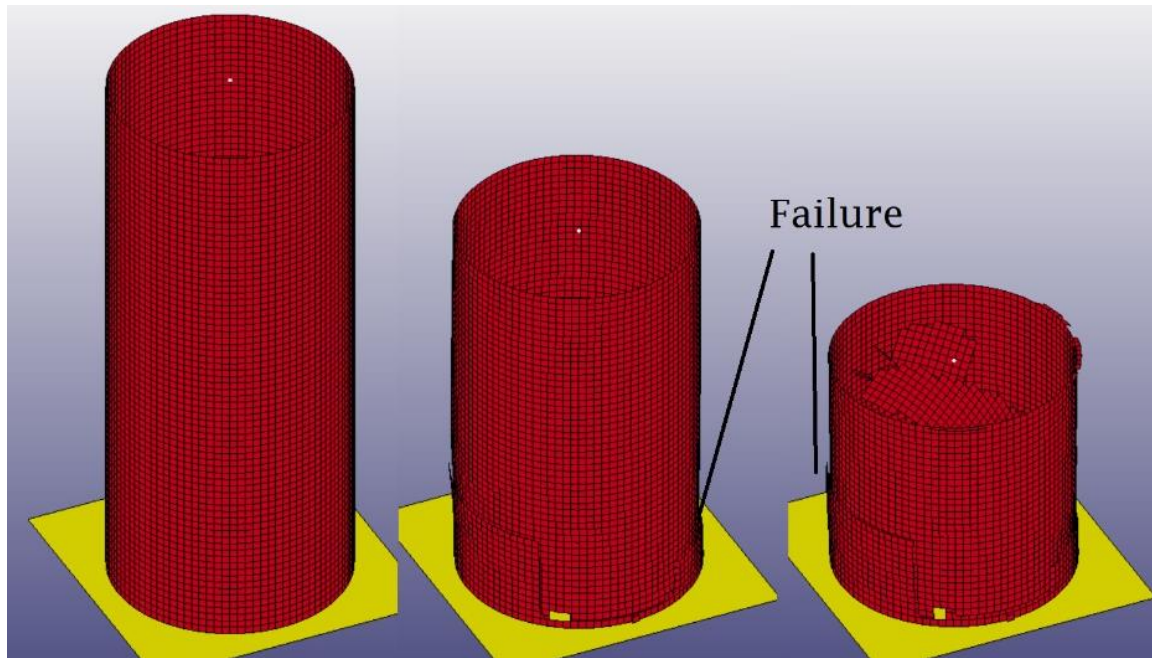


Figure 4.17: H\_I\_1 numerical simulation, internal CFRP tube.

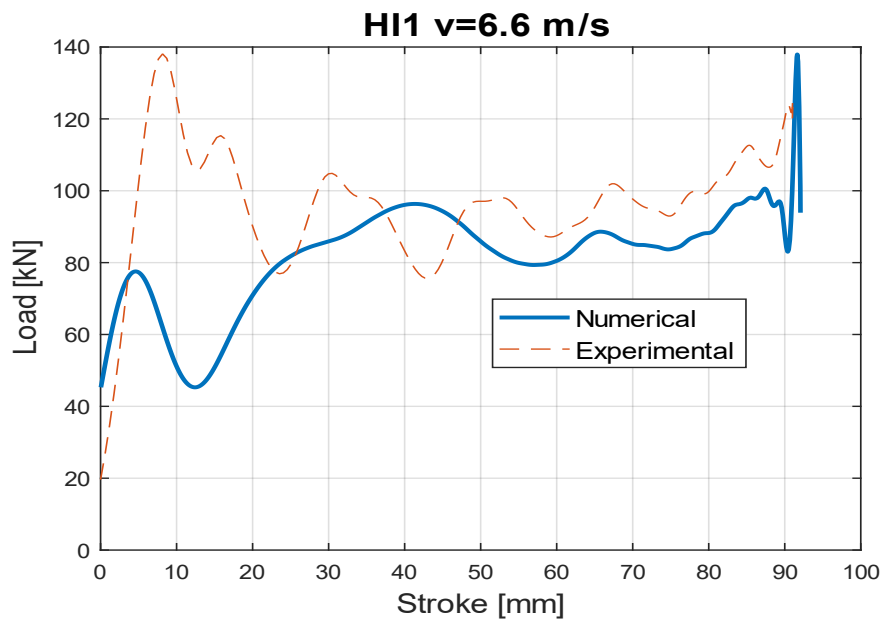


Figure 4.18: Numerical vs experimental load curves H\_I\_1 tube.

Figure 4.18 shows a final peak at the end of the stroke. This situation is similar to the consideration made for the composite tube. As one can see in Figure 4.19, the last peak load is not an isolate event, but a series of oscillation that ends with a wider peak. It is evident that, from Figure 4.18 and Figure 4.19, the curve trend is

similar to the experiment in the phase of folding and crushing, despite the different modes the constituent material tubes show.

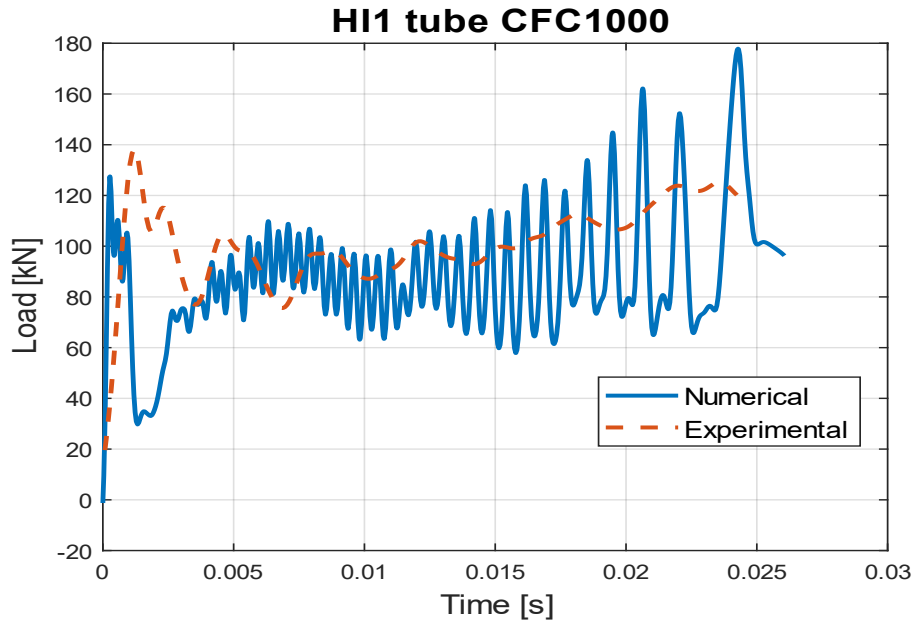


Figure 4.19: Higher class of filtering for H\_I\_1.

Table 4.11 reports the results of the simulation compared with experimental trial. It is noted that despite the much different IPCF, the global results are close to the real test.

Table 4.11: H\_I\_1 tube numerical model impact result.

	<i>MF</i> <i>kN</i>	<i>IPCF</i> <i>kN</i>	<i>EA</i> <i>J</i>	$\delta$ <i>mm</i>	<i>SEA</i> <i>J/g</i>	<i>CFE</i>
Experimental	90.46	137.86	7835	91	52.00	0.66
Numerical	88.18	78.48	7544	92	43.92	1.12
Error	-2%	-75%	-3%	+1%	-18%	+41%

It can be stated that the numerical study of FML tubes captures the global behavior of the crushing tubes in terms of mean force, stroke, and energy absorption. There are flaws in the design caused by the poor composite model, which influence the IPCF of the internal laminated specimen. Moreover, it is known that the single shell modeling is a simple and basic choice of design which causes the actual dynamic of the crushing modes of the bare material to not correspond to the real dynamic.

It must be said that this numerical study is a primitive approach to the simulation of the entire study, knowing that the composite numerical model has flaws in the design and to obtain promising results in the behavior of the FE model. A more intense study in the field is needed. Unfortunately, valid research on the numerical modeling is a thesis by itself.



# 5 Conclusions and future developments

## 5.1. Conclusions

In this work, experimental and numerical simulations of FML crushing tube have been carried out. The outcome is surely positive, as the initial goal of comprehension of materials interaction has been reached.

In the manufacturing process, internal lamination using pre-cut prepregs using overlapping joints was successful in both hybrid and bare composite tube. The use of rubber pad with vacuum bag process, instead of classic method with outside circular mold, shows an easy and versatile process method.

The manufacturing process is indeed valid because the bare composite tubes crushing behavior do not show catastrophic failure. Moreover, the specific energy absorption is similar to literature findings.

It is stated that both hybrid configuration tubes, in terms of energy absorption, perform better than the sum of the bare material tubes. This means energy delamination is a useful “weightless” energy absorption mechanism.

External laminated FML tubes perform better than expected. The dynamic behavior differs from static loading because of the interaction of composite material, after delamination from the internal tube, with the impacting mass. The inward folding of AL tube of specimen H\_E\_2 is a folding mode of hybrid tubes never found in literature. The non-presence of longitudinal cracks permits to exploit the crushing characteristic of composite tubes without catastrophic failure.

Internal laminated FML shows the best performance between two hybrid configurations, in terms of CFE and SEA for crushing length higher than 70 mm. The steady increasing trend load, caused by the compaction of the specimen in the right leg of the curve can be noticed. This is the difference in terms of energy absorption that defines internal lamination shows more performance than external laminated structure.

Bare composite tubes have better SEA than hybrid tubes, especially for stroke under 70mm. H\_I specimen is very close to composite SEA values if long crushing displacement is considered.

Single shell numerical model and the use of \*MAT024 for aluminum tube proved to a good option in terms of simplicity and results to represent the impact loading of the ductile specimen.

The same shell model, with \*MAT058 card, do show average results. The single shell model cannot express the exact failure mode of the experimental tests. It creates two crushing fronts from the top and bottom of the tube. This flaw causes the initial peak load to be almost the half of the real IPCF. Despite that, energy absorption, stroke and mean load results are close to experimental trials, proving that single shell modeling is a fast and simple design to extrapolate overall information regarding crashworthiness parameters.

H\_E FML numerical model crush parameters are all under the 10% of error respect experimental test. The simulation captures the axial crack propagation that happens in H\_E\_3 specimen, but its propagation is defined by steps instead of an immediate crack propagation of experimental results.

H\_I FML numerical model shows good results except for IPCF result which differ by 60%. Stroke, mean force and SEA are all under the 3% of error respect to the experimental results. Low initial peak load is a flaw of the composite model, because also in H\_I numerical model, the internal composite tube is subjected to a crushing front at the bottom of the tube, caused by a brittle failure. The external aluminum tube cannot reproduce the outward “mushrooming” folding mode and instead deforms with ring modes.

The hybrid numerical model with single shells connected with tiebreak contact, proves to be fast and simple in design approach, to extrapolate overall information regarding crashworthiness parameters.

## 5.2. Future development

This study puts the basis for further research. By knowing the flaws of this study and the further possibilities of analysis make the FML crushing tube field a wide and unexplored topic.

The use of other lamina types (such as unidirectional), different woven yarns, and different orientation could cause a different interaction between the material of the hybrid tube.

The use of displacement sensor during the impact test in order to obtain more precise data on the displacement of the impacting mass, instead of obtaining values from integration of acceleration.

Numerical models accuracy in capturing a wide field of failure modes, including delamination, can be improved in different ways. This goal can be achieved by implementing more complex material cards, such as MAT\_262, supported by additional experimental tests to characterize the material in a more complete way. A different modeling approach can be adopted by switching to 3-D elements or by introducing a stacked-shell approach. Additional study on cohesive elements can be performed.

The use of topological optimization of the FML could improve the overall energy absorption performance. The geometry of the constituent, in terms of thickness of ductile tube and lamination layers, is optimized to perform at its highest potential.







## Bibliography

- [1] J. A. C. Ambrosio, "General Introduction to Structural Crashworthiness," in *Crashworthiness*, 2001. doi: 10.1007/978-3-7091-2572-4\_5.
- [2] S. P. Desjardins and D. H. Laananen, *Aircraft Crash Survival Design Guide. Volume IV - Aircraft Seats, Restraints, Litters, and Padding. Final Report*, no. v. 4. Defense Technical Information Center, 1980. [Online]. Available: <https://books.google.it/books?id=ANe7NwAACAAJ>
- [3] M. A. Jiménez, A. Miravete, E. Larrodé, and D. Revuelta, "Effect of trigger geometry on energy absorption in composite profiles," *Compos. Struct.*, vol. 48, no. 1, 2000, doi: 10.1016/S0263-8223(99)00081-1.
- [4] M. Mirzaei, M. Shakeri, M. Sadighi, and H. Akbarshahi, "Experimental and analytical assessment of axial crushing of circular hybrid tubes under quasi-static load," *Compos. Struct.*, vol. 94, no. 6, 2012, doi: 10.1016/j.compstruct.2012.01.003.
- [5] A. Pandarkar, M. D. Goel, and M. S. Hora, "Axial crushing of hollow and foam filled tubes: An overview," *Sadhana - Acad. Proc. Eng. Sci.*, vol. 41, no. 8, 2016, doi: 10.1007/s12046-016-0525-4.
- [6] M. Costas, J. Díaz, L. E. Romera, S. Hernández, and A. Tielas, "Static and dynamic axial crushing analysis of car frontal impact hybrid absorbers," *Int. J. Impact Eng.*, vol. 62, pp. 166–181, Dec. 2013, doi: 10.1016/J.IJIMPENG.2013.06.011.
- [7] Y. Shen, Z. Wu, and X. Hu, "Effect of reinforcement layer number on energy absorption of aluminum-CFRP hybrid square tubes under axial loading: Experimental and numerical study," *Thin-Walled Struct.*, vol. 155, 2020, doi: 10.1016/j.tws.2020.106935.
- [8] L. Wågström, R. Thomson, and B. Pipkorn, "Structural adaptivity in frontal collisions: Implications on crash pulse characteristics," *International Journal of Crashworthiness*, vol. 10, no. 4. 2005. doi: 10.1533/ijcr.2005.0353.
- [9] A. Baroutaji, M. Sajjia, and A. G. Olabi, "On the crashworthiness performance of thin-walled energy absorbers: Recent advances and future

- developments," *Thin-Walled Structures*, vol. 118, 2017. doi: 10.1016/j.tws.2017.05.018.
- [10] A. A. A. Alghamdi, "Collapsible impact energy absorbers: an overview," *Thin-Walled Struct.*, vol. 39, no. 2, pp. 189–213, Feb. 2001, doi: 10.1016/S0263-8231(00)00048-3.
- [11] N. Jones, *Structural impact, second edition*, vol. 9781107010963. 2011. doi: 10.1017/CBO9780511820625.
- [12] Z. Tang, S. Liu, and Z. Zhang, "Analysis of energy absorption characteristics of cylindrical multi-cell columns," *Thin-Walled Struct.*, vol. 62, 2013, doi: 10.1016/j.tws.2012.05.019.
- [13] A. A. Nia and J. H. Hamedani, "Comparative analysis of energy absorption and deformations of thin walled tubes with various section geometries," *Thin-Walled Struct.*, vol. 48, no. 12, 2010, doi: 10.1016/j.tws.2010.07.003.
- [14] F. Tarlochan, F. Samer, A. M. S. Hamouda, S. Ramesh, and K. Khalid, "Design of thin wall structures for energy absorption applications: Enhancement of crashworthiness due to axial and oblique impact forces," *Thin-Walled Struct.*, vol. 71, 2013, doi: 10.1016/j.tws.2013.04.003.
- [15] A. Alavi Nia and M. Parsapour, "Comparative analysis of energy absorption capacity of simple and multi-cell thin-walled tubes with triangular, square, hexagonal and octagonal sections," *Thin-Walled Struct.*, vol. 74, 2014, doi: 10.1016/j.tws.2013.10.005.
- [16] S. Pirmohammad and S. E. Marzdashti, "Crushing behavior of new designed multi-cell members subjected to axial and oblique quasi-static loads," *Thin-Walled Struct.*, vol. 108, 2016, doi: 10.1016/j.tws.2016.08.023.
- [17] T. Wierzbicki, S. U. Bhat, W. Abramowicz, and D. Brodtkin, "Alexander revisited-A two folding elements model of progressive crushing of tubes," *Int. J. Solids Struct.*, vol. 29, no. 24, 1992, doi: 10.1016/0020-7683(92)90040-Z.
- [18] J. M. Alexander, "An approximate analysis of the collapse of thin cylindrical shells under axial loading," *Q. J. Mech. Appl. Math.*, vol. 13, no. 1, 1960, doi: 10.1093/qjmam/13.1.10.
- [19] W. Abramowicz and N. Jones, "Dynamic axial crushing of square tubes," *Int. J. Impact Eng.*, vol. 2, no. 2, 1984, doi: 10.1016/0734-743X(84)90005-8.
- [20] S. R. Guillow, G. Lu, and R. H. Grzebieta, "Quasi-static axial compression of thin-walled circular aluminium tubes," *Int. J. Mech. Sci.*, vol. 43, no. 9, 2001,



doi: 10.1016/S0020-7403(01)00031-5.

- [21] G. Lu and T. Yu, *Energy Absorption of Structures and Materials*. 2003. doi: 10.1533/9781855738584.
- [22] B. Wang and G. Lu, "Mushrooming of circular tubes under dynamic axial loading," in *Thin-Walled Structures*, 2002, vol. 40, no. 2. doi: 10.1016/S0263-8231(01)00057-X.
- [23] W. Abramowicz, "Thin-walled structures as impact energy absorbers," in *Thin-Walled Structures*, 2003, vol. 41, no. 2–3. doi: 10.1016/S0263-8231(02)00082-4.
- [24] W. Abramowicz and N. Jones, "Transition from initial global bending to progressive buckling of tubes loaded statically and dynamically," *Int. J. Impact Eng.*, vol. 19, no. 5–6, 1997, doi: 10.1016/s0734-743x(96)00052-8.
- [25] D. Karagiozova and M. Alves, "Transition from progressive buckling to global bending of circular shells under axial impact - Part I: Experimental and numerical observations," *Int. J. Solids Struct.*, vol. 41, no. 5–6, 2004, doi: 10.1016/j.ijsolstr.2003.10.005.
- [26] S. Ramakrishna and H. Hamada, "Energy absorption characteristics of crash worthy structural composite materials," *Key Eng. Mater.*, no. 143 PART II, 1998, doi: 10.4028/www.scientific.net/kem.141-143.585.
- [27] A. G. Mamalis, M. Robinson, D. E. Manolacos, G. A. Demosthenous, M. B. Ioannidis, and J. Carruthers, "Crashworthy capability of composite material structures," *Composite Structures*, vol. 37, no. 2. 1997. doi: 10.1016/S0263-8223(97)80005-0.
- [28] E. Mahdi, A. M. S. Hamouda, and T. A. Sebaey, "The effect of fiber orientation on the energy absorption capability of axially crushed composite tubes," *Mater. Des.*, vol. 56, 2014, doi: 10.1016/j.matdes.2013.12.009.
- [29] T. Ishikawa and T. W. Chou, "Stiffness and strength behaviour of woven fabric composites," *J. Mater. Sci.*, vol. 17, no. 11, 1982, doi: 10.1007/BF01203485.
- [30] N. K. Naik and V. K. Ganesh, "Prediction of on-axes elastic properties of plain weave fabric composites," *Compos. Sci. Technol.*, vol. 45, no. 2, 1992, doi: 10.1016/0266-3538(92)90036-3.
- [31] A. Rabiee and H. Ghasemnejad, "Progressive Crushing of Polymer Matrix Composite Tubular Structures: Review," *Open J. Compos. Mater.*, vol. 07, no.

- 01, 2017, doi: 10.4236/ojcm.2017.71002.
- [32] H. Hadavinia and H. Ghasemnejad, "Effects of Mode-I and Mode-II interlaminar fracture toughness on the energy absorption of CFRP twill/weave composite box sections," *Compos. Struct.*, vol. 89, no. 2, 2009, doi: 10.1016/j.compstruct.2008.08.004.
- [33] K. C. Shin, J. J. Lee, K. H. Kim, M. C. Song, and J. S. Huh, "Axial crush and bending collapse of an aluminum/GFRP hybrid square tube and its energy absorption capability," *Compos. Struct.*, vol. 57, no. 1–4, 2002, doi: 10.1016/S0263-8223(02)00094-6.
- [34] M. R. Zainal Abidin and S. Jamian, "Short review: Crashworthiness characteristic of natural fiber composite," *Int. J. Manag. Appl. Sci.*, vol. 1, no. 3, 2015.
- [35] H. Hamada, J. C. Coppola, D. Hull, Z. Maekawa, and H. Sato, "Comparison of energy absorption of carbon/epoxy and carbon/PEEK composite tubes," *Composites*, vol. 23, no. 4, 1992, doi: 10.1016/0010-4361(92)90184-V.
- [36] "Engineered materials handbook," *Choice Rev. Online*, vol. 33, no. 09, 1996, doi: 10.5860/choice.33-5121.
- [37] D. Brabazon, "Introduction: Polymer Matrix Composite Materials," *Encycl. Mater. Compos.*, pp. 563–564, Jan. 2021, doi: 10.1016/B978-0-12-819724-0.00109-9.
- [38] D. Dalli, L. F. Varandas, G. Catalanotti, S. Foster, and B. G. Falzon, "Assessing the current modelling approach for predicting the crashworthiness of Formula One composite structures," *Compos. Part B Eng.*, vol. 201, 2020, doi: 10.1016/j.compositesb.2020.108242.
- [39] N. Tanlak and F. O. Sonmez, "Optimal shape design of thin-walled tubes under high-velocity axial impact loads," *Thin-Walled Struct.*, vol. 84, 2014, doi: 10.1016/j.tws.2014.07.003.
- [40] P. H. Thornton and P. J. Edwards, "Energy Absorption in Composite Tubes," *J. Compos. Mater.*, vol. 16, no. 6, 1982, doi: 10.1177/002199838201600606.
- [41] A. G. Mamalis, Y. B. Yuan, and G. L. Viegelaahn, "Collapse of thin-wall composite sections subjected to high speed axial loading," *Int. J. Veh. Des.*, vol. 13, no. 5–6, 1992.
- [42] C. M. Kindervater, "Energy Absorption of Composites as an Aspect of

- Aircraft Structural Crash-Resistance," in *Developments in the Science and Technology of Composite Materials*, 1990. doi: 10.1007/978-94-009-0787-4\_89.
- [43] P. H. Thornton, "The Crush of Fiber-Reinforced Plastics," in *Handbook of Ceramics and Composites*, 2021. doi: 10.1201/9781003210085-11.
- [44] A. G. Mamalis, D. E. Manolakos, G. A. Demosthenous, and M. B. Ioannidis, "Analysis of failure mechanisms observed in axial collapse of thin-walled circular fibreglass composite tubes," *Thin-Walled Struct.*, vol. 24, no. 4, 1996, doi: 10.1016/0263-8231(95)00042-9.
- [45] A. G. Mamalis, D. E. Manolakos, and G. L. Viegelaahn, "Crashworthy Behaviour of Thin-Walled Tubes of Fibreglass Composite Materials Subjected to Axial Loading," *J. Compos. Mater.*, vol. 24, no. 1, 1990, doi: 10.1177/002199839002400104.
- [46] A. G. Mamalis, D. E. Manolakos, G. A. Demosthenous, and M. B. Ioannidis, "The static and dynamic axial collapse of fibreglass composite automotive frame rails," *Compos. Struct.*, vol. 34, no. 1, 1996, doi: 10.1016/0263-8223(95)00134-4.
- [47] E. Oterkus, C. Diyaroglu, D. De Meo, and G. Allegri, "Fracture modes, damage tolerance and failure mitigation in marine composites," in *Marine Applications of Advanced Fibre-Reinforced Composites*, 2016. doi: 10.1016/B978-1-78242-250-1.00004-1.
- [48] O. Laban, S. Gowid, E. Mahdi, and F. Musharavati, "Experimental investigation and artificial intelligence-based modeling of the residual impact damage effect on the crashworthiness of braided Carbon/Kevlar tubes," *Composite Structures*, vol. 243, 2020. doi: 10.1016/j.compstruct.2020.112247.
- [49] J. S. Kim, H. J. Yoon, and K. B. Shin, "A study on crushing behaviors of composite circular tubes with different reinforcing fibers," *Int. J. Impact Eng.*, vol. 38, no. 4, 2011, doi: 10.1016/j.ijimpeng.2010.11.007.
- [50] D. Hull, "A unified approach to progressive crushing of fibre-reinforced composite tubes," *Compos. Sci. Technol.*, vol. 40, no. 4, 1991, doi: 10.1016/0266-3538(91)90031-J.
- [51] G. L. Farley and R. M. Jones, "Crushing Characteristics of Continuous Fiber-Reinforced Composite Tubes," *J. Compos. Mater.*, vol. 26, no. 1, 1992, doi: 10.1177/002199839202600103.
- [52] A. G. Mamalis, D. E. Manolakos, G. A. Demosthenous, and M. B. Ioannidis,

- "The static and dynamic axial crumbling of thin-walled fibreglass composite square tubes," *Compos. Part B Eng.*, vol. 28, no. 4, 1997, doi: 10.1016/S1359-8368(96)00066-2.
- [53] G. C. Jacob, J. F. Fellers, S. Simunovic, and J. M. Starbuck, "Energy absorption in polymer composites for automotive crashworthiness," *J. Compos. Mater.*, vol. 36, no. 7, 2002, doi: 10.1177/0021998302036007164.
- [54] Y. C. Zhang and J. Harding, "A numerical micromechanics analysis of the mechanical properties of a plain weave composite," *Comput. Struct.*, vol. 36, no. 5, 1990, doi: 10.1016/0045-7949(90)90154-T.
- [55] Z. Xudong, W. Qijian, and W. Chen, "Experimental and numerical study of GFRP-reinforced steel tube under axial impact loads," *Int. J. Impact Eng.*, vol. 122, 2018, doi: 10.1016/j.ijimpeng.2018.07.018.
- [56] G. L. Farley, "The Effects of Crushing Speed on the Energy-Absorption Capability of Composite Tubes," *J. Compos. Mater.*, vol. 25, no. 10, 1991, doi: 10.1177/002199839102501004.
- [57] G. L. Farley, "Effect of Fiber and Matrix Maximum Strain on the Energy Absorption of Composite Materials," *J. Compos. Mater.*, vol. 20, no. 4, 1986, doi: 10.1177/002199838602000401.
- [58] G. Savage, "Safety and survivability in formula one motor racing," *Met. Mater. Bury St Edmunds*, vol. 8, no. 3, 1992.
- [59] J. Bieniaś, P. Jakubczak, and B. Surowska, "Properties and characterization of fiber metal laminates," in *Hybrid Polymer Composite Materials: Properties and Characterisation*, 2017. doi: 10.1016/B978-0-08-100787-7.00011-1.
- [60] A. Asundi and A. Y. N. Choi, "Fiber metal laminates: An advanced material for future aircraft," *J. Mater. Process. Technol.*, vol. 63, no. 1–3, 1997, doi: 10.1016/S0924-0136(96)02652-0.
- [61] R. C. Alderliesten and R. Benedictus, "Fiber/metal composite technology for future primary aircraft structures," in *Journal of Aircraft*, 2008, vol. 45, no. 4. doi: 10.2514/1.33946.
- [62] A. Salve, R. Kulkarni, and A. Mache, "A Review: Fiber Metal Laminates (FML's) - Manufacturing, Test methods and Numerical modeling," *Int. J. Eng. Technol. Sci.*, vol. 3, no. 2, 2016, doi: 10.15282/ijets.6.2016.1.10.1060.
- [63] C. M. Gilmore, "Advanced Composites Manufacturing By Timothy G. Gutowski," *Mater. Manuf. Process.*, vol. 13, no. 4, 1998, doi:

10.1080/10426919808935286.

- [64] R. Alderliesten, "On the Development of Hybrid Material Concepts for Aircraft Structures," *Recent Patents Eng.*, vol. 3, no. 1, 2009, doi: 10.2174/187221209787259893.
- [65] E. C. Botelho, R. A. Silva, L. C. Pardini, and M. C. Rezende, "A review on the development and properties of continuous fiber/epoxy/aluminum hybrid composites for aircraft structures," *Materials Research*, vol. 9, no. 3. 2006. doi: 10.1590/S1516-14392006000300002.
- [66] A. Vlot, "Impact loading on fibre metal laminates," *Int. J. Impact Eng.*, vol. 18, no. 3, 1996, doi: 10.1016/0734-743X(96)89050-6.
- [67] A. Fink, P. P. Camanho, J. M. Andrés, E. Pfeiffer, and A. Obst, "Hybrid CFRP/titanium bolted joints: Performance assessment and application to a spacecraft payload adaptor," *Compos. Sci. Technol.*, vol. 70, no. 2, 2010, doi: 10.1016/j.compscitech.2009.11.002.
- [68] M. R. Bambach, M. Elchalakani, and X. L. Zhao, "Composite steel-CFRP SHS tubes under axial impact," *Compos. Struct.*, vol. 87, no. 3, 2009, doi: 10.1016/j.compstruct.2008.02.008.
- [69] R. Subbaramaiah, B. G. Prusty, G. M. K. Pearce, S. H. Lim, and R. S. Thomson, "Crashworthy response of fibre metal laminate top hat structures," *Compos. Struct.*, vol. 160, 2017, doi: 10.1016/j.compstruct.2016.10.112.
- [70] M. Kathiresan, K. Manisekar, and V. Manikandan, "Performance analysis of fibre metal laminated thin conical frusta under axial compression," *Compos. Struct.*, vol. 94, no. 12, 2012, doi: 10.1016/j.compstruct.2012.05.026.
- [71] H. Jiang, Y. Ren, and J. Xiang, "A numerical study on the energy-absorption of fibre metal laminate conical frusta under quasi-static compression loading," *Thin-Walled Struct.*, vol. 124, 2018, doi: 10.1016/j.tws.2017.12.020.
- [72] R. Kalhor and S. W. Case, "The effect of FRP thickness on energy absorption of metal-FRP square tubes subjected to axial compressive loading," *Compos. Struct.*, vol. 130, 2015, doi: 10.1016/j.compstruct.2015.04.009.
- [73] H. Yang, H. Lei, G. Lu, Z. Zhang, X. Li, and Y. Liu, "Energy absorption and failure pattern of hybrid composite tubes under quasi-static axial compression," *Compos. Part B Eng.*, vol. 198, 2020, doi: 10.1016/j.compositesb.2020.108217.

- [74] G. Zhu, G. Sun, H. Yu, S. Li, and Q. Li, "Energy absorption of metal, composite and metal/composite hybrid structures under oblique crushing loading," *Int. J. Mech. Sci.*, vol. 135, 2018, doi: 10.1016/j.ijmecsci.2017.11.017.
- [75] G. Zhu, J. Liao, G. Sun, and Q. Li, "Comparative study on metal/CFRP hybrid structures under static and dynamic loading," *Int. J. Impact Eng.*, vol. 141, 2020, doi: 10.1016/j.ijimpeng.2020.103509.
- [76] G. Zhu, G. Sun, Q. Liu, G. Li, and Q. Li, "On crushing characteristics of different configurations of metal-composites hybrid tubes," *Compos. Struct.*, vol. 175, 2017, doi: 10.1016/j.compstruct.2017.04.072.
- [77] Z. Wang, X. Jin, Q. Li, and G. Sun, "On crashworthiness design of hybrid metal-composite structures," *Int. J. Mech. Sci.*, vol. 171, 2020, doi: 10.1016/j.ijmecsci.2019.105380.
- [78] ASTM, "D3039/D3039M Standard Test Method for Tensile Properties of Polymer Matrix Composite Materials," *Annu. B. ASTM Stand.*, 2014.
- [79] L. A. Carlsson, D. F. Adams, and R. B. Pipes, "Basic experimental characterization of polymer matrix composite materials," *Polym. Rev.*, vol. 53, no. 2, 2013, doi: 10.1080/15583724.2013.776588.
- [80] D 3518, "Standard Test Method for In-Plane Shear Response of Polymer Matrix Composite Materials by Tensile Test of a 645 ° Laminate 1," *Annu. B. ASTM Stand.*, vol. 94, no. Reapproved, 2007.
- [81] Society of Automotive Engineers, "Instrumentation for Impact Test - Part 1 - Electronic Instrumentation J211/1\_201403," *Soc. Automot. Eng.*, vol. 552, no. 724, 2014.
- [82] M. Y. Huang, Y. S. Tai, and H. T. Hu, "Numerical study on hybrid tubes subjected to static and dynamic loading," *Appl. Compos. Mater.*, vol. 19, no. 1, 2012, doi: 10.1007/s10443-010-9176-5.
- [83] LSTC, *LS-DYNA® Keyword User's Manual III- version R8.0*, vol. III. 2015.
- [84] O. Cousigné, D. Moncayo, D. Coutellier, P. Camanho, and H. Naceur, "Numerical modeling of nonlinearity, plasticity and damage in CFRP-woven composites for crash simulations," *Compos. Struct.*, vol. 115, no. 1, 2014, doi: 10.1016/j.compstruct.2014.04.017.
- [85] A. Cherniaev, C. Butcher, and J. Montesano, "Predicting the axial crush response of CFRP tubes using three damage-based constitutive models," *Thin-Walled Struct.*, vol. 129, 2018, doi: 10.1016/j.tws.2018.05.003.

- [86] A. Matzenmiller, J. Lubliner, and R. L. Taylor, "A constitutive model for anisotropic damage in fiber-composites," *Mech. Mater.*, vol. 20, no. 2, 1995, doi: 10.1016/0167-6636(94)00053-0.
- [87] K. Schweizerhof *et al.*, "Crashworthiness Analysis with Enhanced Composite Material Models in LS-DYNA - Merits and Limits," *LS-DYNA World Conference*. 1998.
- [88] P. Feraboli, B. Wade, F. Deleo, M. Rassaian, M. Higgins, and A. Byar, "LS-DYNA MAT54 modeling of the axial crushing of a composite tape sinusoidal specimen," *Compos. Part A Appl. Sci. Manuf.*, vol. 42, no. 11, 2011, doi: 10.1016/j.compositesa.2011.08.004.
- [89] N. E. Dowling, "Mechanical behavior of materials: Engineering Methods for Deformation, Fracture and Fatigue, Third Edition," *Choice Reviews Online*, vol. 46, no. 12. 2007.
- [90] J. H. Yan, M. A. Sutton, X. Deng, Z. Wei, and P. Zavattieri, "Mixed-mode crack growth in ductile thin-sheet materials under combined in-plane and out-of-plane loading," *Int. J. Fract.*, vol. 160, no. 2, 2009, doi: 10.1007/s10704-009-9420-x.
- [91] A. Rabiee and H. Ghasemnejad, "Finite Element Modelling Approach for Progressive Crushing of Composite Tubular Absorbers in LS-DYNA: Review and Findings," *Journal of Composites Science*, vol. 6, no. 1. 2022. doi: 10.3390/jcs6010011.
- [92] J. Hallquist, *LS-DYNA® theory manual*, no. March. 2006.
- [93] F. Dogan, H. Hadavinia, T. Donchev, and P. S. Bhonge, "Delamination of impacted composite structures by cohesive zone interface elements and tiebreak contact," *Cent. Eur. J. Eng.*, vol. 2, no. 4, 2012, doi: 10.2478/s13531-012-0018-0.
- [94] X. Xiao, M. E. Botkin, and N. L. Johnson, "Axial crush simulation of braided carbon tubes using MAT58 in LS-DYNA," *Thin-Walled Struct.*, vol. 47, no. 6–7, 2009, doi: 10.1016/j.tws.2008.12.004.
- [95] M. M. Shokrieh and S. M. Kamali Shahri, "Modeling residual stresses in composite materials," in *Residual Stresses in Composite Materials*, 2021. doi: 10.1016/B978-0-12-818817-0.00006-8.





# A Appendix A

## A.1. Manufacturing



Figure A.1: Detail at overlapping point in external lamination.

## A.2. Tensile test



Figure A.2: Failure mode of tensile test specimens.



Figure A.3: Failure mode of in-plane shear test specimens.

## B.1. Crush test pictures



Figure A.4: Tube plug to constrain tubes during tests



Figure A.5: AL tube after impact.



# List of Figures

FIGURE 0.1: CIRCULAR TUBES AFTER IMPACT (A) COMPOSITE, (B) DUCTILE .....	1
FIGURE 0.2: DROP TOWER TEST. ....	2
FIGURE 1.1: REPRESENTATIVE CRUSHING FORCE–DISPLACEMENT CURVE .....	8
FIGURE 1.2: TYPICAL LOAD CONFIGURATION .....	9
FIGURE 1.3: MOST COMMON ENERGY ABSORPTION SUB-STRUCTURES IN AUTOMOBILES [9]. ....	9
FIGURE 1.4: AXIALLY LOADED DEFORMATION MODES OF CIRCULAR TUBE [20] .....	12
FIGURE 1.5: (A) AXIAL FORCE VS AXIAL CRUSHING DISTANCE, (B) PHOTOGRAPHIC RECORD OF THE DEVELOPMENT OF WRINKLES DURING AXIAL CRUSHING [11]. ....	12
FIGURE 1.6: MILD STEEL SAMPLES, VELOCITIES FROM LEFT TO RIGHT ARE: 352, 158, 127, 114 M/S AND UNTESTED [22]. ....	14
FIGURE 1.7: BUCKLING COLLAPSE OF (A) SQUARE [23] AND (B) CIRCULAR TUBES [20]. ....	15
FIGURE 1.8: GLOBAL BUCKLING VERSUS PROGRESSIVE FOLDING [20]. ....	15
FIGURE 1.9: 2D-WEAVE COMPOSITES: (A) PLAIN, (B) TWILL, (C) 4-HARNESS, (D) 8-HARNESS [32]. ....	17
FIGURE 1.10: TYPICAL VALUES OF SEA FOR DIFFERENT MATERIALS [26] .....	18
FIGURE 1.11: TYPICAL COLLAPSE MODES FOR COMPOSITE TUBES: (A) CATASTROPHIC FAILURE (B) PROGRESSIVE FAILURE [43] ...	20
FIGURE 1.12: TYPICAL FRACTURE MODES [47]. ....	21
FIGURE 1.13: (A) MODE I-A, (B) MODE II [49]. ....	22
FIGURE 1.14: MODE III [48]. ....	22
FIGURE 1.15: MODE IV OF A KEVLAR® CIRCULAR TUBE[49]. ....	23
FIGURE 1.16: FRACTURE MECHANISMS OBSERVED IN LAMINATES [31] .....	23
FIGURE 1.17: SKETCH OF THE FRAGMENTATION SEQUENCE [21]. ....	24
FIGURE 1.18: POST CRUSHING PICTURE OF FRAGMENTATION MODE BY A WOVEN GFRP TUBE [50] .....	25
FIGURE 1.19: DETAILS OF LAMINA BENDING MODE [21]. ....	25
FIGURE 1.20: SPLAYING CRUSHING MODE [51]. ....	26
FIGURE 1.21: SPLAYING MECHANISM [50]. ....	27
FIGURE 1.22: SKETCH OF BRITTLE FAILURE MODE [51]. ....	27
FIGURE 1.23: LOCAL BUCKLING MICRO-MECHANISM [51]. ....	28
FIGURE 1.24: VARIOUS TYPE OF MECHANISMS [54]. ....	29
FIGURE 1.25: THE EFFECT OF A COLLAPSE TRIGGER MECHANISM [40]. ....	30
FIGURE 1.26: DEFINITION OF FIBER ORIENTATION OF A CIRCULAR TUBE [55]. ....	31
FIGURE 1.27: BUILD-UP OF A CROSS-PLY GLARE LAMINATE [60] .....	33
FIGURE 1.28: CANDIDATE AREA FOR AERONAUTICAL GLARE .....	35
FIGURE 1.29: CRUSHING FAILURE MODES TOP HAT GLARE STRUCTURE [69]. ....	36
FIGURE 1.30: COMPARISON OF EA AND SEA AMONG BARE SPECIMEN AND HYBRID SPECIMENS [71]. ....	37
FIGURE 1.31: COLLAPSE OF SQUARE FML WITH DIFFERENT CFRP THICKNESS [7]. ....	37
FIGURE 1.32: (A) LAY-UP DESIGN, (B) SCHEMATIC OF THE CROSS PROFILE [73]. ....	38
FIGURE 1.33: (A)EXTERNAL LAMINATION AND (B) INTERNAL LAMINATION COLLAPSING MECHANISM [75]. ....	38
FIGURE 1.34: COMPARISON OF EA AND SEA WITH (A) DIFFERENT SECTION SIZES; (B) DIFFERENT SECTIONAL SHAPES [77]. ....	39
FIGURE 2.1: RENDER OF THE HYBRID TUBE .....	40
FIGURE 2.2: ALUMINUM TUBES. ....	42
FIGURE 2.3: CROSS SECTIONAL SKETCH LAY-UP .....	43
FIGURE 2.4: CUT PREPREGS DURING THE LAMINATION. ....	43
FIGURE 2.5: CLOSE UP PICTURE OF (A) INTERNAL APPLICATION OF STRUCTURAL ADHESIVE, (B) THE OVERLAPPING SPOT FOR EXTERNAL LAMINATION. ....	44
FIGURE 2.6: HEAT-SHRINK-TAPE APPLIED DURING LAMINATION PROCESS. ....	44
FIGURE 2.7: REUSABLE VACUUM BAG FOR MID-LAMINATION COMPACTION .....	45

FIGURE 2.8: (A) 0° AND (B) 45° PRE-PREGS LAMINATION. ....	46
FIGURE 2.9: RUBBER PAD DURING THE PREPARATION OF A VACUUM-BAG. ....	47
FIGURE 2.10: VACUUM-BAG ELEMENTS ....	48
FIGURE 2.11: SEALED VACUUM-BAG. ....	48
FIGURE 2.12: TUBE SPECIMENS. ....	50
FIGURE 2.13: (A) VACUUM-BAG COUPONS WITH TABS, (B) TABS CLOSE-UP AFTER CURING CYCLE. ....	51
FIGURE 2.14: 0° AND 45° FIBER ORIENTATION SPECIMENS WITH STRAIN GAUGE. ....	52
FIGURE 3.1: (A) STRESS STATE ON A MATERIAL CHUNK, (B) STRESS STATE UNDER IN PLANE LOADING [79]. ....	54
FIGURE 3.2: TENSILE SYSTEM SETUP. ....	55
FIGURE 3.3: SCHEMATIC OF TENSILE TEST SPECIMEN. ....	56
FIGURE 3.4: TENSILE STRESS-STRAIN FOR 0° ORIENTATION SPECIMENS. ....	57
FIGURE 3.5: 45° TENSILE TEST SPECIMEN FOR MEASURING IN-PLANE SHEAR RESPONSE [79]. ....	59
FIGURE 3.6: IN-PLANE SHEAR STRESS-STRAIN RELATIONSHIP. ....	60
FIGURE 3.7: (A) SPECIMEN READY TO BE TESTED, (B) TEST SYSTEM. ....	61
FIGURE 3.8: AL TUBE CRUSHING DYNAMIC. ....	63
FIGURE 3.9: AL TUBE CRUSHING LOAD DURING THE STROKE. ....	64
FIGURE 3.10: (A) C_S_1 AND (B) C_S_3 SPECIMENS. ....	65
FIGURE 3.11: (A) FULL OF DEBRIS C_S_1 AND (B) EMPTY C_S_3 SPECIMENS. ....	65
FIGURE 3.12: INTERNAL LAMINATION BARE COMPOSITE TUBES. ....	66
FIGURE 3.13: (A) C_L_1, (B) C_L_2 CRUSHING DYNAMIC. ....	67
FIGURE 3.14: POST-CRUSH (A) C_L_1 AND (B) C_L_2 SPECIMENS. ....	67
FIGURE 3.15: LOAD-DISPLACEMENT OF EXTERNAL LAMINATION BARE COMPOSITE TUBES ....	68
FIGURE 3.16: CRUSHING DYNAMIC OF (A) H_E_3, (B) H_E_2, (C) H_E_1. ....	70
FIGURE 3.17: POST-CRUSH SPECIMENS (A) H_E_3, (B) H_E_2, (C) H_E_1. ....	70
FIGURE 3.18: LOAD-DISPLACEMENT OF EXTERNAL LAMINATION HYBRID TUBES. ....	71
FIGURE 3.19: CRUSHING DYNAMIC OF (A) H_I_1, (B) H_I_2, (C) H_I_3. ....	72
FIGURE 3.20: POST-CRUSH H_I_1 SPECIMEN. ....	73
FIGURE 3.21: POST-CRUSH H_I_2 SPECIMEN. ....	73
FIGURE 3.22: POST-CRUSH H_I_3 SPECIMEN. ....	74
FIGURE 3.23: LOAD-DISPLACEMENT OF INTERNAL LAMINATION HYBRID TUBES. ....	75
FIGURE 3.24: LOAD-DISPLACEMENT CURVES OF (A) BARE COMPOSITE AND (B) HYBRID TUBES ....	77
FIGURE 3.25: HYBRID VS. AL+CFRP ....	78
FIGURE 3.26: BAR GRAPHIC DATA OF TABLE 3.10. ....	79
FIGURE 3.27: TESTED SPECIMENS. ....	79
FIGURE 4.1: EXAMPLES OF STRESS-STRAIN RESPONSES FOR VARIOUS $E_i$ AND $SLIM_i$ VALUES, MAT58B. ....	83
FIGURE 4.2: STRESS-STRAIN DIAGRAM OF SHEAR [83]. ....	84
FIGURE 4.3: VON MISES CRITERION [89]. ....	85
FIGURE 4.4: PLASTIC REGION FOR AL6061. ....	87
FIGURE 4.5: MODEL (A) CONSTRAINED NODES, (B) RIGID WALLS. ....	90
FIGURE 4.6: EXTERNAL LAMINATION HYBRID TUBE FE MODEL. ....	91
FIGURE 4.7: MODEL AFTER IMPACT NUMERICAL VS EXPERIMENTAL ....	92
FIGURE 4.8: NUMERICAL VS EXPERIMENTAL LOAD CURVES AL TUBE. ....	93
FIGURE 4.9: C_L_1 NUMERICAL SIMULATION. ....	93
FIGURE 4.10: (A) DELETED SHELL ELEMENTS IN SIMULATION, (B) DAMAGE CAUSING THE ROTATION. ....	94
FIGURE 4.11: NUMERICAL VS EXPERIMENTAL LOAD CURVES C_L_1 TUBE. ....	95
FIGURE 4.12: HIGHER CLASS OF FILTERING FOR C_L_1. ....	96
FIGURE 4.13: H_E_1 NUMERICAL SIMULATION. ....	97
FIGURE 4.14: DOUBLE-RING FOLDING MODE. ....	97
FIGURE 4.15: NUMERICAL VS EXPERIMENTAL LOAD CURVES H_E_1 TUBE. ....	98
FIGURE 4.16: H_I_1 NUMERICAL SIMULATION. ....	99
FIGURE 4.17: H_I_1 NUMERICAL SIMULATION, INTERNAL CFRP TUBE. ....	100
FIGURE 4.18: NUMERICAL VS EXPERIMENTAL LOAD CURVES H_I_1 TUBE. ....	100
FIGURE 4.19: HIGHER CLASS OF FILTERING FOR H_I_1. ....	101

FIGURE A.1: DETAIL AT OVERLAPPING POINT IN EXTERNAL LAMINATION. ....	119
FIGURE A.2: FAILURE MODE OF TENSILE TEST SPECIMENS. ....	120
FIGURE A.3: FAILURE MODE OF IN-PLANE SHEAR TEST SPECIMENS. ....	120
FIGURE A.4: TUBE PLUG TO CONSTRAIN TUBES DURING TESTS ....	121
FIGURE A.5: AL TUBE AFTER IMPACT.....	121





## List of Tables

TABLE 1.1: SUMMARY OF CRASHWORTHINESS COMPARATIVE PAPERS [9].....	11
TABLE 1.2: SQUARE AND RECTANGULAR VERSUS CIRCULAR TUBE SECTION .....	19
TABLE 1.3: ADVANTAGE OF FML [62] .....	34
TABLE 2.1: FABRIC PREPREG DESCRIPTION.....	41
TABLE 2.2: AL TUBES FEATURES.....	41
TABLE 2.3: ASTM3039 SPECIMEN DIMENSIONS.....	45
TABLE 2.4: TYPICAL M79 EPOXY CURE CYCLE BY HEXPLY® .....	49
TABLE 2.5: GEOMETRIC MEASURE OF TESTED TUBES. ....	50
TABLE 2.6: TENSILE AND PLAIN SHEAR TEST SPECIMEN DIMENSIONS. ....	52
TABLE 3.1: TENSILE TEST RESULTS .....	57
TABLE 3.2: IN-PLANE SHEAR TEST RESULTS .....	60
TABLE 3.3: EFFECTIVE MATERIAL DENSITY .....	62
TABLE 3.4: AL TUBE CRUSHING DATA. ....	64
TABLE 3.5: INTERNAL LAMINATION BARE COMPOSITE TUBES CRUSHING DATA.....	66
TABLE 3.6: EXTERNAL LAMINATION BARE COMPOSITE TUBES CRUSHING DATA. ....	69
TABLE 3.7: EXTERNAL LAMINATION HYBRID TUBES CRUSHING DATA.....	71
TABLE 3.8: INTERNAL LAMINATION HYBRID TUBES RESULT DATA. ....	75
TABLE 3.9: RESULTS OF THE SPECIMEN TESTED.....	76
TABLE 3.10: CRASHWORTHINESS PARAMETERS RELATIVE TO 70 MM OF STROKE.....	78
TABLE 4.1: *MAT_058 CARD OVERVIEW .....	83
TABLE 4.2: CFRP LAMINATE MAT058 PARAMETERS. ....	84
TABLE 4.3: CONTINUE OF TABLE 4.2. ....	85
TABLE 4.4: *MAT_024 CARD OVERVIEW .....	86
TABLE 4.5: ALUMINUM 6060 MAT024 CONSTANTS. ....	87
TABLE 4.6: *AUTOMATIC_ONE_WAY_SURFACE_TO_SURFACE_TIEBREAK CARD OVERVIEW.....	88
TABLE 4.7: TIEBREAK CONTACT CARD PARAMETERS.....	89
TABLE 4.8: AL TUBE COMPARISON OF NUMERICAL MODEL IMPACT RESULTS.....	92
TABLE 4.9: C_L_1 TUBE COMPARISON OF NUMERICAL MODEL IMPACT RESULTS.....	95
TABLE 4.10: H_E_1 TUBE NUMERICAL MODEL IMPACT RESULT.....	99
TABLE 4.11: H_I_1 TUBE NUMERICAL MODEL IMPACT RESULT.....	101



## List of symbols

<b>Variable</b>	<b>Description</b>	<b>SI unit</b>
$D$	Diameter	mm
$t$	Thickness	mm
$l$	Length	mm
$L$	Tube length	mm
$v$	Velocity	m/s
$\sigma_y$	Yield stress	MPa
$\sigma_u$	Ultimate stress	MPa
<b>CFRP</b>	Carbon fiber reinforced plastic	
<b>GFRP</b>	Glass fiber reinforced plastic	
<b>AL</b>	Aluminium	



## Acknowledgments

This endeavor would not have been possible without professor Astori and Politecnico di Milano, they gave me the chance and the tools to perform this study.

I would like to extend my sincere thanks to Ing. Colamartino, Ing. Vignati and Ing. Gahavanini that help me, and were patient to me, during the process. Special thanks to Dot. Rigamonti who believed and helped me in the realization of internal lamination. I would like to recognize Ing. Scampini, fundamental during the test campaign.

I would be remiss in not mentioning miss. Cavallaro that guided me in the writing phase of this thesis.

I am also grateful to my family that gave me the opportunity to study and helped me in times of need during my student career in all these many years.

A special thanks to my parents, I dedicate this final milestone to you, with love.

Many thanks to all my friends (especially, Alberto and Alessandro) that were there in the highs and lows, and to all my study buddies during exam sessions. Also, thanks to Desio library, a second home for me.

Last in order but first in importance, a special thanks to my soulmate Alessia, you were my beacon in these years in the mist.

